Final Report/Amended

Project Title: Water Transport in PEM Fuel Cells: Advanced Modeling, Material Selection, Testing, and Design Optimization

Project Period: June 1, 2007 to May 31, 2012
Date of Report: September 4, 2012

Recipient: CFD Research Corporation
Award Number: DE-FG36-07GO17010

Working Partners:
Ballard Power Systems, Burnaby, BC, Canada
BCS Fuel Cells, Bryan, TX
ESI US R&D, Huntsville, AL
Techverse, Cary, NC
SGL Carbon, Meitingen, Germany
University of Victoria, Victoria, BC, Canada

Cost-Sharing Partners:
CFD Research Corporation
Ballard Power Systems, Burnaby, BC, Canada
BCS Fuel Cells, Bryan, TX
ESI US R&D, Huntsville, AL
Techverse, Cary, NC
SGL Carbon, Meitingen, Germany

Contact: J. Vernon Cole (Principle Investigator and Primary Contact)
CFD Research Corporation
215 Wynn Drive, 5th Fl.
Huntsville, AL 35805
Phone: (256) 726-4852; Fax: (256) 726-4806
E-mail: jvc@cfdrc.com

DOE Managers: DOE HQ Technology Manager: Donna Ho;
DOE Field Project Officer: David Peterson

1. EXECUTIVE SUMMARY

Water management in Proton Exchange Membrane, PEM, Fuel Cells is challenging because of the inherent conflicts between the requirements for efficient low and high power operation. Particularly at low powers, adequate water must be supplied to sufficiently humidify the membrane or protons will not move through it adequately and resistance losses will decrease the cell efficiency. At high power density operation, more water is produced at the cathode than is necessary for membrane hydration. This excess water must be removed effectively or it will accumulate in the Gas Diffusion Layers, GDLs, between the gas channels and catalysts, blocking diffusion paths for reactants to reach the catalysts and potentially "flooding" the electrode. As power density of the cells is increased, the challenges arising from water management are expected to become more difficult to overcome simply due to the increased rate of liquid water generation relative to fuel cell volume. Thus, effectively addressing water management based issues is a key challenge in successful application of PEMFC systems.

In this project, CFDRC and our partners used a combination of experimental characterization, controlled experimental studies of important processes governing how water moves through the fuel cell materials, and detailed models and simulations to improve understanding of water management in operating hydrogen PEM fuel cells. The characterization studies provided key data that is used as inputs to all state-of-the-art models for commercially important GDL materials. Experimental studies and microscopic scale models of how water moves through the GDLs showed that the water follows preferential paths, not branching like a river, as it moves toward the surface of the material. Experimental studies and detailed models of water and airflow in fuel cells channels demonstrated that such models can be used as an effective design tool to reduce operating pressure drop in the channels and the associated costs and weight of blowers and pumps to force air and hydrogen gas through the fuel cell. Promising improvements to materials structure and surface treatments that can potentially aid in managing the distribution and removal of liquid water were developed; and improved steady-state and freeze-thaw performance was demonstrated for a fuel cell stack under the self-humidified operating conditions that are promising for stationary power generation with reduced operating costs.

2. INTRODUCTION

The overall objectives of this project were to achieve:

- Improved understanding of the effect of various cell component properties and structure on the gas and water transport in a PEM fuel cell, with particular emphasis on the gas diffusion media (GDM) and flow channels which have critical roles in transporting excess liquid water;
- Encapsulation of the developed advanced models in a commercial modeling and analysis tool, allowing transfer of technology to the industry for future applications to improve and optimize fuel cell design and operation; and
- Demonstrated improvements in water management resulting in improved efficiency during automotive drive cycles, freeze/thaw cycle tolerance, and faster cold startup.

CFD Research Corporation (CFDRC) planned to develop and demonstrate a PEM fuel cell design improved/optimized for cold start and efficient automotive drive cycle operation through improved water management. The improved design would be accomplished by improving and using advanced simulation capabilities and by conducting complementary experiments for validation/calibration of new models and selection of new materials. The simulation capabilities include physically based, validated models for key phenomena associated with operation of PEM fuel cells, with adequate treatment of multiphase water and gas transport as well as treatment of freeze/thaw behavior. The selected team included Techverse, ESI Group, BCS Fuel Cells, Ballard Power Systems, SGL Carbon and the University of Victoria. The roles of the team members were as follows:

- CFDRC: Overall project management, microscale and cell scale model development, testing, and application;
- Ballard Power Systems: Measurement tools, material data, and operational test results to validate and support the development of models for water transport and management; continuing application of the developed models;
- Techverse: Materials characterization and modification, water transport experimental characterization for channel and GDL assemblies;
- BCS Fuel Cells: Operational cell and stack diagnostics, materials sensitivity, and freeze-thaw cycling characterization for serpentine channel cells under self-humidified conditions;
- ESI Group, NA: Model implementation and software integration, model testing; commercial release of the developed models;
- SGL Carbon: GDL and bipolar plate materials supplier; and
- U. Victoria: Experimental studies of GDL permeation and channel droplet injection, water transport analysis and quantification.

Our approach to improving fundamental understanding of water transport was as follows. We characterized the impact of fuel cell component material properties and structure on water management through ex-situ and in-situ experimental studies. The resulting data, and complimentary publicly available information, was used to develop, test, and validate modeling tools for analysis of water and two-phase transport in fuel cells. The developed experimental and numerical capabilities were then be applied to evaluating and optimizing fuel cell and stack scale water management.

3. PROJECT OBJECTIVES AND ACCOMPLISHMENTS

The specific technical objectives included the following:

- Experimentally characterize relevant physical properties, namely porosity, pore size distribution, and effective contact angle, of fuel cell component materials;
- Perform ex-situ analysis of water, air, and two-phase mixture transport in representative cell components;
- Gather in-situ data on the effect of component material properties and design on liquid water formation and transport, and the resulting cell performance variations;
- Develop, test, and demonstrate improved models for two-phase water and gas transport in porous GDM materials;

- Develop, test, and demonstrate improved models for two-phase transport in fuel cell gas channels with appropriate coupling to the GDM;
- Integrate the two-phase transport models with a CFD based fuel cell simulation code, CFD-ACE+;
- Verify the resulting cell-scale analysis and design tool against measured cell performance and in-situ diagnostic data;
- Develop, demonstrate, and test models for freezing and thawing of liquid water with corresponding heat transfer effects;
- Devise concepts for improved water management in H_2 PEM fuel cells through modification of cell component characteristics and/or operating conditions;
- Perform physical and computational designed experiments/parametric studies to screen the potential water management improvements for feasibility and effectiveness and optimize performance; and
- Simulate and experimentally demonstrate the resulting prototype single cell and stack performance improvements in peak power, freeze/thaw cycle tolerance, and/or cold start delay.

The majority of these objectives were accomplished, with the following exceptions:

- Verify the resulting cell-scale analysis and design tool against measured cell performance and in-situ diagnostic data: liquid water in the membrane electrode assembly was significantly under-predicted compared to experimental diagnostic data;
- Develop, demonstrate, and test models for freezing and thawing of liquid water with corresponding heat transfer effects: freeze-thaw modeling was not addressed due to challenges in improving liquid water predictions;
- Simulate and experimentally demonstrate the resulting prototype single cell and stack performance improvements in peak power, freeze/thaw cycle tolerance, and/or cold start delay: single cell performance simulations of improvement concepts were not performed; experimental assessment was performed and is reported below.

4. SUMMARY OF PROJECT ACTIVITIES:

4.1 Ex-Situ Material Characterization

Materials characterization efforts were planned in order to better understand the impact of properties of individual fuel cell components on water transport and fuel cell operation, and to provide necessary input data to the modeling efforts. The individual components involved in the water transport in a PEM fuel cell are: bipolar plates with gas flow channels; gas diffusion layers; cathode and anode catalyst layers; and the polymer electrolyte membrane. The material characteristics of each of these components that can influence water transport are discussed below:

Bipolar plate: Composition of the bipolar material e.g. resin used for molded graphite as well as surface treatments can affect wettability of the bipolar plates. The electrical and thermal conductivities affect water transport indirectly by affecting the cell power output and cell temperature.

Gas diffusion layers (GDLs): The GDL is typically a porous layer of carbon fibers or a woven carbon cloth, treated to repel water by addition of Polytetrafluoroethylene (PTFE). The wetting characteristics, thickness, porosity, and pore size distribution can directly affect the water transport behavior through the GDL. The electrical and thermal conductivity of the GDL material again can indirectly affect the water transport.

Catalyst layers: The carbon used and its geometry (e.g. particles or fibers), catalyst particle size distribution/average size, ionomer content, porosity, thickness all can have a direct influence on the rate of water formation and water transport characteristics. The electrical and thermal conductivity of the catalyst layers again can indirectly affect the water transport.

Membrane: The equivalent weight of the polymer membrane material determines the water of hydration for carrying each proton as well as the water diffusion coefficient. The water of hydration determines the electro-osmotic water flux occurring along with the flux of protons through the membrane. The proton conductivity and thickness of the membrane influence the rate of reaction and hence the rate of water formation.

The characterization studies largely focused on GDL physical and transport properties. During low power operation, adequate water must be supplied to the cell to establish and maintain the membrane humidification for adequate protonic conductivity or resistance losses will decrease the cell efficiency. This vapor phase water must diffuse through the GDL, in parallel with the reactants, in order to reach the catalyst layers and membrane. At high power density operation, more water is produced at the cathode than is necessary for membrane hydration. This excess water must be removed effectively or it will accumulate in the GDL and block the pathways for reactant transport to the catalysts, introducing mass transport losses and potentially "flooding" the electrode. The liquid water transport properties of the GDL, and any tendency to hold liquid water in place due to surface tension effects, are therefore key contributors to the ability of the cell to operate effectively at high power. Similarly, the GDL must provide electrical and thermal conduction pathways from the bipolar plates to the catalyst region, and both conductivities can have a strong impact on the water formation rate. Despite this importance, many key properties of these materials were poorly characterized. In particular, the principal properties controlling liquid water movement through the GDL were typically estimated from correlations used to describe very different porous materials such as soils. These properties are the capillary pressure, which describes how surface tension effects produce forces to distribute the liquid water within the material, and the relative permeability, which captures the effects of any liquid on the resistance to gas phase flow through the material.

4.1.1 Physical Properties

Much of the ex-situ GDL characterization work was performed by the team members from Ballard. The data collected as part of the ex-situ characterization effort included laser microscope imaging data for 3-D microstructure creation, mercury porosimetry data for porosity and pore size distribution, effective diffusivity (D/Do), through plane and in-plane gas phase permeability, thickness as a function of compression, electrical conductivity as a function of compression and in-plane electrical conductivity. In all data collected, where possible, more than one sample from different Toray papers for the same nominal Teflon loading were also used to assess process variability impact. In all cases, several measurement

locations on the sample are used to characterize GDL variability, in order to assess standard deviations of the measured properties and error bars of the measurement techniques. The following materials were characterized:

- Toray TGP50 at 0%, 10%, 20%, 30%, 40%, 45%, 50% Teflon loadings
- SGL 24BC, 25BC, 34BC, 35BC (as supplied by SGL/CFDRC)
- BMP GDS1120 (commercial BMP material)

Some typical examples of collected data for the case of Toray (30% loading) are shown below.

Figure 1. Laser Microscope Images at 20x and 50x Zooms (2D Slice of 3D Image Database)

For all the material samples, mercury porosimetry was used to determine the porosity and pore size distribution. Representative data for a typical pore size distribution for 30% loaded Toray, and porosity variation with Teflon loading, are shown in Figure 2 and Figure 3.

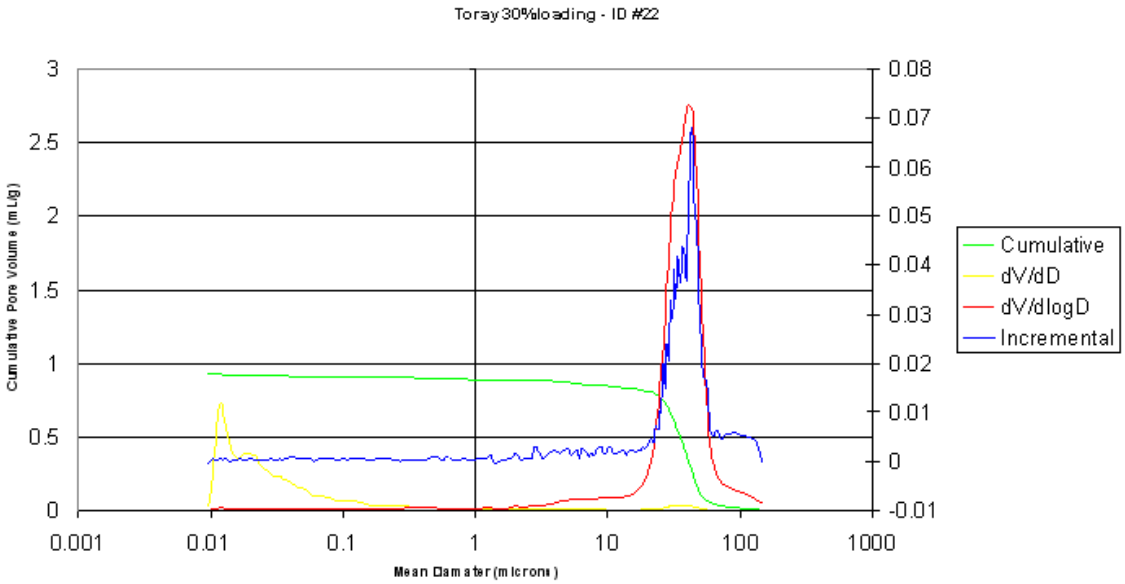

Figure 2. Measured Pore Size Distribution for 30% Teflon Loaded Toray

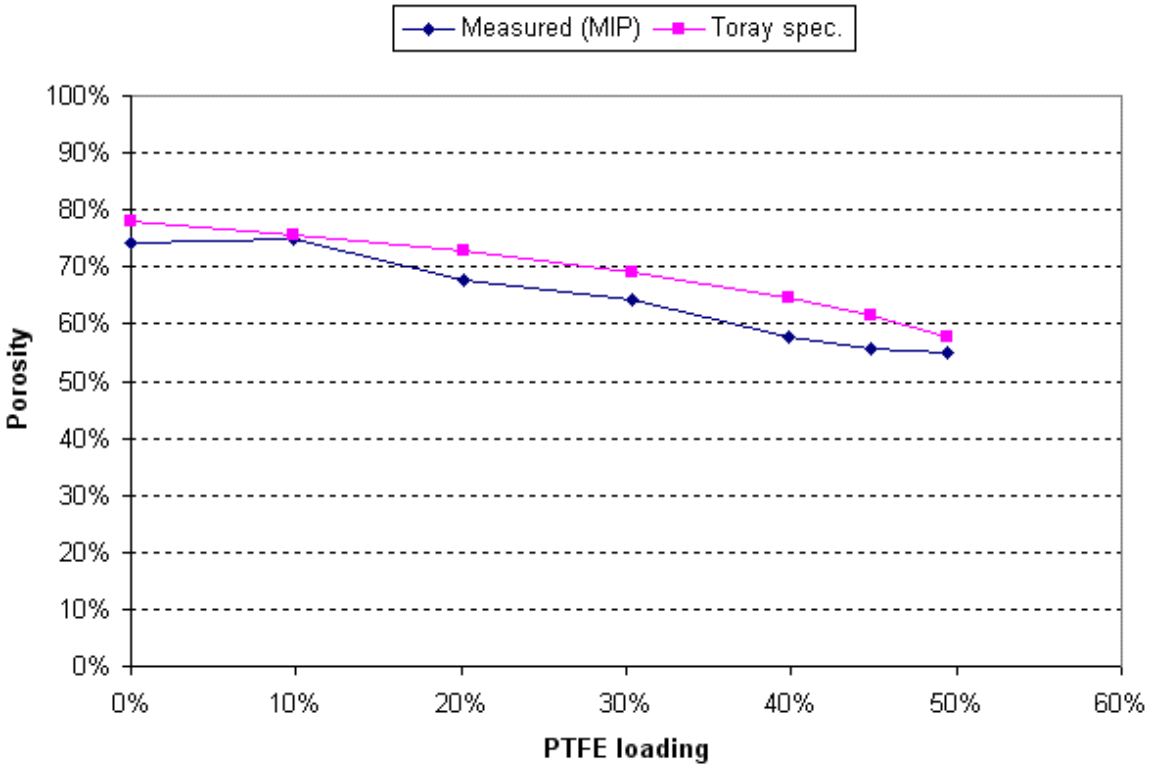

Figure 3. Porosity as a Function of Teflon Loading for Toray

Next, typical values of measured effective diffusivity and electrical conductivity under compression are shown:

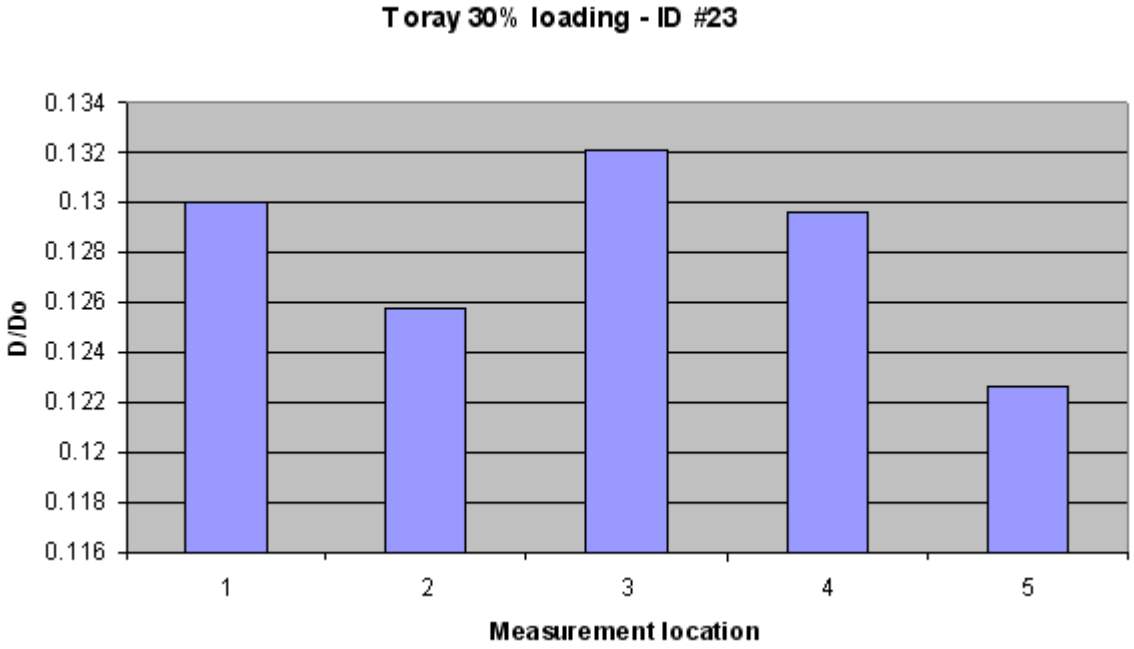

Figure 4. Effective Diffusivity (D/Do) for Toray with 30% Teflon

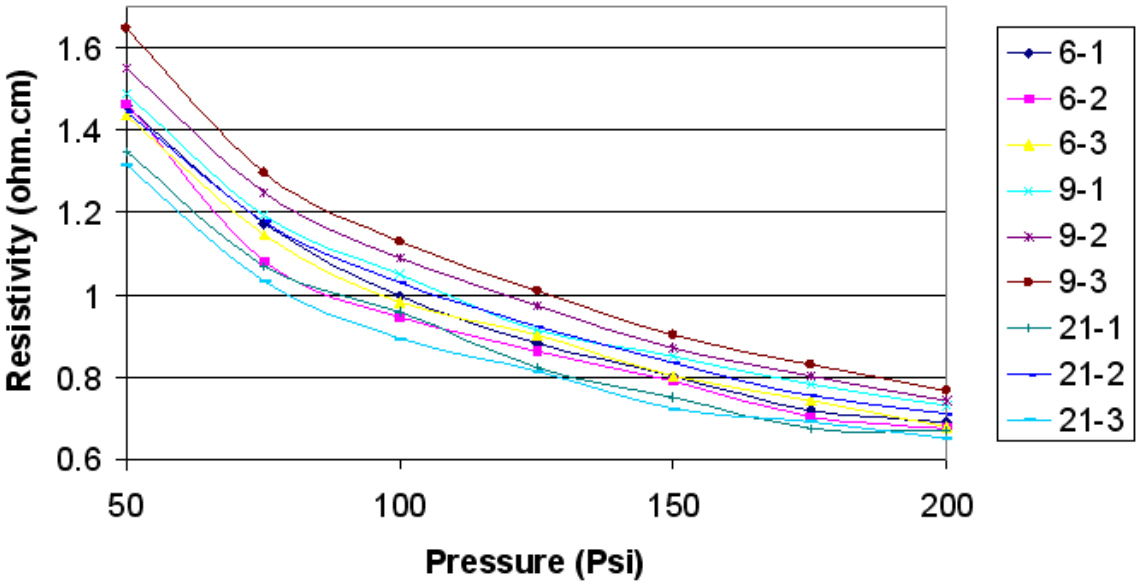

Figure 5. Resistivity Variation at 3 Different Measured Locations for 3 Samples of 30% Teflon Loaded Toray

The final data set from Ballard was in the form of spreadsheets comprising a property database for SGL, Ballard Materials Products (BMP), and Toray paper GDLs with a range of PTFE loadings including:

- Porosity and Pore Size Distribution (Mercury Intrusion Porosimetry, Method of Standard Porosimetry);
- In- and Through-Plane Gas Permeability, Effective Diffusivity;
- Electrical and Thermal Conductivity; and
- Thickness & Electrical Resistance Variation with Compression.

An example summary figure from the GDL porosity measurement, with standard deviation bars and comparison to the manufacturers' specifications, is shown in Figure 6 below.

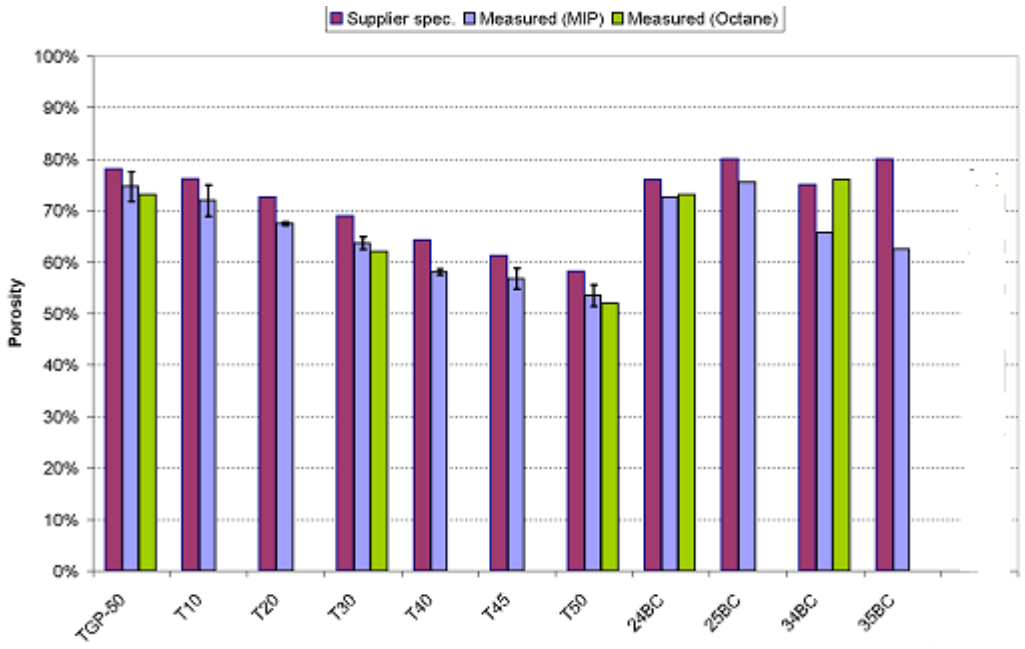

Figure 6. Measured Porosity for GDL Samples at Varying PTFE Loadings, with Supplier Specifications and Standard Deviation

These measurements were all performed using standard techniques, and provided valuable input data for the models described in the following sections. The imaging studies initially appeared to be a promising route to generate detailed geometric models of the GDL microstructure for detailed simulations of water transport using the Lattice Boltzmann Method, LBM. Unfortunately, we could not develop an acceptable methodology for using that data directly. The images were used to qualitatively verify that the microstructures generated for the LBM were representative of the material structure.

4.1.2 Capillary Pressure

Our collaborator Ashok Damle, initially at Research Triangle Institute then continuing his contributions at Techverse, provided capillary pressure and other water transport related characterization data for GDL samples provided by SGL Carbon and Ballard. An experimental apparatus based-on direct water displacement in to the GDL media produced by applied hydrostatic head was assembled to determine capillary pressure-water saturation correlation. This technique was originally used by Nguyen et al. [1] to determine capillary pressure–saturation correlation of GDL materials.

Capillary pressure – water saturation characteristics were measured for the SGL series 24, 25, 34, and 35 GDL materials. Since these GDL media had integrated microporous layers with additional carbon particles on one face, resulting in two distinct surface textures on opposite sides, experiments were conducted for both sides facing the water in the holder. The observed capillary pressure, Pc = Pgas – Pliq, as a function of water saturation correlations for SGL 24 BC GDL are shown in Figure 7 and Figure 8. Only slightly greater than 1” of water pressure was needed for water breakthrough of the sample surface with the 24 BC GDL. There was almost no hysterisis pattern observed during the imbibing and draining cycle. This material has a relatively large mean pore size, as seen above in Figure 6.

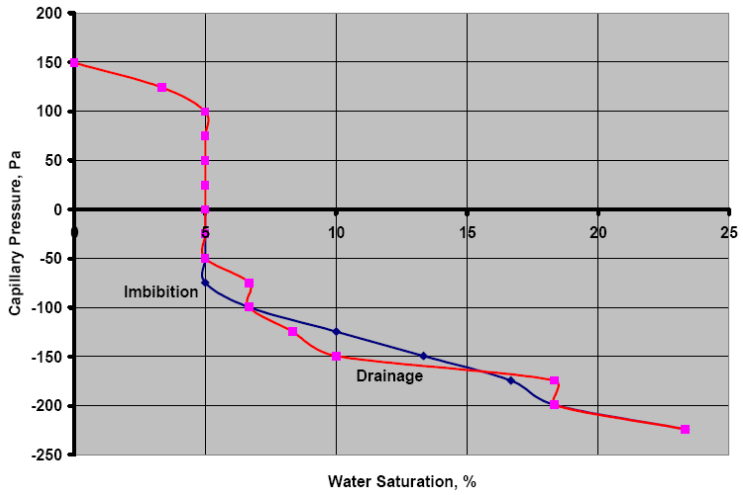

Figure 7. Capillary Pressure – Saturation Correlation For 24 BC GDL (MPL Facing Water)

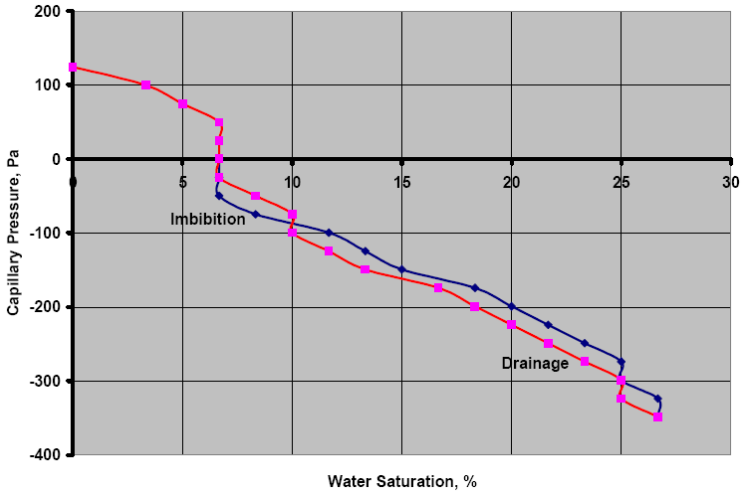

Figure 8. Capillary Pressure – Saturation Correlation For 24 BC GDL (Coarse Side Facing Water)

Contrasting behavior was observed with the 35 BC GDL media. When the media was held in the filter holder with the MPL side facing water, a quick breakthrough was observed with only 1" of water hydrostatic pressure. When the MPL side was facing air, however, greater than 14" of water pressure (3484 Pa) was needed before water breakthrough in the media was observed. The observed capillary-pressure water saturation correlation for 35 BC GDL media with MPL side facing air is shown in Figure 9.

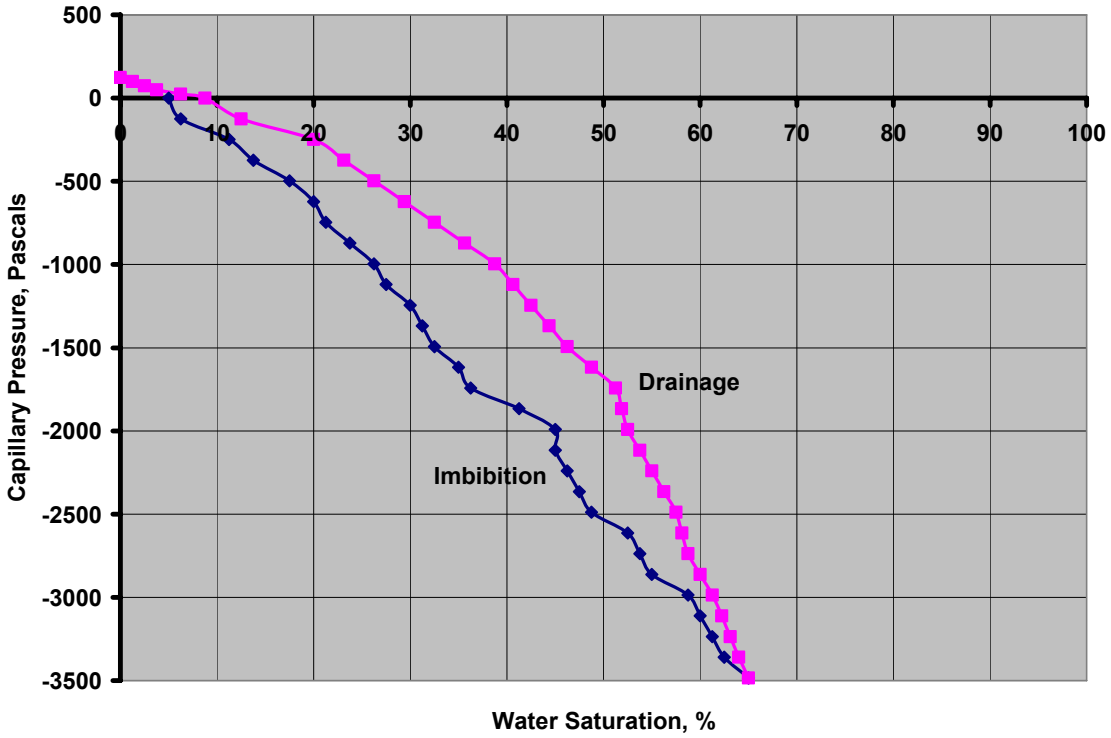

Figure 9. Capillary Pressure – Saturation Correlation for 35 BC GDL (MPL Side Facing Air)

It was observed that for all GDL media characterized the water breakthrough typically occurs at only a few spots in the exposed media area, indicating inhomogeneity of the media with a preponderance of coarser pores in a region being responsible for water breakthrough. This qualitative observation was consistent with other interfacial studies performed at the University of Victoria. However, the capillary pressure curves measured by RTI were not consistent with other studies that were appearing in the literature at the time, in particular these curves did not resolve effects due to the bimodal pore size distributions. Addition of a porous PTFE backing on the air side of the apparatus improved the agreement between the measured capillary pressure ranges and other data appearing in the literature, and also allowed more consistent measurements of the water saturation at breakthrough. We eventually chose to use published correlations for capillary pressure in the developed models due to the concerns about the RIT measurements. The observed water saturation at the breakthrough was consistent with typically reported values of residual saturation in partially wet samples, and these values were used in later modeling work.

4.1.3 Relative Permeability

The permeability of a porous material such as a GDL characterizes the increased resistance to flow of a gas through the sample induced by the solid material. The relative permeability is needed to characterize the increased resistance observed when two fluid phases, i.e. liquid and gas, are present and there is also drag induced on one of those fluids by the other fluid. Models for the relative permeability often assume a power law relation, either linear or cubic dependence on the phase fractions, with little justification. Therefore, we planned to attempt to determine relative permeability relations through experimental characterization, resolving this ambiguity in models for fuel cell water transport.

RTI designed an apparatus to allow investigation of relative permeability and two-phase (water and air) transport behavior of GDL samples. The resulting experimental apparatus was assembled to measure gas permeability through the GDL media, and consisted of a filter holder to house the media, a regulated low pressure gas flow, a differential (30" water pressure) pressure gauge to measure pressure drop across the media and a bubble flow meter to measure gas flow rate exiting the media at ambient pressure. Dry gas (Nitrogen) permeability was first measured with a dry media housed in the filter holder. The media was then filled with water by filling up both sides of the holder with water then applying a small, 5 psig, nitrogen pressure to the inlet side of the holder (this step was repeated 3 times). The water was then drained from both sides and a small nitrogen pressure was applied on the inlet side of the holder. After a threshold initial pressure (~ 5" of water) was exceeded, gas flow rate increased with increasing pressure. The trans-GDL pressure drop was then held constant at 25" of water with gas flow increasing with time eventually reaching a near steady state. The flow rate/pressure drop measurements were then made for the 5 to 30" pressure drop range. The measurements were then repeated with humidification of inlet gas to near saturation by passing the inlet flow through a water bubbler.

A representative sample of the data, the observed flow characteristics for 35 BC GDL media, is shown in Figure 10. This figure also includes the increase in the initial gas flow rate with increasing pressure at the beginning of the wet media measurements. In general, the steady state gas flow with wet media was significantly lower than that for the dry media as expected.

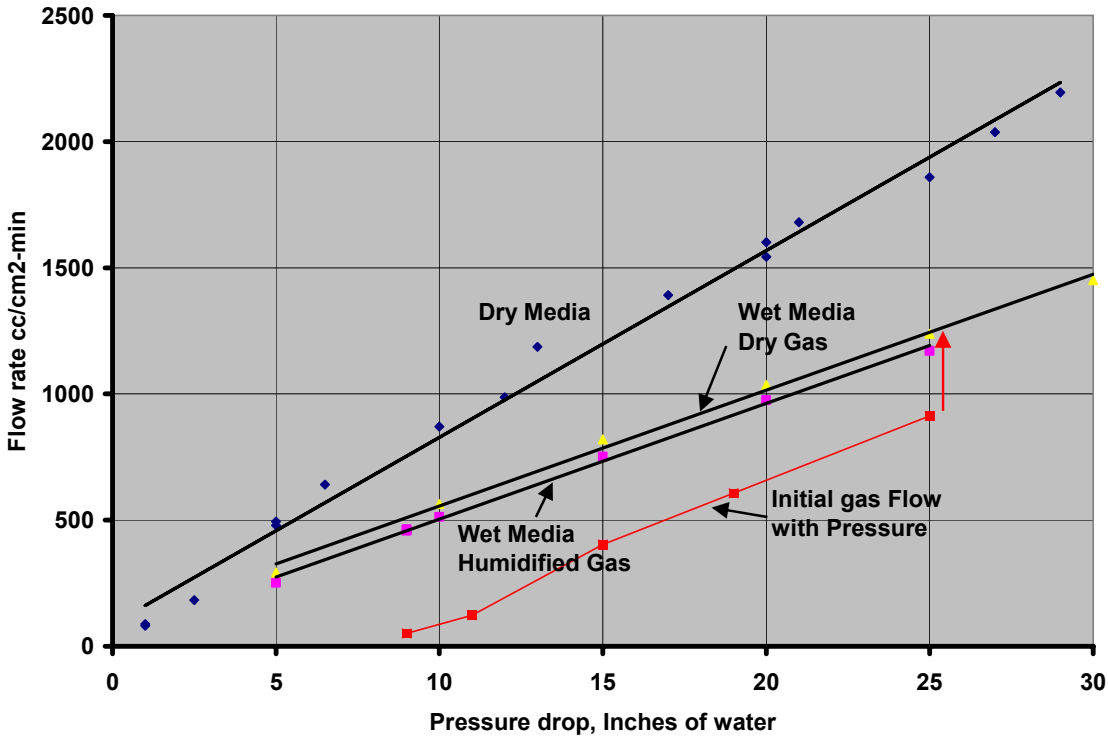

Figure 10. Nitrogen Flow Characteristics for 35 BC GDL Media. Red Curve Demonstrates the Pressure Drop – Flow Rate Relation during Establishment of Gas Flow through Initially Saturated Media.

Single phase water permeability characterization of various gas diffusion layer (GDL) media was performed by Techverse using a simple experimental set up. Water permeability characteristics of the GDL media were determined by measuring the water flow rate through the media as a function of hydrostatic water pressure applied. This effective permeability is expressed as the volumetric flow rate per sample area scaled by the sample thickness and the applied pressure difference, equivalent to the ratio of the Darcy's Law permeability and the water viscosity. The water permeability results of the different media were compared to determine if PTFE has a major effect on water permeability.

Figure 11 depicts the effective water permeability properties for SGL Carbon GDL samples. At lower head pressure, the effective water permeability of the media is low. This occurrence is likely due to the hydrophobicity provided by the PTFE, since the applied pressure must exceed the capillary pressure resistance before significant liquid water flow can occur. After a certain pressure, the water permeability increases drastically. The point at which the water permeability increases is similar to the observed breakthrough pressures of the various media. At the breakthrough pressure, a path with little resistance for the water is created, resulting in much greater water permeability than that observed before the break through pressure since the dominant effects become the drag of the porous material instead of the surface tension and capillary forces.

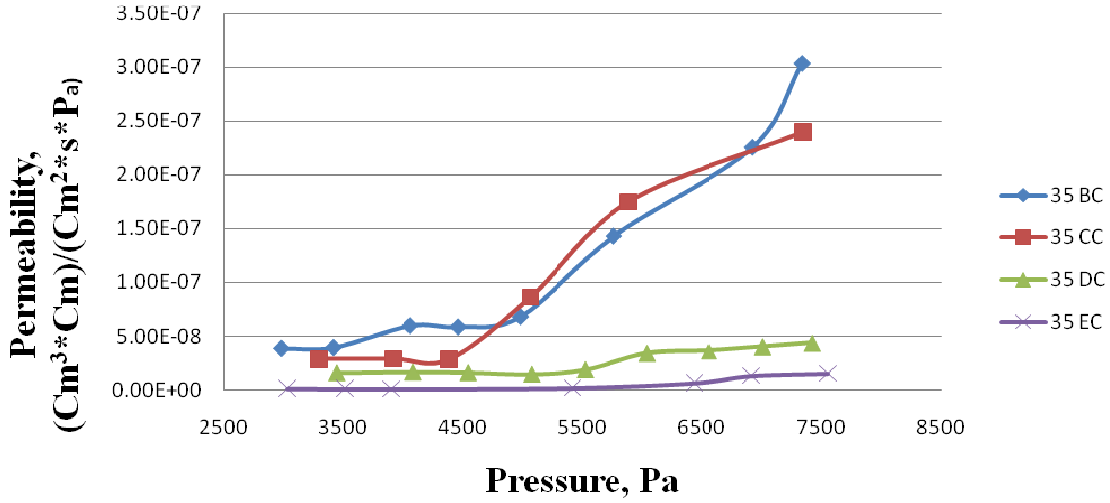

Figure 11. Effective Water Permeability of SGL 35 Series Media

The general trend observed from the comparison is that the lower the PTFE content, the higher the water permeability will be. This experiment did allow some air to remain in the GDL samples, so that the relative permeability of water is contributing to the observed trends. However, the results are convoluted with capillary pressure effects and the approach did not allow accurate determination of the water volume fraction in the GDL pore space at each data point. Therefore, we were not able to determine a direct relation between the relative permeability and saturation.

In addition to the permeability, Techverse determined the residual water saturation of the GDL samples at the end of the experiments for both air flow through wet media and water flow

through initially dry media. Analysis of this data, in conjunction with the data obtained during the capillary pressure measurements, indicated that the relative permeability was a linear function of the water fraction in the media. A linear relationship was also observed by Sole [2], using a more rigorous approach to control the flow rate of each phase and determine the water saturation, and this functional form was used in the cell scale models described below.

4.1.4 GDL/Channel Interface Transport

The phenomena occurring when liquid water reaches the surface of the GDL, then either evaporates or forms droplets that can grow, merge, and detach into the channel gas stream, were considered to be another poorly understood aspect of water management in operating cells. In order to improve the fundamental understanding of these phenomena, Professor Ned Djilali of the University of Victoria contributed studies of time-dependent water transport and percolation through GDLs. The overall aim of these experiments was to provide data for evaluation of the LBM microscale water transport models, and to support development of improved interfacial conditions in the cell-scale computational fluid dynamics based models.

The technical objectives of this study were to:

- Investigate the transitional and steady processes up to the breakthrough point, when water a percolation path forms in the GDL between the reservoir and the surface of the GDL.
- Perform dynamic characterization of pressure, flow rate, and percolation.
- Correlate the (four) main data clusters: pressure, flow rate, images of the percolation area, and material properties of the probing porous layer (the carbon paper GDL).

The work built on some prior experience. Litster et al [3] successfully tested the idea of using fluorescent dye for monitoring water flow in a sublayer layer of the GDL. Bazylak et al [4] proposed robust test cell design and subsequently [5] tested the possibility of incorporating a pressure sensor in the hydraulic system. U. Victoria extended these ideas and developed an improved methodology for measurement and analysis to achieve the objectives of the present collaborative work.

Two data acquisition methods were devised and are abbreviated as PV and PVI. The first one, PV, consisted of collecting two data streams for pressure P(t) and injected volume V(t) respectively, and performing solely visual observations of the invasion events. Though the morphological observations are qualitative, this approach has an important advantage. Since the percolation cell now can be mounted outside of the microscope table, the access to the output window, is open and it is possible by wicking percolated drops to set a quasi-steady-state flow through the carbon paper for a given flow rate. This allows measurement of the pressure difference, $\Delta p2$, through the carbon paper at the "steady state" invasion condition, in addition to measuring the pressure difference at percolation, $\Delta p1$. In the second method, PVI, pressure P(t), volume V(t), and images I(t) are recorded in time. This method is suitable for a few successive percolations only.

Typical PV data is presented in Figure 12. For the pre-set flow rate (a) we have measured the pressure response (b) in the hydraulic system. The visual observation reveals that on the outlet

area of the percolation cell, the first percolated drop appears at the point B while the pressure reaches some characteristic value Δp1. After this maximum the pressure decays to some steady state value, the point C, Δp2< Δp1. After the moment of percolation, B, the drops constantly appear through the same, and spontaneously chosen, output locations in the porous surface. This is consistent with the previously reported result of Bazylak et al [4].

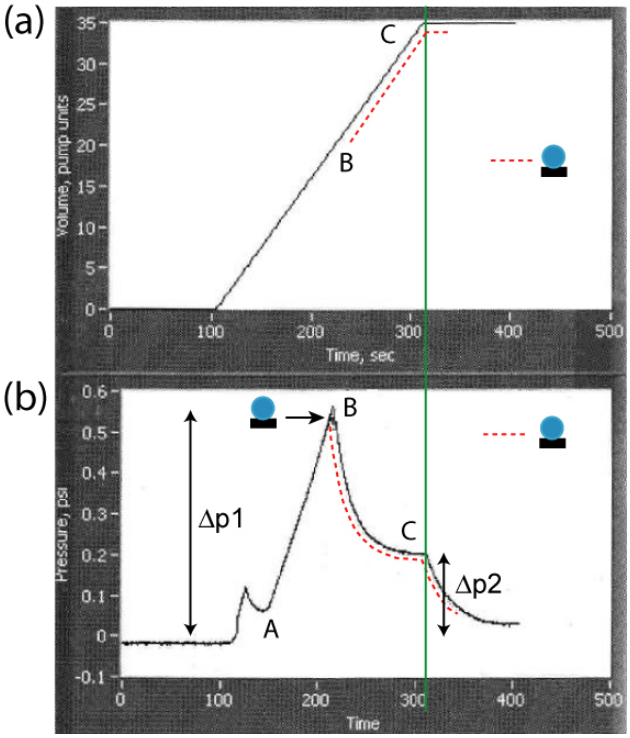

Figure 12. Data Obtained using the PV Method under Steady Flow Conditions in an Initially Dry Sample: (a) Injected Volume V(t); (b) Pressure P(t). Red dotted Lines Depict the Interval during which Percolation Drops Appear Continuously. Breakthrough and Steady-State-Flow Pressure Drops are Δp1 and Δp2, respectively.

Before the onset of percolation at B, the pressure varies linearly with the injected volume, Figure 12 (a) and (b). This linear behavior occurs only for an initially dry sample. However, if the sample was previously "trained" for invasion and still contains liquid in its interior, the pressure response was no longer linear, as illustrated in Figure 13.

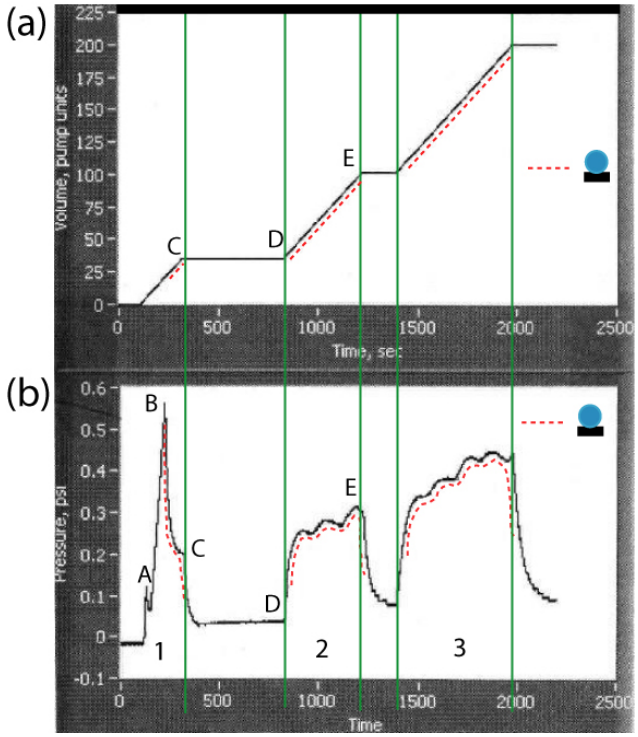

Figure 13. PV Data from Experiments in an Initially Dry sample up to Percolation, and Subsequent Experiments with Wetted Sample: (a) Injected Volume V(t); (b) Pressure P(t). The Red Dotted Lines Depict the Intervals during which Percolated Drops Appear Continuously. Interval (1) Depicted by the Phases A-B-C on the Pressure Plot Corresponds to Figure 3. Intervals (2) and (3) Show the Pressure Response in the Previously Wetted Sample.

The pressure response in the initially dry, (1), and in the previously percolated sample, (2) and (3), are noticeably different. The previously percolated (wetted) sample does not yield as high a breakthrough pressure threshold as in case (1). Also, droplets percolated at much lower pressure differences compared to region (1). The behavior presented in intervals (2) and (3) was new and had not been reported or documented in the literature to our knowledge.

Figure 14 illustrates typical data collected in PVI experiments in a new probing area but with the same batch of carbon paper samples. PVI experiments are generally “one run” tests that only work using dry samples. However, this method provides detailed dynamic information of the invasion process and complements the PV observations. The obvious advantage is the ability to monitor events in the interior part of the porous layer, though this is limited to a region in the vicinity of the upper surface of the sample. Figure 14 illustrates that the P(t) and V(t) data behaves similarly to the case presented on Figure 12 (b), but because the probing areas are different, the maxima of the pressure threshold are slightly different: ~0.55psi and ~0.72psi for Figure 12 and Figure 14, respectively. Part A-B of the curves is consistent with the data of Bazylak et al [5].

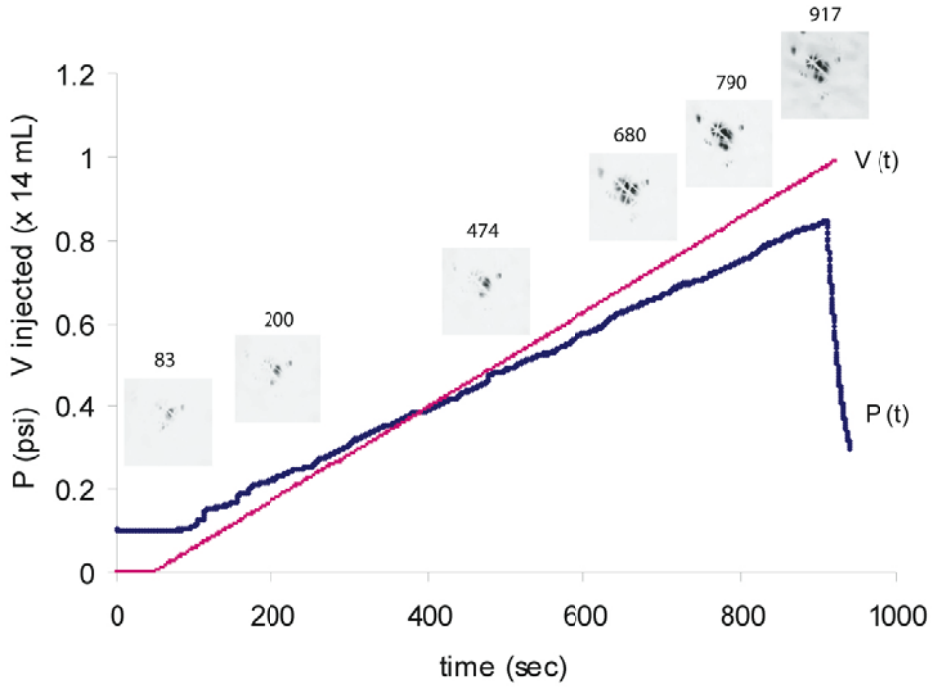

Figure 14. Pressure and Cumulative Injected Volume Traces under Constant Flow Conditions using an Initially Dry Sample. Fluorescence Microscopy Images at Various Times during the Process are shown above the Curves.

Analysis of the invasion images (samples shown in Figure 14) allows quantitative characterization of the invasion dynamics. All collected images were processed and characterized by one number representing the area of the recorded fluorescent cluster, and the resulting data is presented in Figure 15. The data in Figure 15 (c) demonstrates the abrupt change in regime between the initial slow invasion, and the subsequent rapid invasion. The other interesting observation from this data is that the invading cluster reaches quasi-saturation before the moment of percolation. Comparison of Figure 14 and Figure 15 shows that the change of the invasion dynamics does not affect the evolution of P(t) and V(t). These data are by nature integral representations of the process, whereas A(t) is a local parameter.

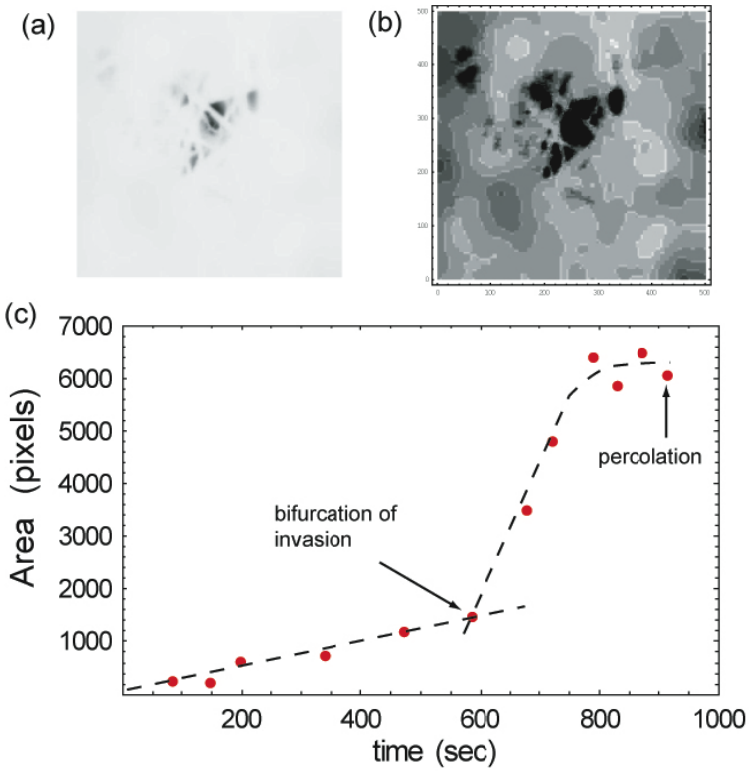

Figure 15. Dynamics of the Invaded Area during Period of Invasion of Layer near the Upper Surface of the Carbon Paper Sample: (a) Sample Raw Image; (b) Same Image after Preprocessing with the Thresholded Area of the Fluorescent Cluster – Shown in Black; (c) Area Data From 12 Images Corresponding to Different Times of the Invasion Process.

The results of the percolation studies were used to evaluate the LBM method for predicting the results water injection into and percolation through a GDL microstructure. The interfacial condition for the cell-scale models of cell performance was based on these results, particularly the observation of near uniform sub-surface saturation at the onset of percolation. That condition was selected to be no capillary pressure gradient in the GDL at the surface, as opposed to the commonly used zero capillary pressure condition.

4.1.5 GDL Surface Contact Angle and Accelerated Aging

Techverse attempted to experimentally simulate, and accelerate, aging of GDL materials. In these experiments, the GDL media were exposed to small electric currents, typical of a working PEM fuel cell, in one hour increments. Capillary pressure and water permeability characteristics of the exposed media, as well as the surface contact angles, were measured after each exposure period to determine the effect of current induced Teflon degradation or migration on the GDL properties. Scanning electron micrographs of the GDL surfaces after some aging experiments appeared to indicate migration of the Teflon in the direction of current flow. Continued imaging did not confirm that migration was occurring, but degradation of the hydrophobic treatment was consistently observed. In general, all media exhibited loss of hydrophobicity as a result of electric current evidenced by decrease in surface contact angles for both the carbon and MPL sides of the media as well as decrease in the capillary breakthrough pressures. The current exposure also resulted in marked increase in water permeability of the media. As expected, the

change in the properties was greater with greater initial Teflon loading. The capillary pressure measurements indicated that there was a substantial decrease in breakthrough pressure occurring within the first three hours of current exposure for all the media tested.

Figure 16 compares the carbon paper side contact angles of representative GDL media with different Teflon loadings. Contact angles were measured by varying the inclination of a sample with respect to gravity, while monitoring both the variation in shape of water droplets on the media surface and the inclination angle at which the droplet began to slide. All three media exhibited a decrease in contact angle over prolonged exposure.

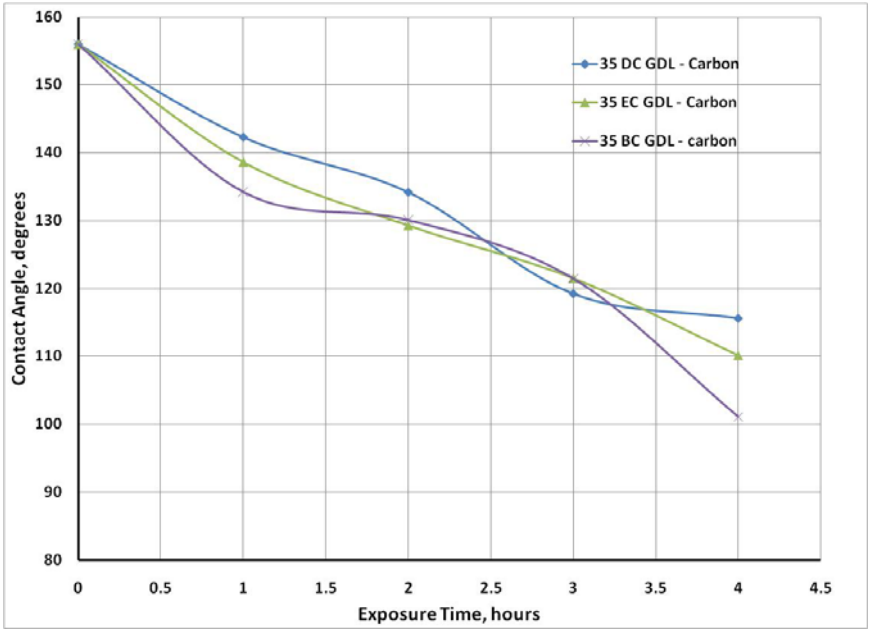

Figure 16. Contact Angles for the Carbon Paper Surface for GDLs with Varying Teflon Loading

Capillary pressure experiments were also performed on the GDL media samples exposed to electric current after each hour increment of exposure to an electrical current. The experimental apparatus and procedure used by Techverse to conduct capillary measurements is described above. At least 1 imbibition and drainage cycle was typically conducted before observing breakthrough in the media. Figure 17 depicts the breakthrough pressures observed for the SGL Carbon 35 series tested samples at each hourly increment. Since breakthrough pressures were observed to be highly influenced by the numerous cracks in the MPL on the GDL media, it is best to compare the intrinsic changes within each media as opposed to comparing the differences in the different media.

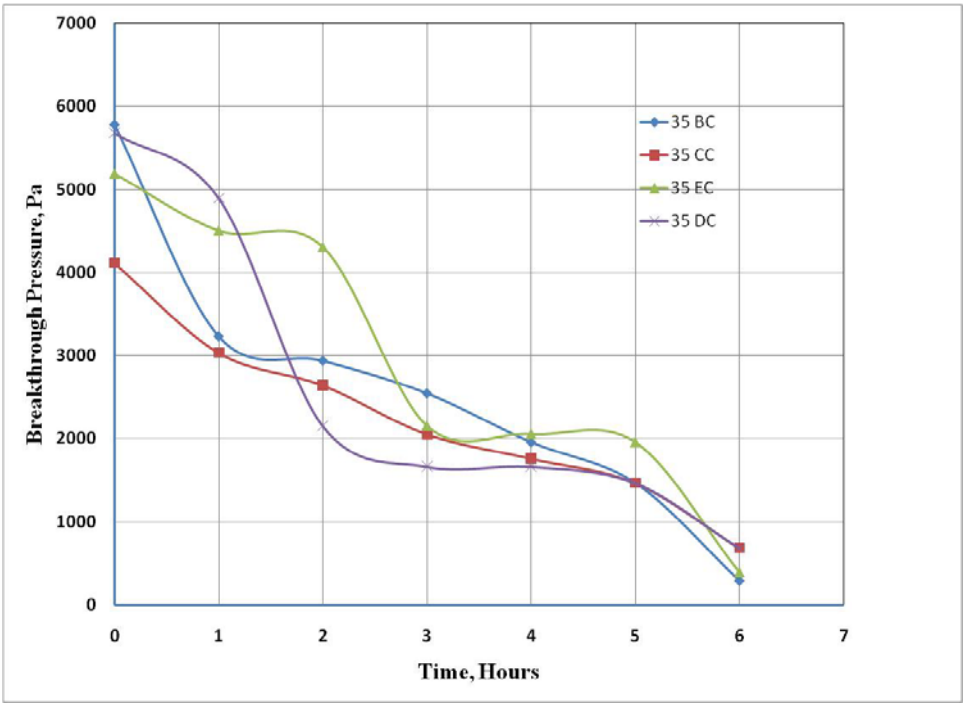

Figure 17. Comparison of Breakthrough Pressure for different Teflon Loading GDLs

In the initial aging experiments performed by Techverse, the GDL media were exposed to 1.5 V. There were concerns that this was not a realistic voltage to use, since an optimum fuel cell would run at a much lower voltage. The experiments were repeated by exposing 35 EC GDL paper, provided by SGL Carbon, to 0.75 V and 1.5 V. 35 EC paper exposed only to water for the same amount of time as the dampening process was used as a control. The control was added due to Los Alamos National Lab demonstrating that GDL paper will lose hydrophobic properties when exposed to water over an extended period of time. The loss of hydrophobicity was demonstrated by an increasing angle of inclination required to slide off a drop of water placed on the surface. During this repeat analysis, the rate of hydrophobic loss was verified to increase with increased voltage. The 1.5 V sample lost all hydrophobic properties on the carbon side after being exposed for only 11 hours, whereas the .75 V sample lost all hydrophobic properties after 19 hours. The carbon side of the 35 EC paper exposed only to water still had some hydrophobic properties after being exposed for 20 hours. The hydrophobic properties on the MPL side decreased at a faster rate for the samples exposed to a current than the GDL side. This trend was not the case with the control sample.

Based on the initial SEM images of material subjected to this aging protocol, and the possibility that the Teflon coating was migrating due to the imposed electric field, Techverse devised an alternate approach to alter the hydrophobicity of GDL materials. The developed technique appears to provide much more uniform Teflon coating of the GDL fibers than typical solution based impregnation methods, and is described below in Section 4.6.2.

4.2 Cell and Stack Water Management

4.2.1 Water Transport in Channels and Non-Operational Cells

Droplet Dynamics in Microchannels

As noted above, the formation of water droplets on the GDL surface and subsequent removal of the water through the channel was deemed to be an important, poorly characterized process. The droplet formation and detachment can have an impact on cell performance, through blocking reactant gas diffusion into the GDL and by hindering flow of reactants into the channel. In order to better understand these phenomena, and to provide data for evaluation of the cell-scale water transport models, the University of Victoria contributed experimental studies of water droplet dynamics in microchannels that emulate a fuel cell channel. Controlled, well-characterized surfaces were used to investigate the emergence, detachment and subsequent dynamic evolution of water droplets emerging from pores into microchannels.

The droplet dynamics studies were performed using microfluidic chips and high-speed flow visualization experiments. The development of various quantitative image analysis tools was undertaken and applied to the images to document the time evolution of the shape and location of the droplets. The microfluidic chip platform (Chip-V0) built previously by Minor [6] was used as the basis, with improvements in chip design and analysis tools throughout the study.

To ensure dimensions that are consistent model with the pore size of the GDL in PEMFC, a Chip V1 design with a 50μm square pore and 250μm gas channel was fabricated. The square geometry is computationally more convenient to reproduce without requiring grid skewing or unacceptable grid aspect ratios, and should exhibit all the salient physical mechanisms and maintain the appropriate value range for the key non-dimensional parameters [Reynolds number for channel flow regime; capillary number for surface tension effects in the channel; Weber number for surface tension forces relative to emerging drop inertia; and Bond number for gravity forces relative to surface tension]. The chip orientation and the corresponding observation window provided different droplet dynamic information, such as contact angle measurement. Besides single and multiple pores, pressure measurement ports were also incorporated in this chip. The chip was fabricated using SU-8 photoresist soft lithography technology.

Characteristic results from a drop emergence study under conditions conducive to formation of discrete drops are shown below in Figure 18. The conditions were inlet pressure, P0, 16.34 psia; square water pore size 50 μm; square gas microchannel height 250 μm; water injection speed, V_W, 4 cm/s; and air velocity,V_A, 10 m/s. Image analysis was applied to extract droplet heights, chord lengths, advancing and receeding contact angles, and frequency of drop detachment.

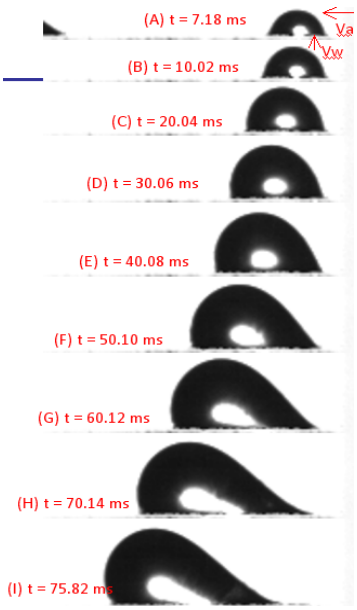

Figure 18. Representative Time Series of Images from a Drop Emergence Study

The trends with respect to observed contact angle hysteresis, air flow rates, and water flow rates are summarized as follows. In general, higher air flow velocities result in decreased contact angle hysteresis and promote droplet detachment in surface tension controlled regimes. A compilation of the data in the form of a flow regime map is shown below in Figure 19. With increasing water velocity, the region corresponding to droplet flow regime becomes smaller. At some point while increasing the superficial water velocity, the slug and film regime will intersect and thus the flow pattern might turn into an intermittent quasi single-phase liquid flow. The desirable operating states are expected to be at the higher air flows within the droplet regime. This promotes droplet detachment while preventing formation of water films on the GDL surface, with mass transfer inhibition, or slugs causing large pressure drops and pressure fluctuations.

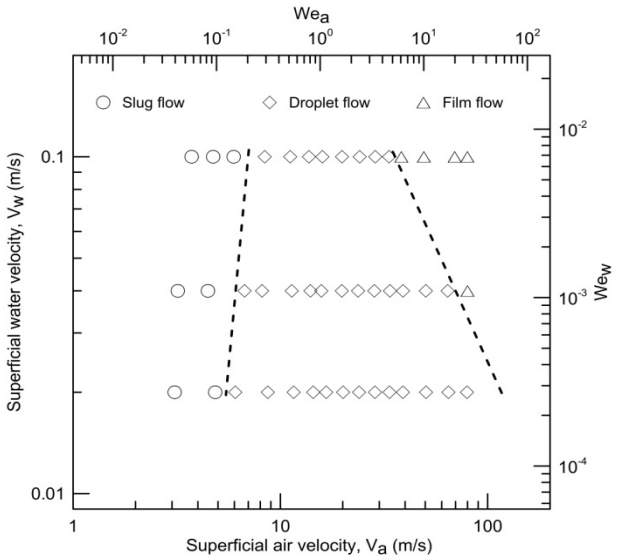

Figure 19. Flow Map based on Controlled Experiments Simulating Water Droplet Detachment in Cathode Microchannels

Pressure drop measurements were performed for a similar system with access ports to allow measurement at locations upstream and downstream of the water injection location, Figure 20. Figure 21 presents the pressure drop multiplier, ratio of wet and dry pressure drops between stations P0 and P3, for a range of air and water flow rates corresponding to typical fuel cell operating conditions. The largest values of Φ_g, at lower air velocities V_a and large error bars, correspond to the onset of slug flows with high water buildup and large fluctuations in the pressure drops. At high air velocities, the ratio approaches unity and the fluctuations decrease.

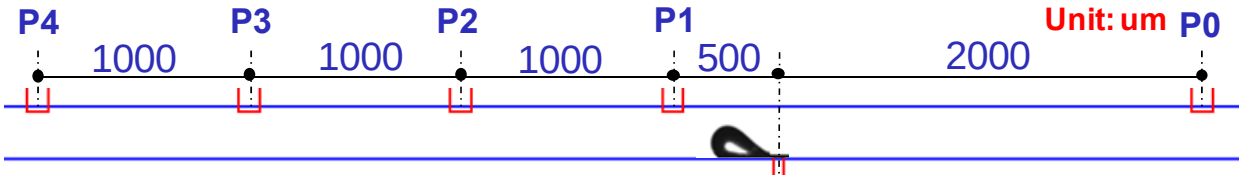

Figure 20. Schematic of Microchannel with Pressure Drop Measurement Ports and Representative Emerging Drop

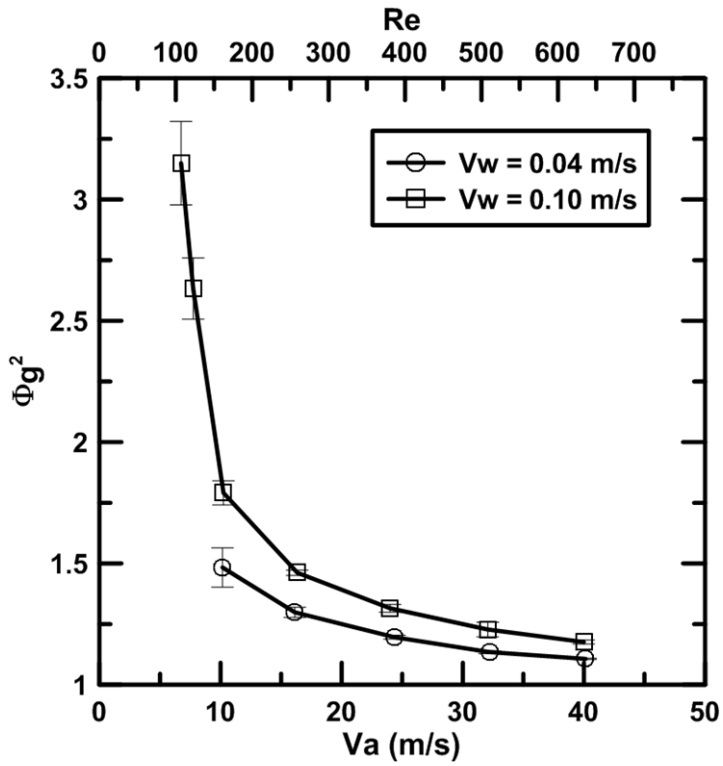

Figure 21. Two-Phase Pressure Drop Multiplier as a Function of Air and Water Flow Rates

The droplet emergence data and images were used to evaluate the two-phase flow capabilities of the cell-scale models, particularly the attempt to include surface tension forces in that model and predict formation of relatively large droplets as seen in the experimental studies.

Two-Phase Pressure Drop In Serpentine Channel Bipolar Plates

Techverse performed an experimental study to examine orientation effects on the water distribution and resulting pressure drops in the serpentine channel bipolar plate design used by

BCS Fuel Cells. It was anticipated that there would be sensitivity to the channel orientation with respect to gravity and the gas inlet location, due to the balance of the gravity body force and pressure required to drive the air through the channels.

In these two phase flow experiments, a GDL media was sandwiched between two Plexiglas plates; the air side plate consisting of flow channels and the water side plate consisting of a recessed cavity. The plates were fabricated with grooved channels to improve contact between the GDL media and the air side plate in the experiments reported here, after initial tests indicated that there was air leakage at the plate-GDL periphery. A single cell is simulated by placing a GDL media, SGL Carbon 35EC, between two Plexiglas plates with grooved flow channels. Both plates consist of three serpentine channels (a bipolar plate design typically used by project partner BCS Fuel Cells), where the GDL media is in full contact with channels on both plates. In one plate, compressed air is passed through the channels, and in the second plate, water is filled in the channels and is forced into the GDL media by applying a constant hydrostatic head. The four orientations considered are horizontal orientation with the water flowing either downwards or upwards, respectively, through the GDL media in to the channels and vertical cell orientation with the air flowing downwards and upwards in the channels respectively.

The observed two phase flow pressure drops for three of the four cell orientations studied are shown below. Figure 22 depicts the two phase flow pressure drop for the horizontal orientation with water flowing down into the GDL media. The pressure drop increases gradually with increasing water flow rate for all three air flow rates; however, after an initial pressure rise period, the pressure drop rise is much less for subsequent water flow rate increase. This phenomenon is due to the fact that two different fluid transport modes are taking place. In this orientation gravity has a direct impact in aiding the formation of the water droplet on the GDL surface as water emerges through the GDL due to hydrostatic pressure. At lower water flow rates the droplets tend to remain suspended longer providing a greater drag on the air flow causing the pressure drop to increase. As the water flow rate increases, droplets tend to detach quickly forming a film on the lower surface of the channels. At greater air velocities this change in the fluid flow behavior appears at lower water flow rates because the greater air momentum is able to detach the droplets at a smaller size.

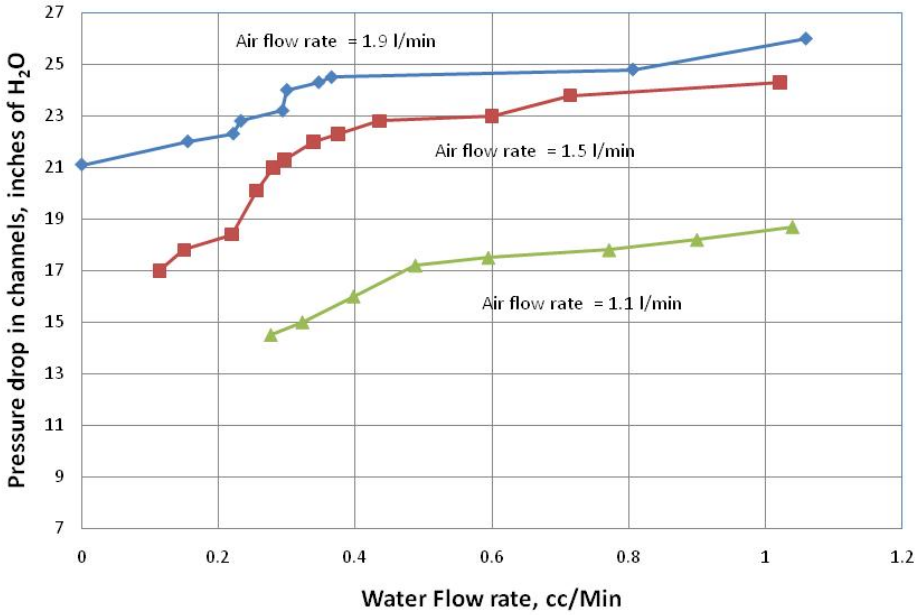

Figure 22. Horizontal Orientation with Water Flowing Downward Through the GDL

Figure 23 depicts the two phase flow pressure drop for the horizontal orientation with water flowing upwards through the GDL media. The pressure drop increases gradually with the water flow rate through the entire range for all three air flow rates as shown in the graph. This phenomenon is due to the fact that the water transport through the channels for this orientation is primarily as a thin film flow. The channels have water and air flowing in a parallel path as two layers, as opposed to a slug flow, which seems to be apparent only at the lowest air flow rate at low water flow rates. The channels farthest from the air inlet were always the first to become wetted because that region has the lowest air pressure. Increasing the hydrostatic head pressure on the GDL and subsequent increasing water flow rate correlates to increasing proportion of the channels becoming wet. Also at the lower air flow rate, a greater percentage of the channels appeared to become wetted due to corresponding lower air pressure.

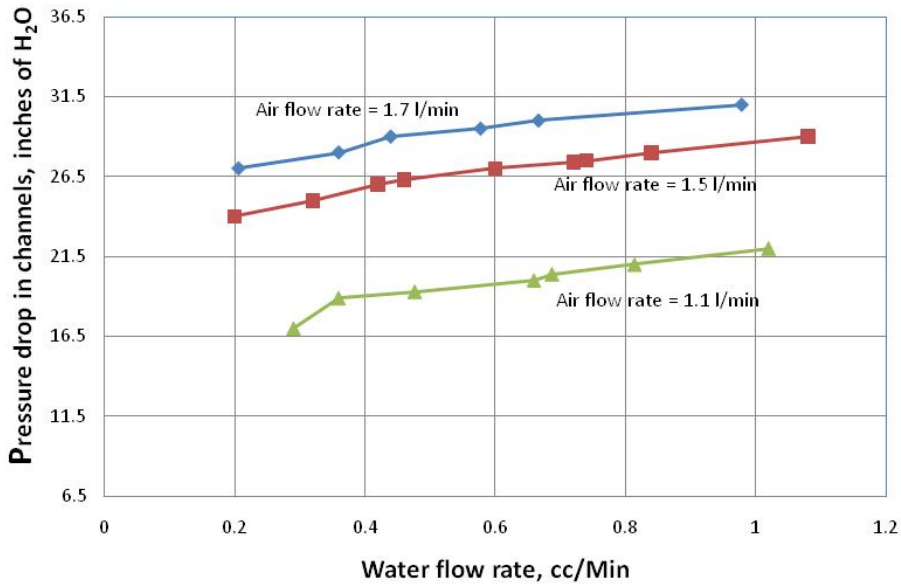

Figure 23. Horizontal Orientation with Water Flowing Upward Through the GDL

Figure 24 depicts the two phase flow pressure drop for the vertical orientation with the air flowing downwards. With this orientation, the transition from slug flow to thin film flow again becomes apparent for the lower water flow rates as in Figure 22. Because of the high hydrostatic head as well as lower air pressure in the lower segments of the channels, water seems to appear easily in the lower segments of the channels even at low water flow rates. At the same time due to high air pressure and lower hydrostatic head in the upper segment of the channels this part of the channels does not get wet even at high water flow rates. Both fluid transport phenomena appear to occur within the same channel as seen in Figure 25. At higher water flow rates, the fluid transport across all the channels becomes thin film flow type. The water phase is pulled to the bottom of the channel, and the air flows above the water allowing a portion of the air to remain in contact with the GDL media. With this orientation, air is likely to be able to make contact with the GDL media despite the channel being wetted. For the vertical orientation with the air flowing upwards through the channels, not shown, the transition from slug flow to thin film flow was not apparent. This orientation also appeared to exhibit the greatest pressure drop for the same air and water flow rate combination compared to other orientations since air needs to carry water upwards against the gravity. Unlike the vertical orientation with air flowing downwards the hydrostatic head is balanced by the air pressure for the entire channel area and thus greater percentage of channels appear to get wetted at higher water flow rates.

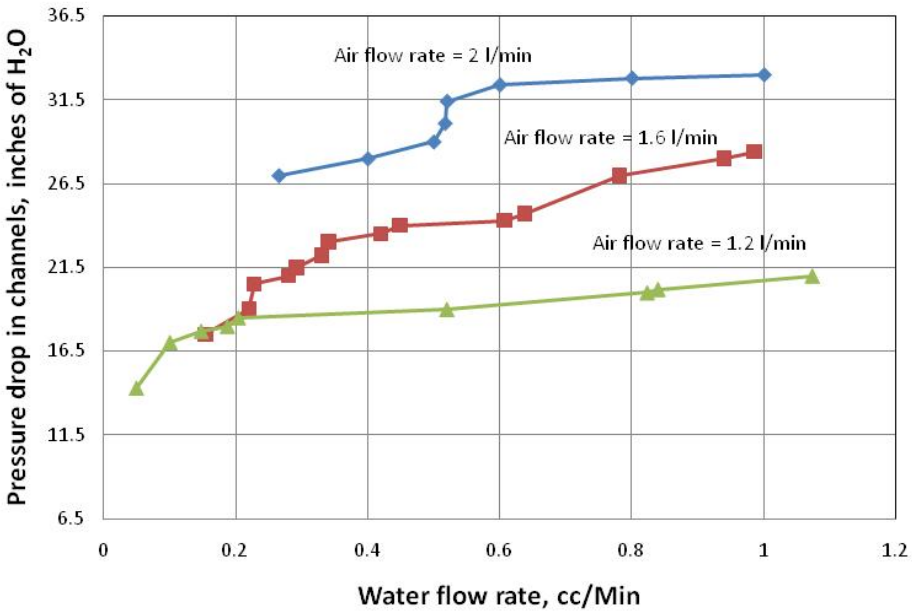

Figure 24. Vertical Orientation with Air Flowing Downward Through the Channels

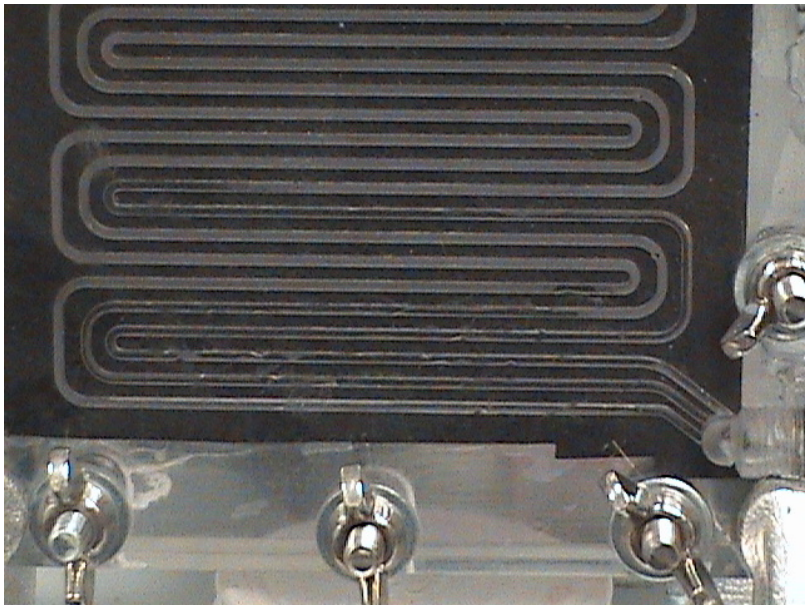

Figure 25. Slug and Thin Film Flow in Vertical Configuration with Air Flowing Downward

These experiments, particularly the case of Figure 22 with water flowing upward through a horizontal GDL were used to evaluate the cell-scale model performance for predicting water transport through the porous GDLs and two-phase flow pressure drops in serpentine channels.

Straight Channel Two-Phase Flow Pressure Drop

Ballard Power Systems developed a two-phase flow fixture capable of measuring the pressure drop in single channels with liquid water injection for different air flow rates to provide model

validation data for different channel designs. The two-phase flow fixture was a non-operational, isothermal, single channel apparatus capable of measuring local static pressures at a number of discrete locations along the channel length. The static pressure at the channel inlet and the channel outlet were measured using highly accurate pressure transducers. The static pressures along the channel length were measured with a reasonably accurate U-tube manometer set-up. The fixture could be operated with or without a porous GDL layer in contact with the channel. The fixture had the ability to control gas flow into the channel as well as the amount of liquid water injected into the channel. The liquid water could be injected either directly into the channel or first through a porous layer and into the channel. The location of liquid water injection could also be varied.

Initial data sets were obtained for a baseline channel design, with water injection into the top of the channel at a single upstream location. Total water flow rates were 11, 37, 56, and 75 microliters/min corresponding to the water generated at 0.3, 1, 1.5, and 2 A/cm2 current densities. The air flows chosen were 61, 204, 306, and 407 sccm, corresponding to stoichiometry 1.8 at each of the above currents. The system repeatability for injection of water at a single, upstream location was evaluated over this range of air and water flow rates, with typical run-to-run deviations within 5% of the average value. Representative data for the time-dependent pressure drops during two-phase flow operation of the test fixture, Figure 26, demonstrates the increased amplitude of the time variation as the water flow rate is reduced. At the higher air flow rates, Figure 27, the time variation is reduced for all but the lowest water flow rates.

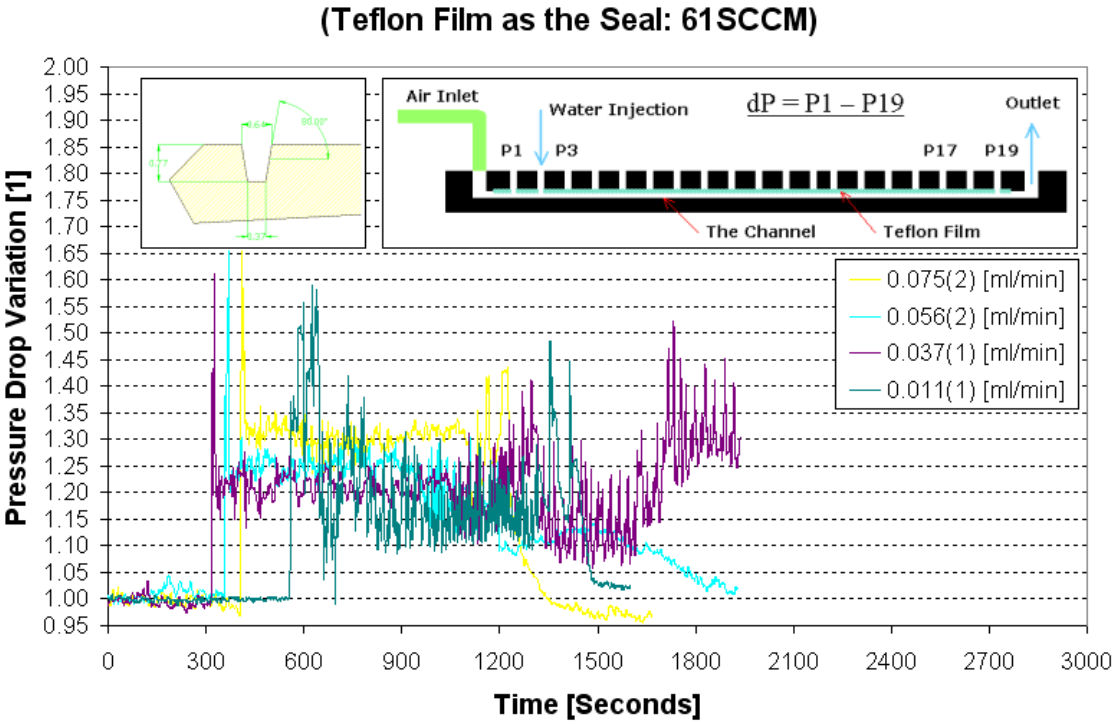

Figure 26. Observed Two-Phase Pressure Drop in Single-Channel Fixture at 61 sccm Air Flow, varying Water Flow. Channel Design and Test Fixture Schematics are Inset.

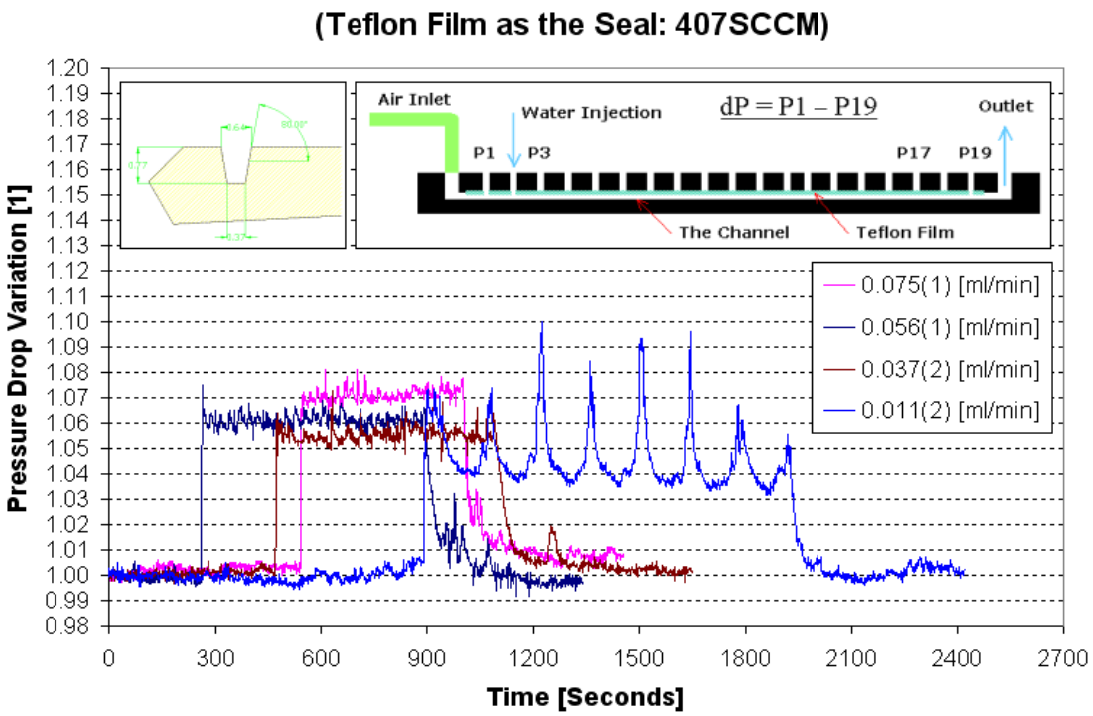

Figure 27. Observed Two-Phase Pressure Drop in Single-Channel Fixture at 407 sccm Air Flow, varying Water Flow. Channel Design and Test Fixture Schematics are Inset.

After the initial data acquisition, a second-generation 2-phase flow fixture (Gen II) was designed and used for further data generation. The purpose of the design iteration was to address key flaws in the Gen I fixture. Improvements that were made include the following:

- Proper liquid water removal in outlet channel port independent of fixture orientation.
- Channel flow visualization from the bottom of the channel and from the side of the channel.
- An increase in the number of pressure taps and liquid water injection sites.
- Alignment features for the channel and the porous layer.

Sample flow visualization results, obtained during initial testing of the Gen II fixture, are shown below in Figure 28.

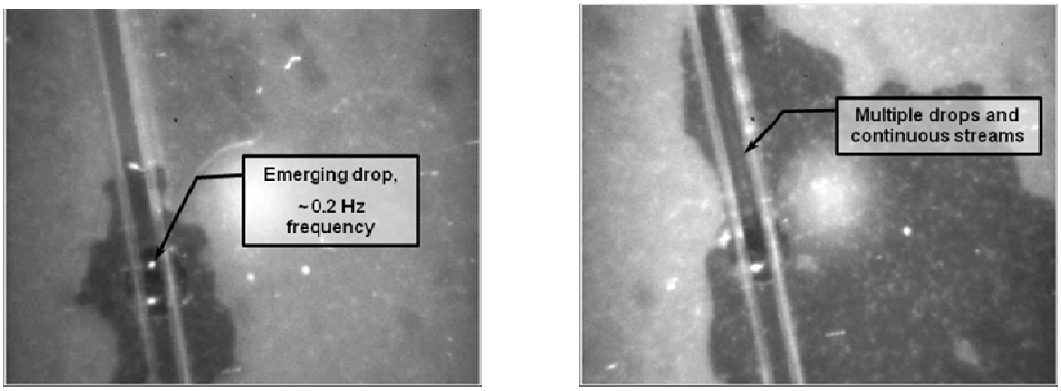

Figure 28. Initial Visualization from Gen II Fixture at Lowest (Left, 61sccm Air 0.011 ml/min Water), and Highest (Right, 407 sccm, 0.075 ml/min Water) Total Flow Rates

Channel pressure drop measurements were conducted for a range of liquid water injection rates, airflow rates and different porous materials [Teflon sheet, raw carbon fiber paper, and carbon fiber paper with carbon sub-layer(s). The experimental results for a single straight channel with carbon fiber paper can be found in Figure 29. The vertical axis in Figure 29 is the ratio of the wet channel pressure drop to the dry channel pressure drop for a given air flow rate and liquid water flow rate. For example, a value of "1.25" means that the wet channel pressure drop is 25% higher than the dry channel pressure drop for that set of operating conditions.

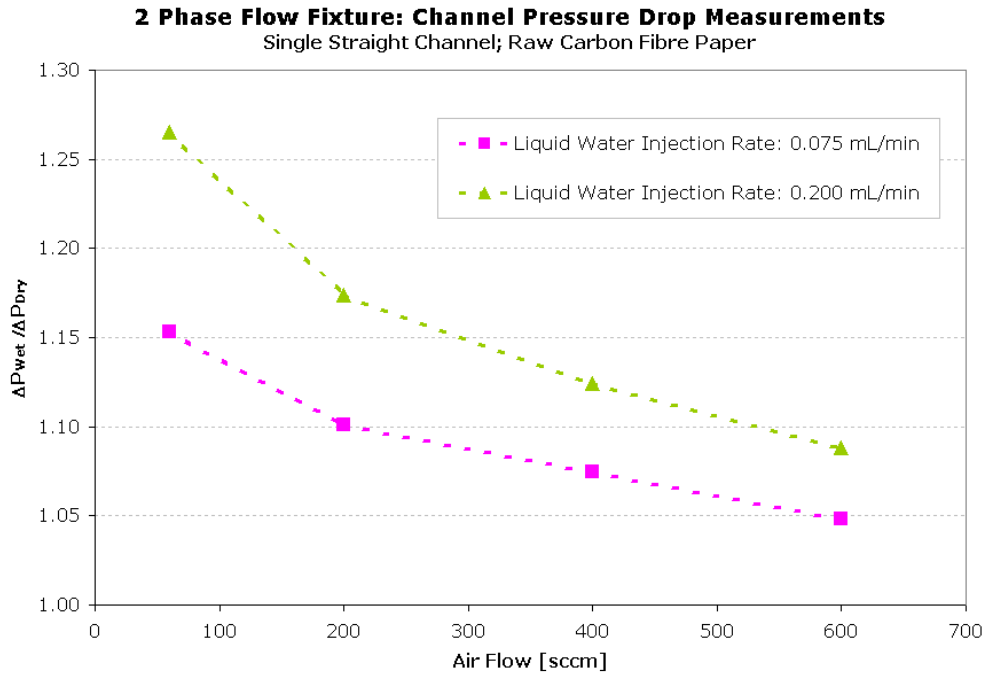

Figure 29. Wet Channel Pressure Drop Measurements

The final data set was used to evaluate the cell-scale two-phase flow model capabilities. In particular, this data was used to evaluate the ability of the model to correctly predict 'wet' pressure drops as a function of operating conditions and channel designs.

4.2.2 BCS Fuel Cells Self-Humidified Operational Cell Characterization

BCS Fuel Cells provided operational cell performance data on single cells and small cell stacks. This effort included development and assessment of a current interruption based measurement of cell internal resistance, characterization of performance variation with materials and operating condition variations, and assessment of freeze-thaw performance. The BCS Fuel Cells membrane electrode assemblies, MEAs, have been developed for self-humidified operation, and the cells use a serpentine flow channel. Therefore, it was anticipated that the data from BCS would provide valuable model testing due to the significant differences from the Ballard fuel cells described in later sections.

For self-humidified operation, the PEM fuel cell needs to be designed for and operated under conditions such that the water generated in the fuel cell is preserved as much as possible, and this water goes toward maintenance of a certain level of hydration of the membrane. The favorable conditions for self-humidified operations are lower temperatures, higher reactant pressures, lower stoichiometries of air flow, dead-ending operation of hydrogen with periodic release, and other parameters, such as cell design and material selections for fabricating the fuel cell.

Component Sensitivity Studies with Current Interruption

BCS Fuel Cells initially concentrated on establishing the method for resistance measurements in single fuel cells operated under self-humidified conditions. The initial development utilizes a Scribner Associates instrument (model #860) that detects IR drop across a fuel cell stack or a single fuel cell using the current interruption method. From such measurements, resistance R can be calculated by dividing the measured IR drop values by the current at which the fuel cell was operating. At the start of operation of a fuel cell, the internal resistance is high. As the fuel cell is conditioned, the resistance values drop and become stable. At some point during the operation of a fuel cell, an increase in resistance indicates a change in internal conditions of the fuel cell and a deviation from stable self-humidified operation. If the fuel cell is operated for some time under this condition of increased cell resistance, a failure of the fuel cell would eventually result.

A single-cell fixture using an electrode area of 25 cm^2 was chosen for establishing the method for resistance measurements and evaluating various membrane electrode assemblies. The catalyst loading on the cathode side is 0.5 mg/cm^2 Pt and on the anode side, 0.2 mg/cm^2 Pt. Typical conditions for measurement of polarization data are air pressure, 8 psig; hydrogen pressure, 3 psig; temperature, 60°C. The fuel cell was conditioned by operation at various current densities for about two days before measurements are taken.

Data were collected at air stoichiometry of 1.5, and hydrogen was dead-ended with periodic release every 30 seconds. Polarization data and internal resistance were measured for a cell using a Nafion 211 membrane and a second cell using a Nafion 212 membrane. The cell resistances for the two membranes are compared in Figure 30 as a function of cell current densities. For Nafion 212 membrane, the cell resistance is typically about 6 mohm, and for Nafion 211 membrane, typically about 4 mohm. This demonstrated the capability to identify the onset of stable, self-humidified operation through the internal resistance measurement.

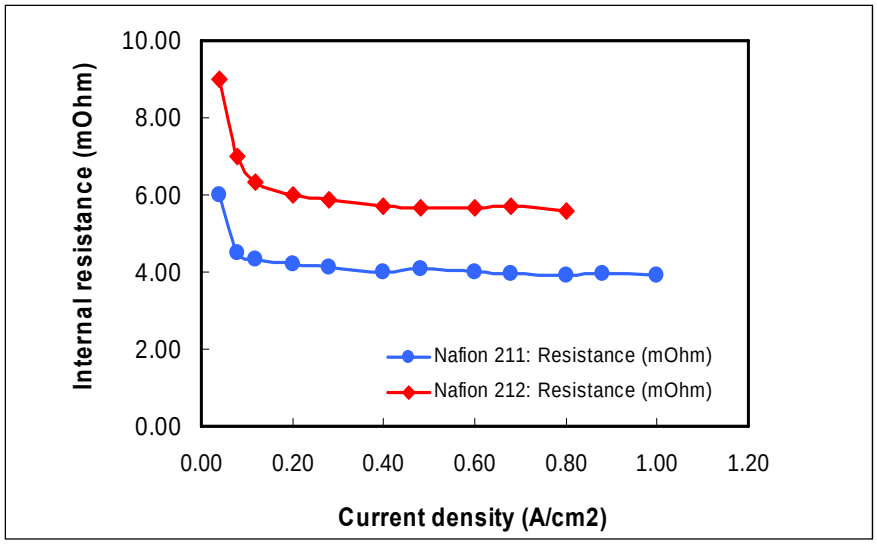

Figure 30. Variation of Cell Internal Resistance with Current Density for Two Membranes, Nafion 211 and Nafion 212. Operating Conditions: MEA Area: 25 Cm^2; Anode: 0.2 Mg/Cm^2 Pt; Cathode: 0.5 Mg/Cm^2 Pt; T: 60°C; Air Pressure: 8.0 Psig; H_2 Pressure: 3 Psig; Air Stoichiometry: 1.5; Dead-End Release Time For H_2: 30 s.

Figure 31 shows data at various temperatures from 45°C to 80°C, keeping the cell current constant at 15A and air stoichiometry at 1.0. Up to 70°C, the cell resistance remains stable, indicating that self-humidified operation is possible up to 70°C under the operational conditions. The cell resistance value starts increasing at about 75°C. This plot indicated that the initial MEA structure and fabrication should be improved, since the expected temperature effect on performance was not observed. It is noted that cell resistance declined with increasing temperature, and then becomes stable. The implication, therefore, is that at air stoichiometry of 1, the maximum temperature for self-humidified operation is about 70°C under the operational conditions.

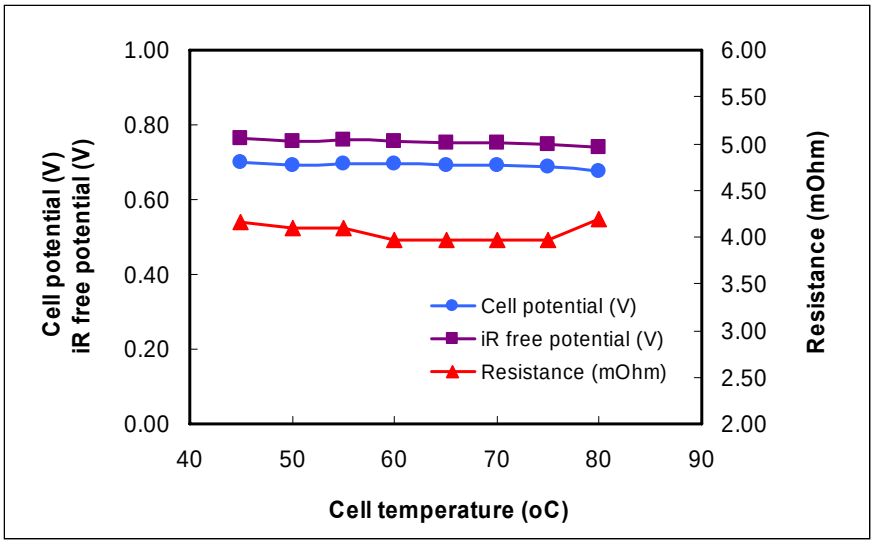

Figure 31. Effect of Temperatures on Cell Potential and Internal Resistance for Single Cell using Nafion 211 Membrane. At Current I=15 A. Operating Conditions: MEA Area: 25 Cm^2; Anode: 0.2 Mg/Cm^2 Pt; Cathode: 0.5 Mg/Cm^2 Pt; T: 60°c; Air Stoichiometry: 1.0; Air Pressure: 8.0 Psig; H_2 Pressure: 3 Psig; Dead-End Release Time for H_2: 30 S.

After the initial verification that the internal resistance technique was capable of providing additional insight into the hydration state of the membrane and catalyst layer, BCS evaluated the sensitivity of cell and short stack performance to a variety of parameters. These parameters included operating temperature, stoichiometries, GDL materials, catalyst loading, and air pressure. Representative data, demonstrating the capabilities of the current interruption technique, are shown in Figure 32 and Figure 33. Figure 33 shows polarization (V-I) and power plot (W-I) data at three different air pressures: 2, 8, and 13 psig of a BASF electrode designated as ETEK#1 with 5% Teflon content in the micro-porous layer, MPL. This electrode was designed to be susceptible to flooding, in order to further evaluate the internal resistance measurement capabilities. Hydrogen pressure was kept constant at 2 psig in all cases. Temperature was kept constant at 40ºC, and the air stoichiometry was kept constant at 1.25. The polarization data were extended to the extreme mass transfer region, with the cell current reaching up to 1.2 A/cm^2, and the cell potential dropping to below 0.10V. It is in the mass transfer control region that any observable effect of flooding would be noticed during the initial stages of electrode flooding. As both the micro- and macro-porous layers become more affected by the flooding, gradually, the effect can become pronounced in the kinetic and ohmic regions of the polarization plots.

Single-cell resistance data as a function of current density for this set of experiments are given in Figure 33. In addition to the initial decrease in resistance in the low current regime, a noticeable drop of the resistance values is observed in the mass transfer control regions. The dropping of the resistance values indicates a change in hydration level of the inner layer of the electrodes, and therefore, the onset of electrode flooding. Drop in resistance starts at a lower current density at a lower pressure, and at a higher air pressure at a higher current density. This behavior was expected based on the mass transfer phenomenon. The mass transfer to the electrode surface increases with increasing reactant pressure, and thus decreases the impact of liquid water on performance.

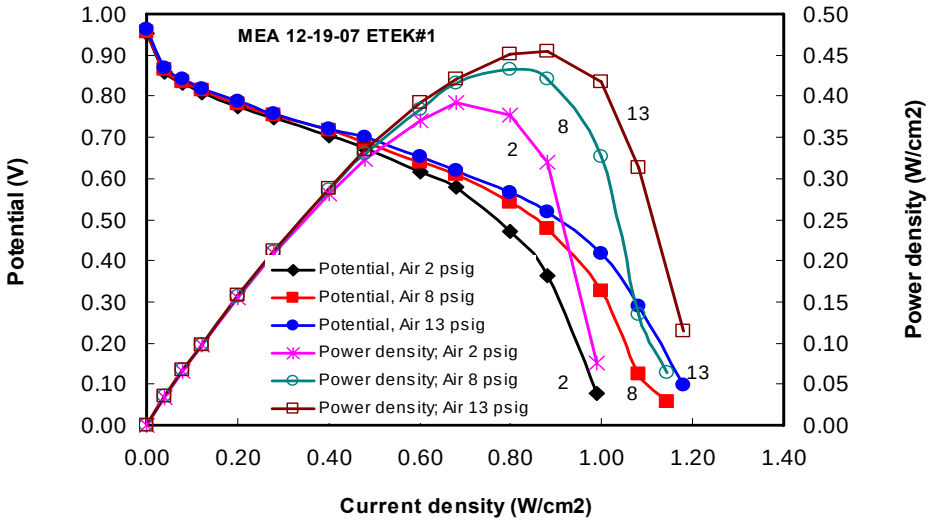

Figure 32. Effect of Air Pressure in the Range of 2 to 13 psig at Air Stoic of 1.25 and Temperature 40°C on Cell Performance using BASF Electrode Designated as ETEK#1. Operating Conditions: MEA area 25 cm^2; Anode: 0.2 mg/cm^2 Pt; Cathode: 0.5 mg/cm^2 Pt; H2 Pressure: 2 psig; Dead-End Holding Time for H_2: 30 s.

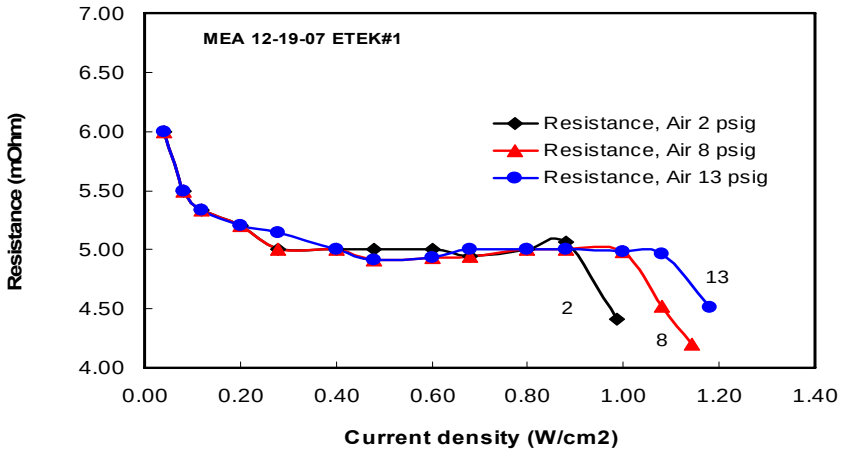

Figure 33. Effect of Air Pressure in the Range of 2 to 13 psig at Air Stoic of 1.25 and Temperature 40°C on Cell Resistance using BASF Electrode Designated as ETEK#1. Operating Conditions: MEA area 25 cm^2; Anode: 0.2 mg/cm^2 Pt; Cathode: 0.5 mg/cm^2 Pt; H2 Pressure: 2 psig; Dead-End Holding Time for H_2: 30 s.

The correlation of internal resistance with flooding had not been previously reported. This work indicated that internal resistance monitoring is a promising, simple technique for in-situ detection of electrode flooding with potential application to active control and cell-scale model validation.

An example characterization of the sensitivity of cell performance to materials and water management related properties is the following evaluation of a range of GDL materials provided by SGL Corporation. Single cells with electrode area 25 cm^2 were used in the measurements. Catalyst loadings on electrodes were 0.5 mg/cm^2 Pt on the cathode and 0.2 mg/cm^2 Pt on the

anode. The GDLS from SGL Carbon are carbon paper based and are designated as 10-BC, 10-CC, 10-DC, and 10-EC. The variable is the Teflon content (5% for BC to 30% for EC) in the macro-porous layer. The GDLs were Pt-catalyzed in house and MEAs were made with Nafion 212 membrane.

The single cell consisted of two plates etched with serpentine channels and is designated as BPFF-old. This is the cell, which has been in use as the standard cell in the laboratory. All operations were self-humidified without any added humidification to either reactant. Fuel cell performance data and cell internal resistance data were collected using a computerized instrument from Scribner Associates (Model 890C–1kW) having the capability of automatic IR-drop measurements with the current interruption technique.

Performance data in the form of V-I and power (W-I) plots for the four Pt-catalyzed gas diffusion layers of series 10 from SGL are given in Figure 34 at the temperature of 60°C and at air stoichiometry of 1.75. The significant differences in performance can be seen in the mass transfer control region. The kinetic and ohmic regions covering up to current density of 0.6 A/cm^2 show almost identical performance. In the mass transfer control region, the performances vary. The variations are now seen as following a trend within the scope of experimental variables. The sample 10BC having 5% Teflon content in the macro-porous layer shows the lowest performance in the mass transfer region, 10CC having 10% Teflon in the macro-porous layer shows the highest, and 10DC (20% Teflon) and 10EC (30% Teflon) are in the intermediate region. The performance in the diffusion control region can be interpreted to be related to the Teflon content in the macro-porous layer. The Teflon content of 10% in the macro-porous layer as in the sample 10CC represents an optimum value for this material, with the performance falling with the further increase of Teflon content due to inhibition of gas diffusion by the Teflon blocking open passages in the macro-porous layer.

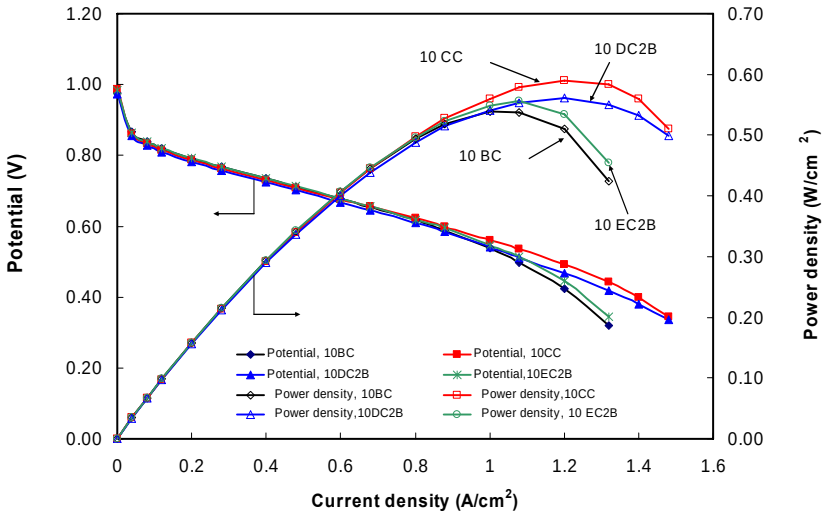

Figure 34. Comparative Polarization Data of SGL 10-Series GDL Materials with varying Macro-Porous Layer Teflon Content in the Range of 5% to 30 % At 60 ^{O}c and Air Stoic of 1.75. Operating Conditions: Electrode Area 25 cm^2; Anode: 0.2 mg/cm^2 Pt; cathode: 0.5 mg/cm^2 Pt; Air Pressure 8 psig; H_2 pressure: 3 psig; Dead-End Holding Time for H_2: 30 sec.

Figure 35 presents the internal cell resistance data as a function of current density. These data show reasonable consistency and trends between the samples. The data for samples 10BC and 10CC showing lower internal cell resistances, and the data for 10DC and 10EC showing higher values.

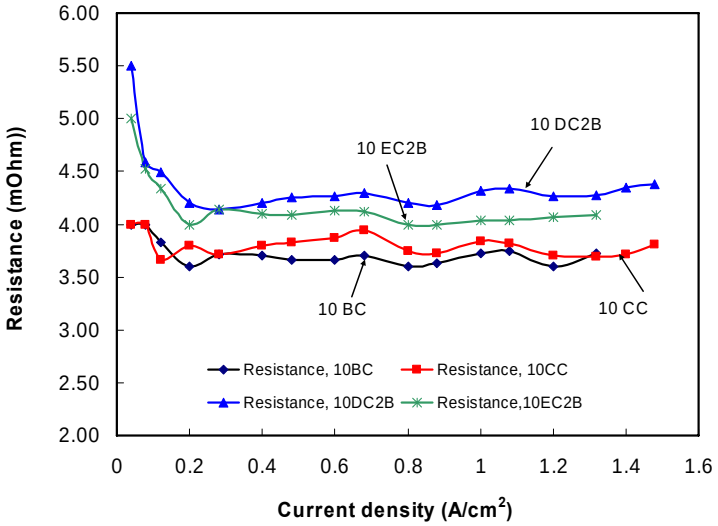

Figure 35. Internal Resistance Data Corresponding to Figure 34

Similar evaluations of additional SGL series 10 GDL samples with varying micro-porous layer Teflon content were performed by BCS. Unlike the macro-porous layer studies, there was a trend among all three samples with the best performance obtained from the material with the least micro-porous layer Teflon content. Based on internal resistance measurements at varying operating conditions, this is likely due to a similar trade-off between hydrophobicity of the GDL and gas phase mass transfer limitations imposed by excess Teflon, with the lowest Teflon loading in the microporous layer sufficient to maintain humidification in the catalyst layer and membrane.

Electrochemical Impedance Spectroscopy Studies

The characterization and improvement of the BCS Fuel Cells systems was planned to be based on polarization curve measurements, providing cell and stack power as a function of operating conditions, and simultaneous monitoring of the internal resistance as described above. Based on feedback received at the 2009 Annual Merit Review, these diagnostics were augmented by impedance spectroscopy measurements. The current interruption measurement of internal resistance is essentially a single frequency analogue of impedance spectroscopy, which provides the cell electrical impedance over a broad range of frequencies. Impedance spectroscopy does provide richer data, since it allows the researcher to identify relative changes in phenomena that respond rapidly to electrical perturbations, such as the electrochemical reaction kinetics, and those that respond more slowly such as the level of membrane hydration or the rate of reactant mass transfer through the GDL.

Impedance data is obtained in the forms of impedance vs. resistance, impedance vs. frequency, and phase angle vs. frequency. These basic plots are further analyzed to deduce and understand the characteristics of the electrode interfaces. The impedance data collected allows analysis of

impedance, capacitance, cell internal resistance, and (interfacial) resistance of the interface as function of current density, frequency of the sinusoidal signal. Interpretations of the capacitance and other data obtained from the impedance studies were expected to lead to better understanding of the state of the electrode interfaces in a fuel cell.

Initial experiments indicated that the current interruption and impedance spectroscopy techniques both allowed detection of the onset of flooding, with corresponding increases in the polarization resistance of the cell, Figure 36. In the complex-plane representation of the impedance behavior of a parallel RC circuit, the frequency corresponding to the top point of the semi-circular plot, ω(max), is related to capacitance by ω(max) = 1/RC. Figure 37 shows the plot of ω(max) as a function of current density for the same characterization experiment. For the first loop, attributed to the electrode kinetics, the characteristic frequency is identical at 40 and 60°C. For the second loop, attributed to diffusion of reactants through the GDL, the values are different at the two temperatures as a result of water condensation and the onset of flooding at the lower temperature.

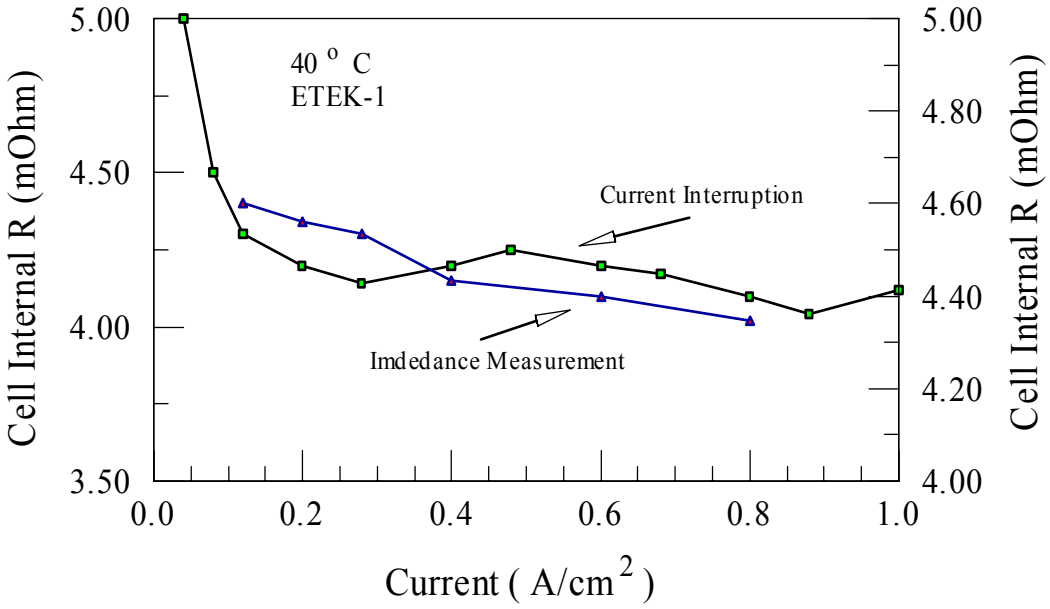

Figure 36. Comparison of Cell Internal Resistance Data Obtained by Current Interruption and Impedance Measurements Plotted versus Current Density. Electrode: BASF Experimental Electrode at 40°C.

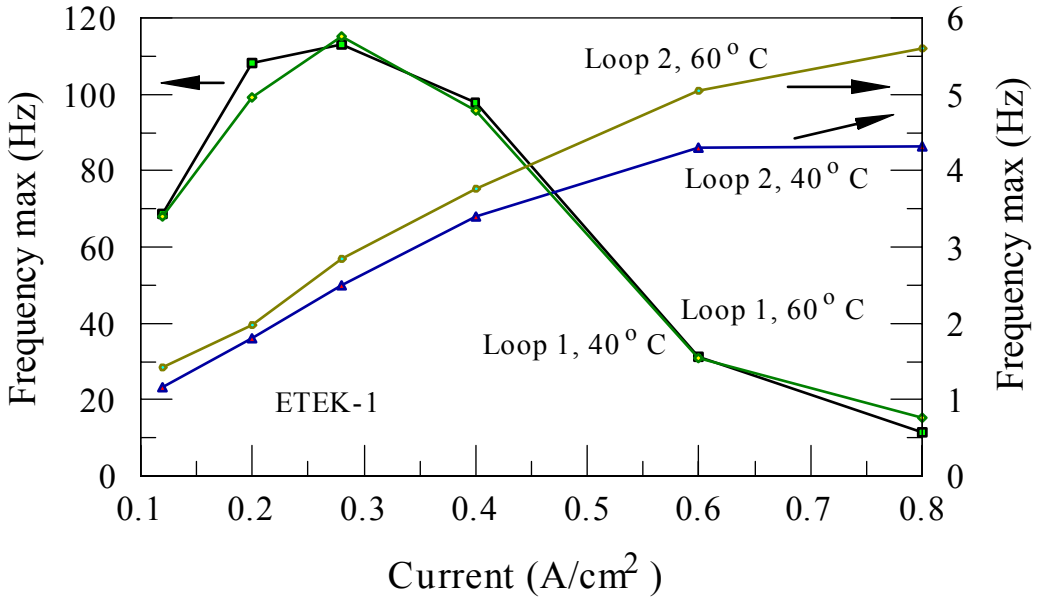

Figure 37. A Plot of Frequency Max as a Function of Current Density and Temperature for the Two Loops

BCS evaluated a number of commonly used equivalent circuit models to analyze the impedance data. These included a resistance in series with two RC circuits, and a similar model with the capacitor replaced by a constant phase element model to better capture the deviations from an ideal capacitor. The variation of fitted capacitance values, as a function of current density and frequency of electrical modulation producing the impedance data and the inability of the concept of an equivalent circuit containing a constant phase element, CPE, to explain the perfect circle-fit for the second loop led to the interpretation that the dispersive capacity in the CPE concept is not purely from mass transport through the porous electrode structure. The more plausible explanation was believed to be the importance of high surface area Pt catalyst for producing the first loop observed in the Nyquist impedance plots, and mostly the porous carbon electrode structure for producing the second loop. The variation of polarization resistance data versus time at temperatures 40° and 60°C and its interpretation indicated that at the lower temperature, physical flooding of the micro-porous layer occurs. These conclusions also agreed with earlier conclusions made from the stability data of the fuel cell using the same experimental GDL, designed to induce flooding, at the two temperatures mentioned above.

The impedance spectroscopy did provide additional details on the transition from electrochemical reaction limited performance to mass transfer limited performance in single cells and short stacks. This provided some guidance to BCS Fuel Cells as the program continued with evaluation of freeze/thaw cycling.

Freeze/Thaw Characterization

BCS planned to investigate the fundamental nature of damage resulting from freeze/thaw cycling in single cells and in cell stacks. This damage is closely related to water management, and one hypothesis of this program was that if strategies could be developed to control the physical location and distribution of water in a cell before freezing, the damage caused by ice formation could be mitigated.

Initial studies included development of a protocol to produce consistent results during the freeze-thaw cycling between normal operation and -20°C storage. This was followed by evaluation of start-up protocols from freezing conditions, both with and without external heating. Figure 38 presents FT startup data for the single cell and 4-cell stack. The applied current values during the startup period are shown in Figure 39, which also shows the rise in temperature during the startup period and up to 200 seconds. There was no external heating during the startup period in the stack. In spite of that, the startup period was within about 50 seconds, about the same time as for the single cell that had an external heating device. In Figure 39 it is observed that within 200 seconds the applied current was about 0.4 A/cm^2 and the rise in temperature was about 10°C. For the single cell, the temperature rise was about 15°C (not shown in the figure). At the stack level, startup was fairly quick and within 200 seconds the power level was about 0.25 W/cm^2 at the low temperature of about 10^{o}C.

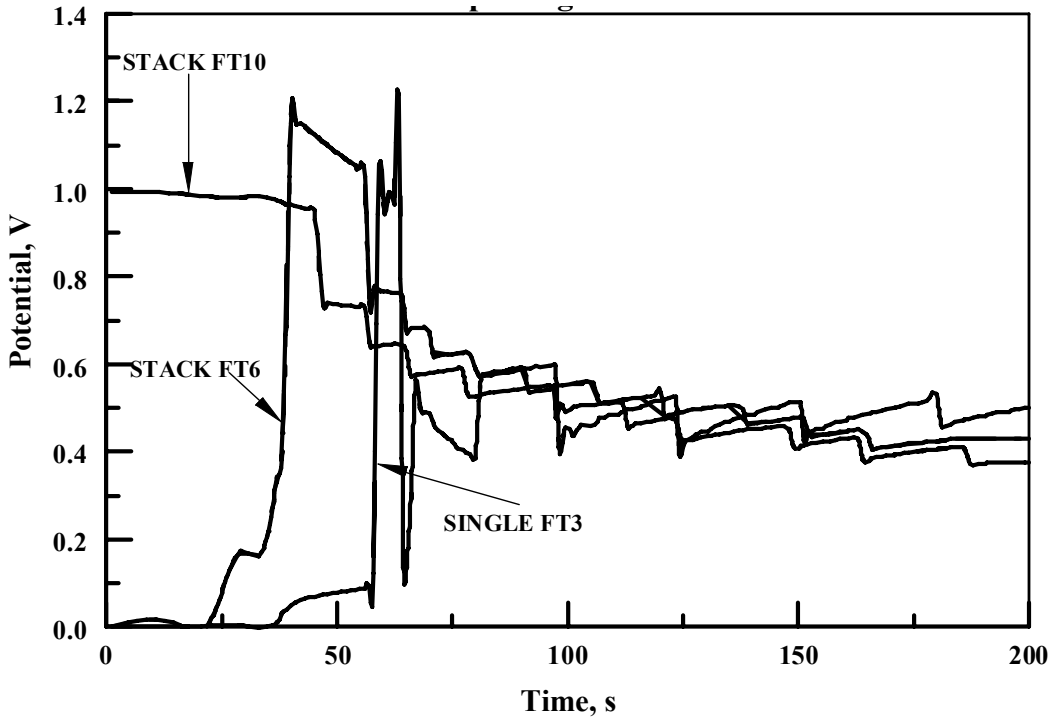

Figure 38. Cold Startup (Potential vs Time) Data for the Single Cell and 4-Cell Stack

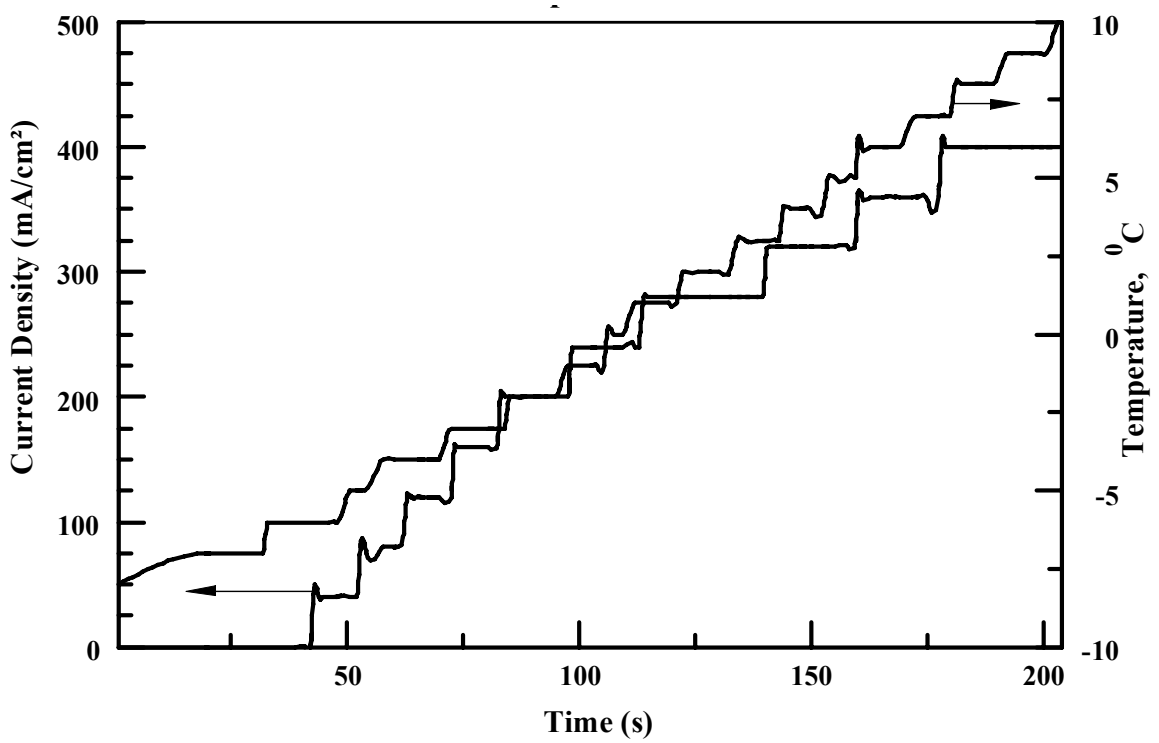

Figure 39. Cold Startup (Current Density and Temperature vs. Time) Data For the 4-Cell Stack

The trend of improved cold-start performance continued with the extension to a 10-cell stack. Figure 40 and Figure 41 show the startup data (current and potential scans) for the 4-cell and 10-cell stacks compared to that obtained previously for the single cell startup. It can be seen that the startup of the 10-cell stack occurs at least twice as fast as that of the 4-cell stack, and at least 4 times faster than of the single cell.

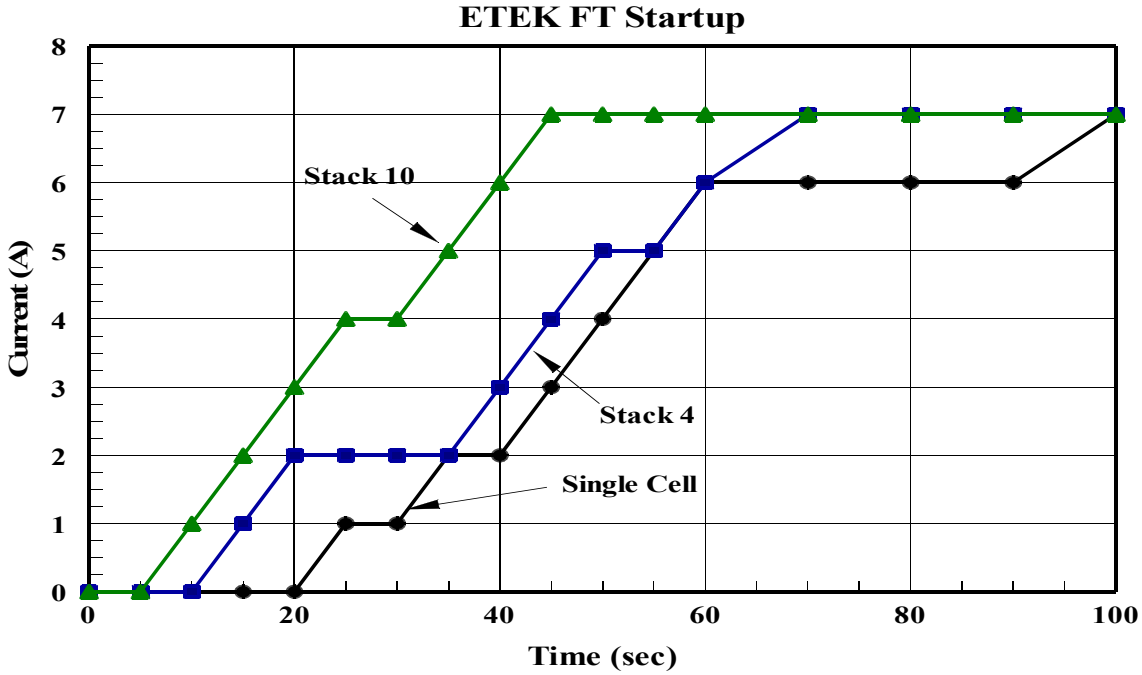

Figure 40. Cell-Applied Currents during the FT Startup for the Single Cell, 4-Cell Stack and 10-Cell Stack

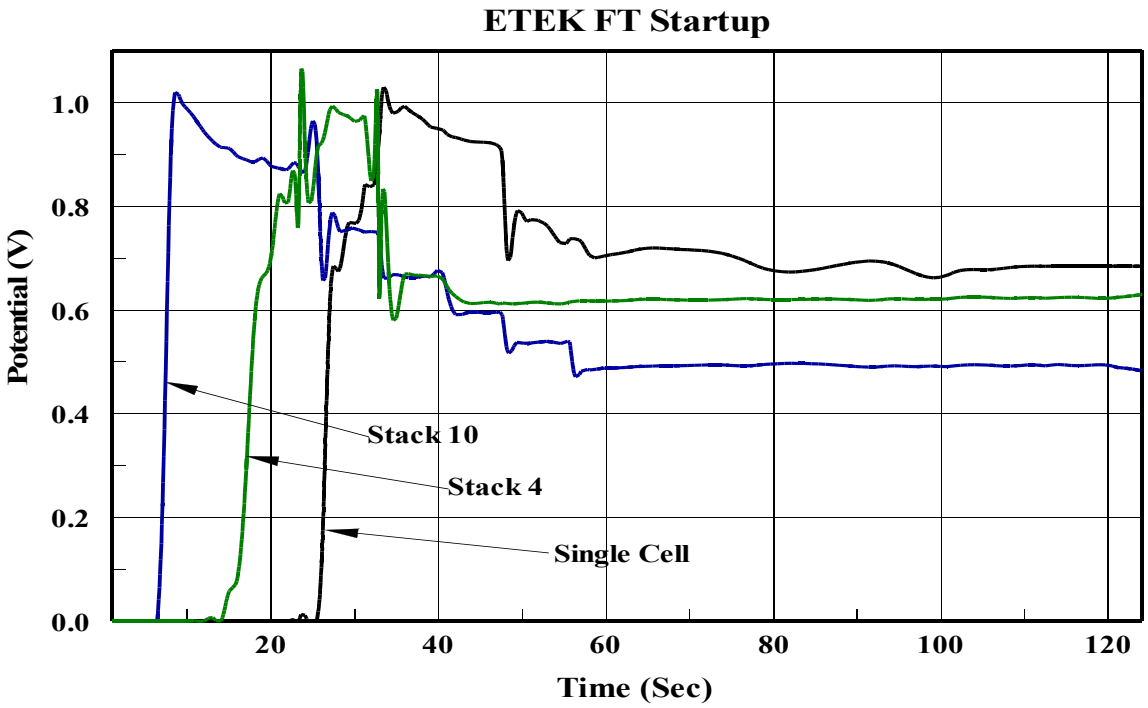

Figure 41. Cell Potentials during the FT Startup for the Single Cell, 4-Cell Stack and 10-Cell Stack

It can be seen from Figure 42 that the cell potentials (calculated as average values obtained before and after impedance measurements for each applied current, respectively), do not change for the values of applied current up to 7A. However, up to 20% drop could be observed for higher values of applied current. This effect could be explained by increasing hydration of the stack. It is also clearly seen that this decay in performance with freeze-thaw cycles is almost non-existing for the 10-cell stack. These differences were attributed to more uniform hydration and less local flooding occurring in the 10-cell stack relative to the smaller stack, consistent with trends observed in impedance spectroscopy measurements obtained under normal operation.

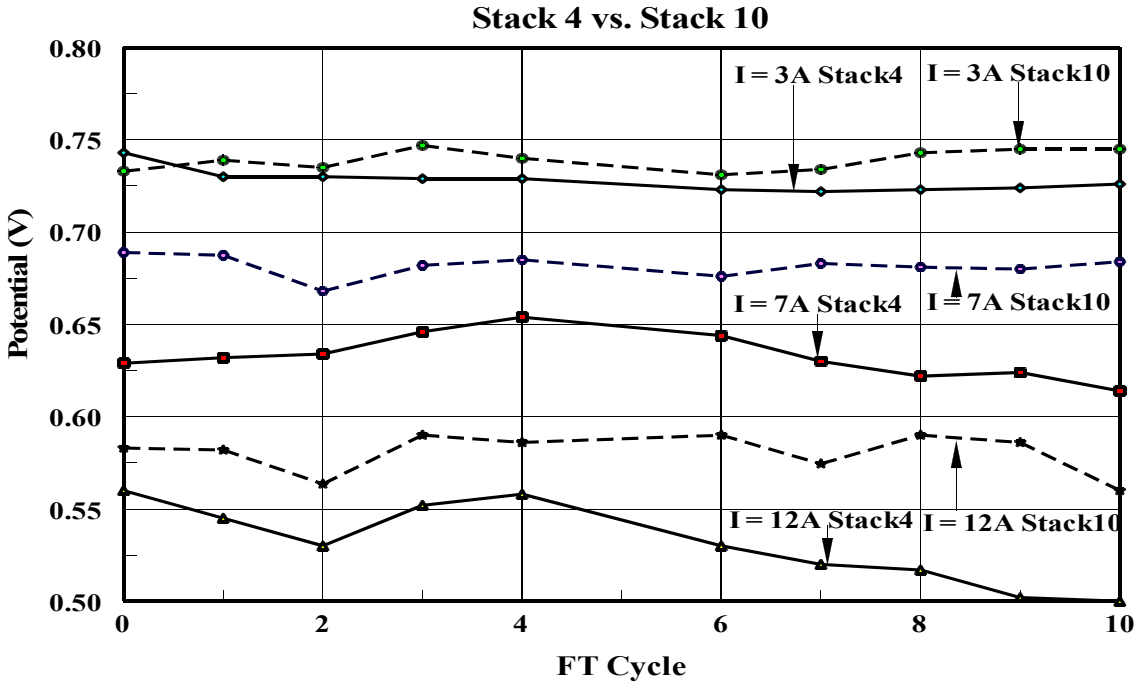

Figure 42. The Average Cell Potentials for the 4-Cell and 10-Cell Stacks for Freeze – Thaw Cycles 1 – 10

These activities did not provide any additional fundamental understanding into the water distribution at shut-down or after freezing, but did meet the objective of characterizing freeze-thaw performance in the self-humidified cells and result in improved freeze-thaw performance.

4.2.3 Ballard Operational Fuel Cell Diagnostic Data

Shortly after the project initiation, Ballard Power Systems compiled an updated model validation data package which included both detailed ex-situ material characterization data for properties and in-situ cell diagnostic data for performance, cell current distribution, MEA water distribution and water cross-over data. This data pack was delivered to CFDRC three months after the project start. The data pack was a selection of experimental data that is intended for model input and validation to improve fuel cell modeling capability. The data pack also clearly identified Ballard standard model input parameters for fuel simulations, including Ballard internally measured values in many cases and literature values if measurements were not available internally.

Some salient features of this comprehensive data set are described below:

- Complete description of model input parameters with confidence levels
- Complete geometrical description of the cell/channel geometry
- Brief description of the experimental setup and MEA parameters
- Description of the operating conditions used for measurements
- Experimental results on performance, current maps, stoichiometry sensitivity, RH sensitivity demonstrating the hydration/dehydration effects
- MEA water content characterization and water content breakdown in different layers of the MEA using 10 cell stack measurements
- Measured water cross-over data using the above 10 cell stack
- Single cell measured data on oxidant, fuel and coolant pressure drops as well as water crossover data in an operating cell.

During the course of the project, much of the Ballard diagnostics effort was focused on materials characterization and the water transport studies described above. In addition to those studies, Ballard and CFDRC jointly designed a set of experiments for additional diagnostic data. These experiments were focused on cell performance, MEA water content characterization, and current maps as a function of expected water content. Independent variables included inlet humidity for both air and fuel gas streams, operating temperature, and target current density. Ballard performed those experiments and delivered the resulting data to CFDRC during the fourth year of the project. Complementary data on electrochemical kinetics, gathered in a test fixture designed to operate at high reactant flow rates and uniform temperature for uniform conditions along the length of the cell, were also provided.

These two data sets provided the primary source of experimental results for evaluating the capabilities of the cell-scale water transport and fuel cell performance model. Sample data is included below in the discussion of model validation.

4.3 Model Development

4.3.1 Lattice Boltzmann Method Model

Development and evaluation of a Lattice Boltzmann Method, LBM, model for simulation of single-phase and two-phase flow within GDL microstructures was intended to address several challenges in understanding water transport within fuel cells. In-situ diagnostics are challenging as the medium is thin (200 – 300μm) and optically opaque (graphitic carbon). Numerical modeling efforts typically use fitting to Darcy's Law for permeability effects and the Leverett function for capillary pressure. The Lattice Boltzmann Method provided a promising approach for developing predictive models of transport in GDLs and related porous media, enabling materials design on the microscale and providing effective transport properties that could be used in cell-scale models.

LBM can be understood as a simplified solution of the Boltzmann equation, using a swarm of hypothetical particles that exist on a lattice with the permissible velocity directions and magnitudes constrained to a handful of discrete values. During simulation, the distribution of particles is updated by first streaming, or flowing, between lattice nodes based on the initial distribution. A collision process is then simulated, resulting in updated velocity distributions at each lattice node. The streaming captures the effects of fluid convection, and the collision processes emulate actual molecular scale collisions to produce viscous effects. LBM has been widely studied and peer reviewed. Advantages are that the kinetic theory basis of the method allows simple implementation of molecular forces responsible for liquid-gas phase separation and capillary effects. The solution algorithms make the LBM suitable for domains with complex boundaries such as the interior of a porous GDL material. Weaknesses arise from the formulations used for the collision processes, which can result in intractable simulation times for models that accurately capture intermolecular forces with very short relaxation time scales.

The governing equation is the well-known Boltzmann-transport equation (BTE) given by,

$$\frac{Df(\mathbf{x},\boldsymbol{\xi},t)}{Dt} = \frac{\partial f}{\partial t} + \boldsymbol{\xi}.\nabla f + \mathbf{F}.\nabla_{\xi} f = \left(\frac{\partial f}{\partial t}\right)_{coll} \qquad [1]$$

Here, f is the probability distribution function describing the distribution of particle population over velocities $\boldsymbol{\xi}$, at location $\mathbf{x}$ and at time t. The right side of the equation is the change in f due to intermolecular collisions. It is related to local density ρ and momentum $\rho\mathbf{u}$ as,

$$\rho(\mathbf{x},t) = \int f(\mathbf{x},\boldsymbol{\xi},t)d\boldsymbol{\xi} \quad [2]$$

$$\rho(\mathbf{x},t)\mathbf{u}(\mathbf{x},t) = \int f(\mathbf{x},\boldsymbol{\xi},t)\boldsymbol{\xi}d\boldsymbol{\xi} \quad [3]$$

In LBM, the collision is typically modeled by the Bhatanagher-Gross-Krook (BGK) model [7]

$$\left(\frac{\partial f}{\partial t}\right)_{coll} = -\frac{f - f^{eq}}{\lambda} \quad [4]$$

which assumes that particle distributions approach local equilibrium linearly over a characteristic time λ. This characteristic time is related to the fluid viscosity ν. This model has well-known limitations in applications such as multiphase and porous media flow. In particular, employing the BGK model in porous-media flow results in a viscosity dependence of the computed permeability. Hence, in this work, a multiple-relaxation-time (MRT) collision model is implemented [8]. In the MRT model, the single relaxation time λ is replaced by a collision-matrix given by,

$$\left(\frac{\partial f_\alpha}{\partial t}\right)_{coll} = -\Lambda_{\alpha\beta}(f_\beta - f_\beta^{eq}) \quad [5]$$

Here, α, β corresponds to particle velocities $\boldsymbol{\xi}_\alpha$ and $\boldsymbol{\xi}_\beta$, respectively. Employing the collision-matrix allows separation of relaxation time-scales between hydrodynamic modes such as velocity, pressure and stress-tensors, thus improving numerical accuracy and stability.

The multiphase LBM model was based on the work of He *et al*. [9], in which the mean-molecular interaction force $\mathbf{F}$ is formulated as the sum of phase segregation and surface tension forces. The phase segregation force is expressed as the gradient of the non-ideal part of the equation-of-states (EOS), which separates the fluid into respective liquid and gas phase densities, by entropy minimization. The surface tension force depends on the interfacial curvature and is scaled by the strength of the molecular interaction.

In numerical implementation, two separate distribution functions are used. One distribution function f is for a phase-tracking variable, known as the index function, φ. The transport equation of f recovers an advection-diffusion equation known as the Cahn-Hilliard equation. Transition of φ from the limiting values at the liquid to gas phase is spread over a finite number of lattice nodes. The interface is implicitly defined as the contour of φ having the average of these limiting values. Fluid properties such as density and viscosity are interpolated from φ. A second distribution function g is used to compute pressure and momentum. The transport equation of g recovers the Navier-stokes equation with a surface tension term. The surface tension is computed

from φ as proportional to $\varphi\nabla\nabla^2\varphi$. In this work, the first and second-order derivatives are computed as weighted sum of the second-order central difference along the lattice-velocity directions. The limiting values of φ are obtained analytically from the EOS and can be further refined from the simulation of liquid film or drop equilibration.

Solid surface wettability and contact angle effects were modeled by Mukherjee et al. [10] by adding an external force near the surface. This force was designed to mimic molecular attraction/repulsion between fluid drop molecules and solid surface molecules as,

$$\mathbf{F}_w = -K_w \varphi_l \mathbf{n}_s \qquad [6]$$

Here, K_w is the strength of interaction parameter and $\mathbf{n}_s$ is the surface normal. In this work, we employed a similar model by Yiotis et al. [11] due to its simpler implementation on complex boundaries such as randomly oriented GDL fibers. They assign a φ value to the solid between liquid and gas limit to compute surface tension forces.

A modeling approach was also developed to generate microstructures representative of GDL materials, in order to provide geometric data input to the LBM simulations. The GDL microstructure of non-woven carbon paper was generated by simulating laying fixed diameter, continuous, cylindrical fibers in parallel planes. Within a plane the fibers are randomly orientated and may intersect each other. This approach is similar to that reported by Schulz et al. [12]. In this work, the spacing between parallel planes was typically assumed to be equal to the fiber diameter.

Performance criteria for the LBM models were as follows. The single-phase LBM models were to be verified by comparison to relevant single-phase flow benchmarks, including:

- Couette flow between parallel plates;
- Lid driven cavity flow; and
- CFD analyses of benchmark models for single-phase flow with heat transfer.

When the LBM model was demonstrated to perform adequately against the above single-phase flow metrics, the two-phase capability would be developed and verified using the metrics for the continuum model of two-phase flow in porous media, namely

- Ex-situ observations of capillary wicking, and
- Ex-situ observations of the relationship between pressure drop and mass flux.
- After satisfactory verification against the ex-situ two-phase flow experiments, additional verification will be performed against Ballard data for water transport in fuel cell geometries.

Hardware requirements for the LBM are primarily driven by memory requirements, as dictated by the resolution of the velocity distribution and the number of lattice nodes. Models shown in this report were simulated using Linux workstations with 2.2 GHz CPU speed and 4 GB of RAM memory. The software was parallelized using domain decomposition techniques, and demonstrated linear speed scaling up to 8 processors.

4.3.2 Cell Scale Multiphysics Model

To enable model-based design and optimization of PEM fuel cells, models must address a broad range of conditions including operation with significant liquid water in the channels. The model developed during this work represents an effort to address common deficiencies of previous model formulations, introducing a more general multiphase flow model that can serve as the basis for a design tool addressing water management. Earlier performance models have utilized computational fluid dynamics techniques, in conjunction with solution of gas phase chemical transport, heat transfer, and electrochemistry, to predict cell performance and the distribution of liquid water within the fuel cell. However, these models tend to simplify the impact of the liquid water on the solution, particularly in the channels where droplet formation and drag due to the liquid water is often neglected.

The cell scale model was intended to address these deficiencies, introducing a more general multiphase flow model that can serve as the basis for a design tool addressing water management. The model is based on the conservation equations for gas and liquid phase mass and momentum, each chemical species in the model, total enthalpy of the two-phase fluid mixture and solids, and electrical current in the membrane and solid phases. These governing equations are solved using a finite volume approach, in which the computational domain is divided into numerous control volumes and the governing differential equations are transformed into a nonlinear system of equations for each solution variable. The finite volume technique is well-established in the computational fluid dynamics community, and its application to solution of multiphysics problems including predicting fuel cell performance is well documented. The distinction of our approach is in the use of a true two-phase formulation for the gas and liquid flow in the fuel cell, solving for the phase fraction of the liquid water and the velocities of both phases in all portions of the model except solid regions.

The key assumption implicit in this approach are that adequate constitutive models for physical phenomena such as drag forces between the gas and liquid in the channels, capillary pressure forces in the porous media, and rates of phase change due to evaporation and condensation can be developed and implemented in a numerically stable fashion. The treatment of flow and liquid permeation across interfaces between porous and non-porous regions was also expected to be a potential weakness, as this was an area of ongoing research. To address these concerns, we planned to test the submodels independently against benchmark simulation results and experimental data gathered in a controlled fashion.

The metrics for success of the two-phase model simulating cell component component level were satisfactory prediction of:

- Water transport through GDL as measured at RTI for saturation model and capillary pressure functions
- Channel level transport against Ballard Flowviz data, adequate prediction of wet pressure drops in channels observed at BCS and Ballard,
- Droplet formation and transport trends consistent with ex-situ experiments and the Flowviz observations at Ballard, and
- Agreement with other researchers ex-situ observations (wicking experiments into GDL and ex-situ GDL+channel)

The performance metrics for steady state simulations were adequate prediction of trends and values of:

- Relative humidity profiles in the channels;
- Wet pressure drops in the channels;
- Temperature spatial distribution;
- Current and voltage spatial distribution;
- Membrane and GDL water spatial profiles;
- Sensitivity to operating pressure, temperature, and relative humidity; and
- Sensitivity to inlet stoichiometry.

The metrics for transient analysis will be adequate predictions of:

- Response to inlet drying and/or purging;
- Degradation associated with cell reversal and measured H_2O, CO_2 formation;
- Degradation at startup arising from in-plane galvanic currents and associated corrosion;
- Observed high potentials resulting from abnormal water distributions and consequent catalyst migration/dissolution; and
- Water distribution and migration during startup/shutdown;

To capture many of these effects, we anticipated that further model improvements and calibration would be required throughout the project.

In developing the mathematical formulation of the multiphase model, a unified approach for porous and non-porous media was employed to capture transport of water and gas species between flow channels and porous GDL, catalyst layer CL, and polymer electrolyte membrane PEM. To incorporate the effect of liquid-gas interfacial drag, water percolation through the GDL, and formation of water drop/slugs/films in the channel due to surface tension effects; the liquid and gas velocities are solved from individual momentum conservation equations. However, a single pressure field is used for both phases. The conservation of mass and momentum equations are based on Ishii's formulation [13], derived by volume averaging the point equations to obtain:

$$\frac{\partial}{\partial t}\left(\varepsilon_k \rho_k\right)+\nabla\cdot\left(\varepsilon_k \rho_k \vec{V}_k\right)=S_k\,, \qquad [7]$$

$$\frac{\partial}{\partial t}\left(\varepsilon_k \rho_k \vec{V}_k\right)+\nabla\cdot\varepsilon_k\left(\rho_k \vec{V}_k\vec{V}_k-\mu_k\nabla\vec{V}_k\right)=-\varepsilon_k\nabla P+\vec{I}_{k,m}+\varepsilon_k\rho_k g\,, \qquad [8]$$

where

$$\varepsilon_k=\alpha_k\varepsilon\,, \qquad [9]$$

$$\vec{I}_{k,m}=-\varepsilon_k\left(\frac{\varepsilon_k\mu_k}{\kappa_k}\vec{V}_k+C_f\left|\vec{V}_k-V_m\right|(\vec{V}_k-V_m)\right). \qquad [10]$$

The fluid phase mass conservation equation accounts for accumulation, convection, and sources due to phase change. The momentum equation terms represent momentum acceleration at a point in space, convection, diffusion through viscous effect, the pressure driving force, drag

forces, and gravity force. Here, the subscripts *k* and *m* denotes the fluid phases, ε is the porosity, α volume fraction, *t* time, ρ density, μ viscosity, *P* pressure, *g* gravity and *I* the drag force from the porous medium and the other fluid phase *m*, κ the permeability and C_f the fluid-fluid drag coefficient. In a non-porous region, $\varepsilon \to 1$ and $\kappa \to \infty$, and the standard Navier-Stokes equation is recovered. The Darcy's law and symmetry drag models are implemented to model solid-fluid and liquid-gas drag, respectively. Capillary forces are modeled by adding a pressure gradient to the liquid phase momentum equation. The capillary pressure was initially based on the Leverett function to compute capillary force from local liquid saturation. The numerical solution approach includes formulation of a partial elimination algorithm to closely couple liquid and gas velocities in all fluid regions where the drag force can be large. The pressure correction equation is formulated from the addition of the liquid and gas mass continuity equations weighted by appropriate factors. The liquid volume fraction, α equation is formulated from the subtraction of the weighted continuity equations.

The energy equation solution assumes equal temperatures for the liquid, gas and porous solid matrix in a given finite volume, but does account for distinct velocities of liquid and gas convecting energy through the model. The conservation equation for energy is given by:

$$\frac{\partial}{\partial t}\left((1-\varepsilon)\rho_S h_S + \varepsilon\rho_{mix} h_{mix}\right) + \nabla\cdot\left(\varepsilon_g \rho_g V_g h_g\right) + \nabla\cdot\left(\varepsilon_l \rho_l V_l h_l\right) = \nabla\cdot\mathbf{q} + \varepsilon_g \boldsymbol{\tau} : \nabla V_g + \varepsilon_l \boldsymbol{\tau} : \nabla V_l + \varepsilon\frac{\partial P}{\partial t} + j_T \eta + \sum R_i G_i + \frac{|\mathbf{i}\bullet\mathbf{i}|}{\sigma} \quad [11]$$

where *h* is the total enthalpy, **q** heat flux from conduction and species diffusion, j_T transfer current between porous solid and fluid mixture, **i** total current density, σ thermal conductivity. The term $\sum R_i G_i$ corresponds to the Gibbs free energy change of reaction, and only contributes for electrochemical reaction steps. The subscripts are *mix* for mixture averaged, *s* solid, *l* liquid and *g* gas. The total enthalpy, *h* includes enthalpy of formation and sensible enthalpy. Therefore, this formulation implicitly accounts for energy sources or sinks due to phase change and chemical reaction. The temperature is computed from the mixture enthalpy using mixture averaged specific heat.

The individual gas species mass conservation equations are as follows:

$$\frac{\partial}{\partial t}(\varepsilon_g \rho_g Y_i) + \nabla\cdot(\varepsilon_g \rho_g V_g Y_i) = \nabla\cdot\left(\rho_g D_i \nabla Y_i\right) + \dot{\omega}_i, \quad [12]$$

where Y_i is the mass-fractions of the *i*-th species, $\dot{\omega}_i$ the source/sink due to electrochemical reaction in the CL, and D_i mass diffusivity. In porous media, an effective mass diffusivity due to water condensation is incorporated by modifying the Bruggeman model as $D_i = D_0\left(\varepsilon(1-\alpha)\right)^{\tau}$, where D_0 is the intrinsic multicomponent diffusivity of species *i* and τ is the tortuosity. Water transport in the polymer electrolyte membrane is modeled using Springer model in which the membrane water transport is determined by electro-osmotic drag and back-diffusion. At the PEM/CL interface the vapor diffusion flux is balanced by water transport into or out of the membrane.

In the porous catalyst regions, electronic current in the solid phase and protonic current in the ionomer phase are both present and constitute the total current. The transfer current density j_T between the solid and fluid arises from the electrochemical reaction on catalyst pore surfaces. Here, j_T is computed using the Butler-Volmer equation. In the absence of deposition the species surface reaction rate is balanced by the species diffusion flux between the bulk fluid and the surface as:

$$\sum_{j=1}^{N_{steps}} M_i (a_{ij}^{"} - a_{ij}^{'}) \frac{j_{T,j}}{F} = \varepsilon_g \rho_g D_i \frac{Y_{i,S} - Y_i}{\delta} \quad . \qquad [13]$$

Here, F is Faraday constant, M_i molecular weight of the i-th species, $a_{ij}^{'}$, $a_{ij}^{"}$ normalized stoichiometric coefficients of reactants and products, $Y_{i,s}$ mass fraction on the catalyst surface, and δ the characteristic length scale for surface to bulk fluid diffusion, typically the pore diameter. The reaction source $\dot{\omega}_i$ in Eq. (6) is calculated by scaling the diffusion flux in Eq. (7) by a surface-to-volume ratio to capture the effect of catalyst loading.

Hardware requirements for the cell scale models are primarily driven by memory requirements, as dictated by the number of finite volume grid cells and the number of intrinsic variables. The operational cell models typically had order 200,000 grid cells and were simulated using Linux workstations with 2.2 GHz CPU speed and 4 GB of RAM memory.

4.4 Model Testing and Validation

4.4.1 Lattice Boltzmann Method

Single Phase Flow Model and Microstructure Generation

The single phase LBM implementation and GDL structure generation were benchmarked against numerous test cases. Initial validation of the single phase model included simulation of the decay of Taylor vortices, which verified correct implementation of the collision function representing the fluid viscosity and periodic boundary conditions for flow. In Figure 43, a test case is shown for flow through an idealized porous structure of solid spheres arranged in a simple cubic array. Permeability κ is computed from the average flow velocity u by applying Darcy's law,

$$u = \frac{\kappa}{\mu\varepsilon}\left(\frac{P_{in} - P_{out}}{L}\right) \qquad [14]$$

where μ is the viscosity, ε the porosity, P_{in} the inlet pressure, P_{out} the outlet pressure, and L the channel length. In Table 1. Non-Dimensional Permeability of a Simple Cubic Arrangement of Spheres, the computed permeability is compared with the analytical solution of Chapman and Higdon [14] at different porosities obtained by varying the sphere size. The values are in agreement within 5% of the analytical solution.

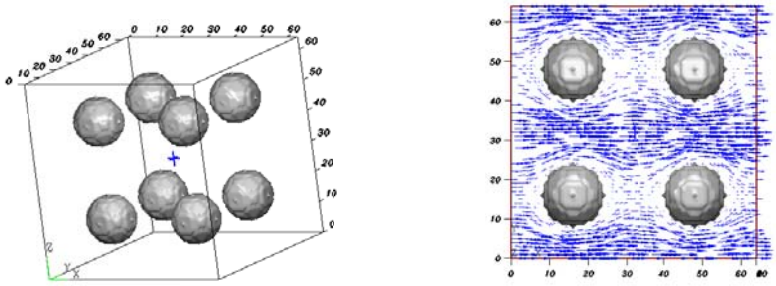

Figure 43. Flow-Through Simple-Cubic Arrangement of Solid Spheres. A Perspective View of the Model Domain, Left, and the Predicted Velocity Vectors, Right.

Table 1. Non-Dimensional Permeability of a Simple Cubic Arrangement of Spheres

Porosity, ε	Analytical, κ/d^2	Computed, κ/d^2	% Error
0.992	0.2805	0.2843	1.3
0.935	0.0761	0.0749	1.6
0.779	0.0192	0.0189	1.6
0.477	0.0025	0.0026	4

The GDL microstructure reconstruction was validated by comparing computed pore size distribution and permeability with measurements. In Figure 44, reconstructed Toray090 is shown with the computed pore size distribution. The peak in the pore volume is at radius 11μm. This is consistent with reported measured value of 12μm. In Table 2, in-plane and through-plane permeability are computed for Toray090 and SGL10BA. GDLs are 200μm thick with spatial resolution of 3.4μm, porosities 0.78 and 0.88, respectively. SGL10BA has higher permeability than Toray090 due to higher porosity. The in-plane permeability is greater than through-plane value. The difference is due to the preferred fiber orientation in the material plane and suggests that alignment to the mean-flow direction have less resistance to the flow. The computed trends are consistent with these observations and are quantitatively similar to those reported in the numerical work of Schulz et al. [12].

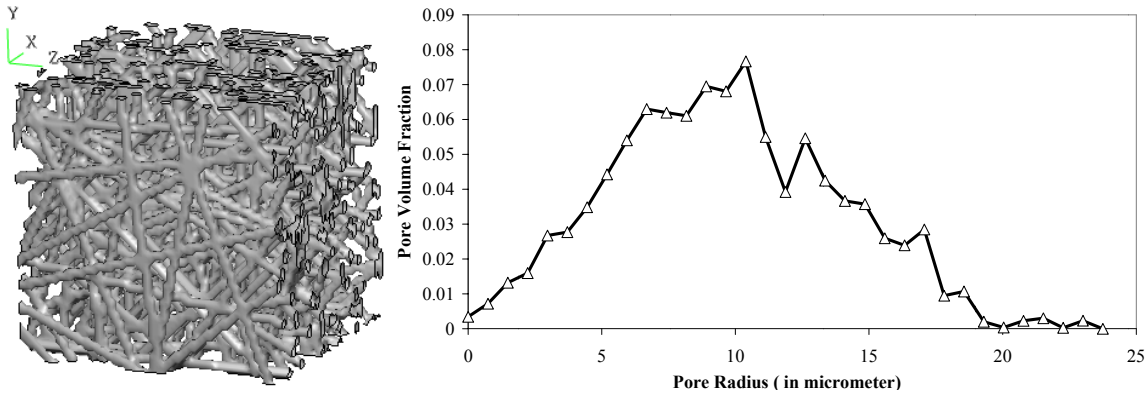

(a) (b)

Figure 44. (a) Numerically Reconstructed Carbon Paper; and (b) Pore Size Distribution; Porosity 0.78

Further validation of the single phase model, and the related microstructure generation approach, was accomplished by prediction of the permeability of compressed GDL structures. A porous microstructure under external compression was modeled following the same approach as by Schulz et al. [12], i.e. by linearly scaling the height of the solid voxels from the base of the material. Therefore, solid voxels further from the base have greater displacement. However, displaced voxels were not allowed to penetrate into each other. The ratio of the compressed GDL thickness and the uncompressed GDL is the compression ratio c.

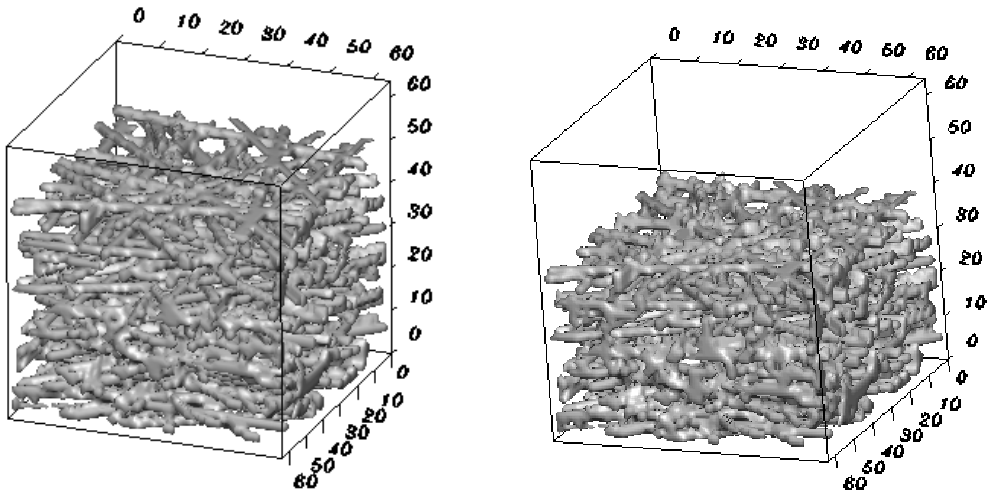

Figure 45. Compressed Toray090 at Compression Ratios 0.8 (Left); and 0.6 (Right)

Figure 45 shows the generated Toray090 microstructure at $c = 0.6$ and 0.8. In Figure 46, the through-plane gas-permeability is compared at different compression ratio for Toray090 and SGL10BA. The measured data is by Dohle et al. on SGL10BA [15]. At higher compression, the GDL thickness decreases, but there is no change in the fiber volume. Therefore, porosity increases and permeability decreases with compression. The computed and measured data are consistent with this expectation.

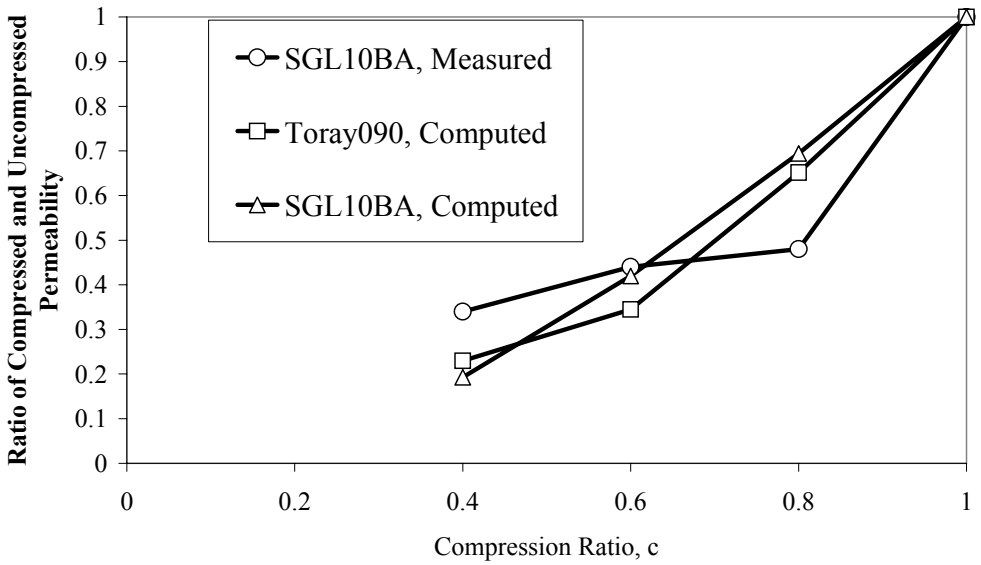

Figure 46. Through-Plane Permeability of Compressed Gas-Diffusion-Layer

To capture the effects of Teflon loading on transport in GDL microstructures, CFDRC developed a Teflon distribution model for the LBM microstructures. This model was based on the assumption that the Teflon solution strongly wets the GDL fibers during the impregnation, consistent with the microscopic images of Teflon 'webbing' at fiber-fiber intersections. To create a microstructure with a specified Teflon loading, spatial distributions of pores of different sizes were identified. The fluid voxels corresponding to the smallest pore sizes were successively filled with Teflon as PTFE % loading increases. Thus, Teflon was preferentially distributed to smaller pores and corners of the larger pores. The increase in fiber diameter due to the Teflon coating was assumed to be negligible, but the fiber surface characteristics were changed from hydrophilic to hydrophobic when any Teflon is introduced. In Figure 47 and Figure 48, laser scan images of GDL surface regions provided by Ballard and the numerically generated microstructures of TGP-H-050 are shown for the range 0-40 % PTFE loading. The model GDL thickness is 170μm, area 102μm × 102μm, and fiber diameter 8 μm. Porosity of the untreated GDL is 0.75.

Figure 47. Laser Scans of GDL Microstructure with varying Teflon Addition; 0%, 20%, and 40% from Left to Right

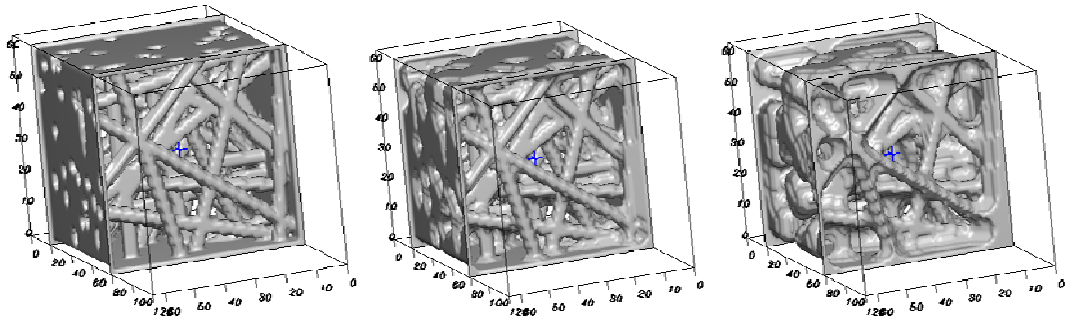

Figure 48. Numerically-Generated GDL Microstructure with varying Teflon Addition; 0%, 20%, and 40% from Left to Right

The single-phase flow permeability predicted by the LBM models is compared to Ballard measurements of permeabilities in Figure 49. The model predictions agree well with the experimental values until high Teflon loadings, beyond the range practical for use in a fuel cell, are reached. These results verified that the stochastic microstructure generation approach is adequate for analysis of transport and PTFE loading effects in carbon paper GDLs.

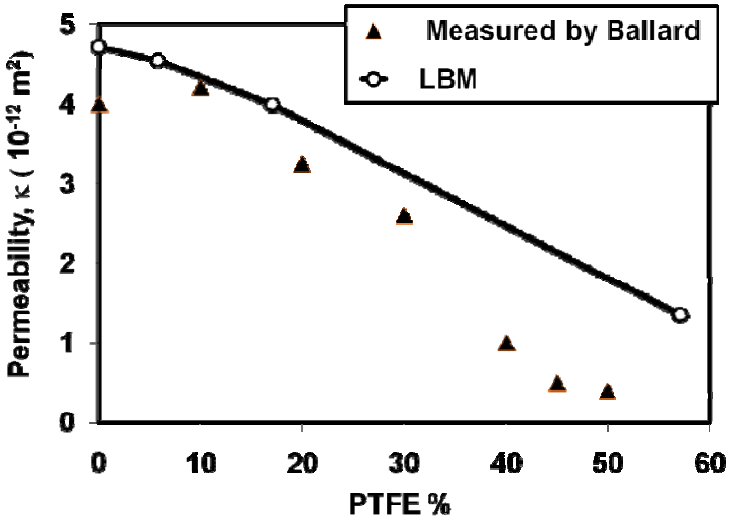

Figure 49. Comparison of Predicted and Measured Toray TGP-50 Permeability Variation with Teflon Loading

These case studies for the LBM approach to simulating flow in porous media, such as GDLs, provided the validation necessary for the project to proceed to development and evaluation of the multi-phase LBM model.

Multi-Phase Flow Model

As in the case of the single-phase LBM model, the initial validation tests for the multi-phase implementation were simple cases evaluating model predictions against analytical solutions. Equilibration of an isolated drop to its spherical shape, and comparison of the predicted surface tension induced pressure difference to the well-known Laplace law, validated the implementation of surface tension forces between the fluids. Droplet equilibration simulations on a solid surface, Figure 50, verified the implementation of variable surface wettability. The predicted shapes of the equilibrated drops on neutral, hydrophilic, and hydrophobic surfaces were cut spheres, as desired.

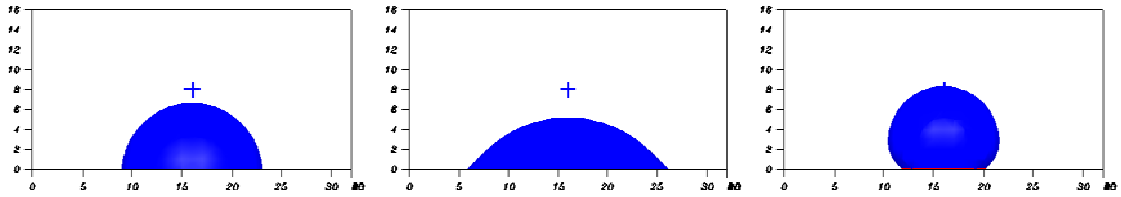

Figure 50. Simulated Drops in Equilibrium on Partially Wetting Surfaces

A qualitative evaluation of the multiphase LBM model was performed by simulations of water permeation into a GDL. The simulations addressed the influence of fiber wettability on the liquid flow pattern. The microstructure was based on Toray 090, 200μm thick comprising of 25 layers of carbon fibers of diameter 8μm, the in-plane area is 218μm×218μm and porosity 0.78. An open space of thickness 109μm is provided at the gas-channel side to allow liquid-breakthrough and formation of multiple droplets. Liquid is introduced at the boundary on the catalyst side. The side-boundaries are no-slip walls of neutral wettability i.e. liquid contact angle 90º. In Figure 8, snap-shots of liquid-breakthrough are shown at different fiber hydrophobicity. Liquid breaks through the channel side of the GDL in the form of droplets. These droplets may coalesce forming larger drops. As hydrophobicity is increased, the predicted liquid saturation at breakthrough decreases. Liquid flows as small streams leading to surface pores. These observations were consistent with published experimental permeation studies [16,4, 5].

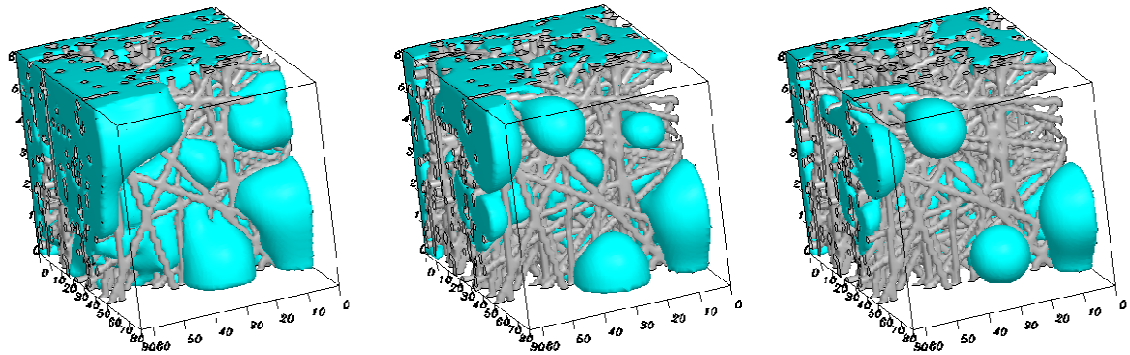

Figure 51. Predicted Distribution of Liquid Emerging from a Toray 090 GDL for Liqiud-Fiber Contact Angles of 90°, 126°, and 162°

Comparison of the predicted pressure versus time history of a similar simulation, Figure 52, to the measured PV curves provided by the University of Victoria, Figure 12 above, demonstrates the principal weakness of the multiphase LBM method. The LBM prediction with surface tension and contact angle effects does not exhibit the sharp drop in pressure at the instant of liquid breakthrough, point (b) of the figures.

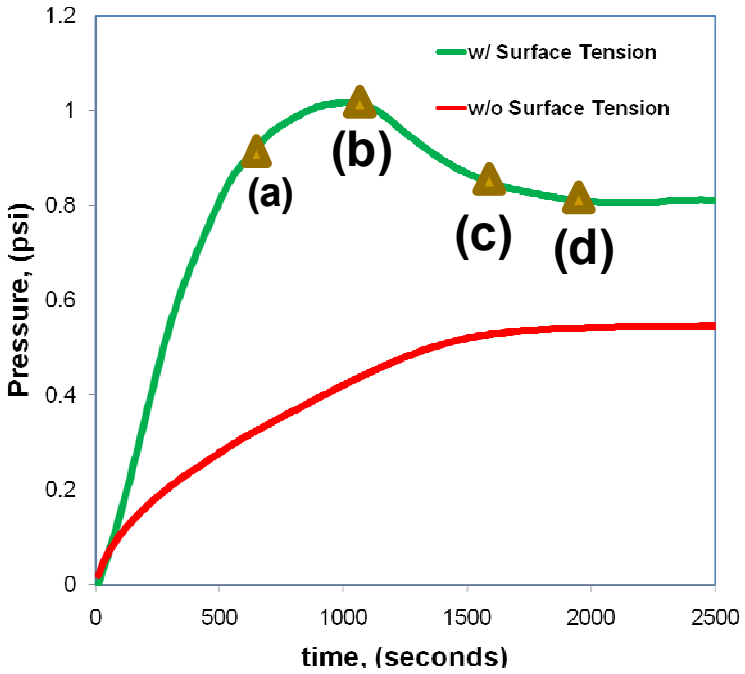

Figure 52. Pressure Transient Predicted by Multiphase LBM during Simulated Water Percolation with and without Surface Tension Effects

This discrepancy occurs because the LBM force functions and time scale are not able to simultaneously reproduce the viscosity, density, and surface tension forces. This was a known potential weakness of the multiphase LBM method, and these results indicate that only static, equilibrium predictions such as the capillary pressure simulations shown in following sections are expected to be quantitatively correct. Therefore, further development of the multiphase LBM models to incorporate heat transfer and multicomponent chemical transport was not pursued.

4.4.2 Cell Scale Multiphysics Model

In the following, validation studies and ongoing model improvements developed through the course of the project are documented.

Initial Two-Phase Flow Benchmark Tests

The initial benchmark model case for measuring accuracy and robustness of the two-phase flow simulations in channels was the predicted phase-fraction profiles obtained by Oliveira et al. [17] for the development of stratification of two fluids with different densities. The model case is developing flow in a two-dimensional channel of width, H, 10 mm and length, L, 100 mm. The fluid densities chosen for the simulation were 1000 kg/m^3 and 950 kg/m^3. The Reynolds number for both fluids was kept at 1000. More details of the test case can be found in [17]. However, in contrast to Oliveira et al., the simulations were run as steady state models that are a greater challenge for stable convergence. The resulting liquid fraction distribution, Figure 53, indicates that the developed flow is stratified as desired. The vertical profiles of the phase fraction alpha, Figure 54, are a good qualitative match to the results of Oliveira, but some quantitative differences do exist, particularly at x/H=2 and x/H = 8.

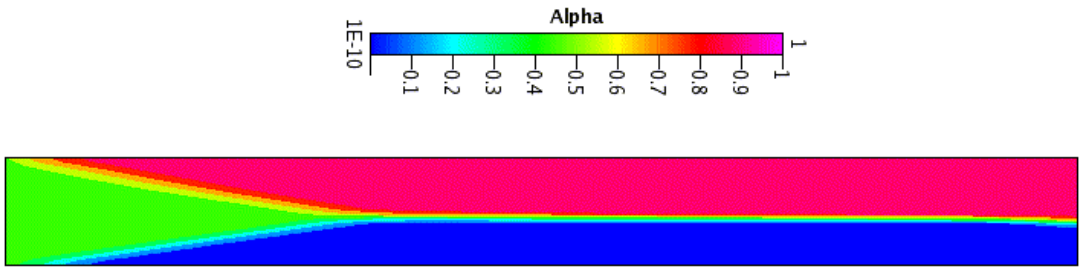

Figure 53. Phase Fraction, Alpha, Contours for Stratification in a 2d Channel Benchmark Case

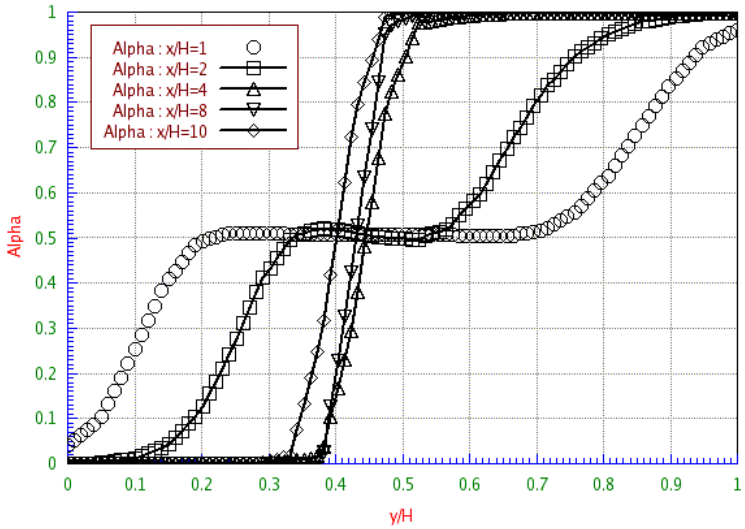

Figure 54. Alpha Profiles at different Stations along the Channel

Additional case studies performed at this stage of model development included prediction of phase separation during flow around a U-bend, and prediction of measured pressure drops in an annular channel under similar conditions to fuel cell operation. For both of these studies, the model performance was deemed satisfactory to continue.

Ballard Straight Channel Two-Phase Pressure Drop

Initial attempts to simulate the two-phase pressure drop data gathered by Ballard exposed several concerns about the two-phase flow formulation. The simulated experiments were for cases in which water was injected through a single hole on the top of the channel, slightly downstream of the air inlet. The drag from the developed air flow past this opening tended to pull all of the water out of the short inlet 'pipe' used in the model, due to the absence of drop scale surface tension forces in the models. Also, the model convergence was determined to be sensitive to the characteristic droplet size and the scaling factors for the phase continuity equations. Adequate convergence for the air and water mass balances were eventually obtained by increasing the length of the water inlet region, refining the solution grid, using a drag model that was symmetric with respect to the identity of the dispersed and continuous phases, including the gravity body force, and scaling the continuity equations by a reference dynamic viscosity for each phase.

The predicted trends for the ratio of 'wet' to dry pressure drops resulting from steady state simulations are shown in Figure 55. At this stage, the models were still not capturing the

significant increase in the two-phase pressure drop at the lower total flow rates, particularly the 61 sccm air flow 11 μl/min liquid flow condition where a strong time dependence was observed in the experimental data. It should be noted that, although the measured pressure drop data for wet flows is clearly time-dependent, see Figure 26 and Figure 27 above, the models were simulated as steady-state problems for this evaluation because of Ballard concerns about long run times for transient models.

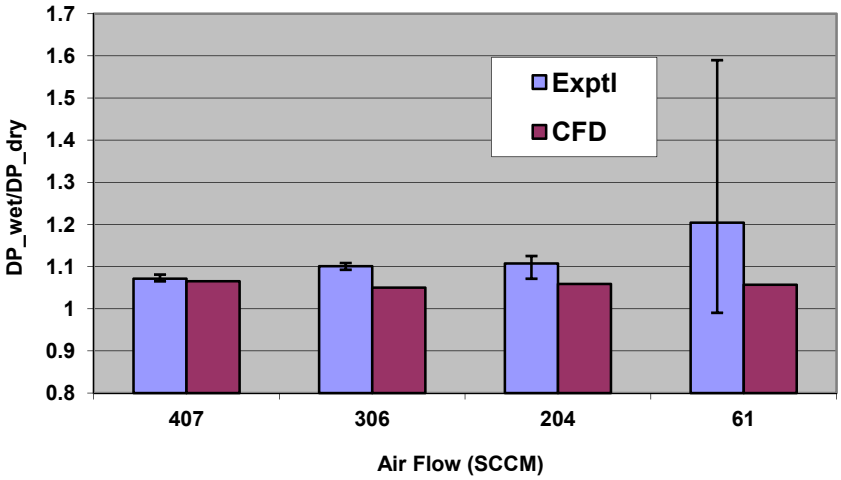

Figure 55. Comparison of Experimental and Simulated Pressure Drop Ratios for Two-Phase and Dry Air Flows with Varying Total Flow, Equivalent Stoichiometry 1.8, Channel Design 1

Better trends in the model predictive capability were observed for variation in liquid flow at fixed air flow rates of 61 sccm, Figure 56, and 407 sccm, Figure 57. The models are able to capture the increase in pressure drop as the liquid flow increases. The model results tend to be lower than the mean measured data at low liquid water flows, likely because the actual problem is transient and effects of periodic liquid water accumulation and draining are not adequately captured by the steady state simulations.

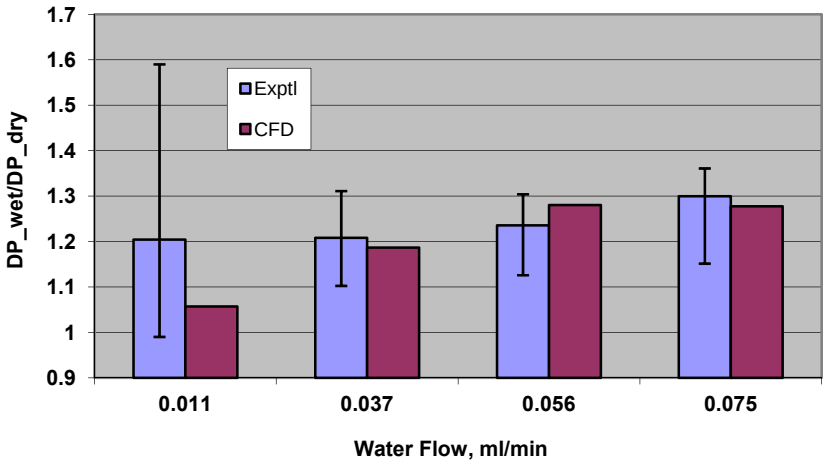

Figure 56. Experimental and Predicted Wet/Dry Pressure Drop Ratios at 61 sccm Air Flow for Varying Water Flow Rates

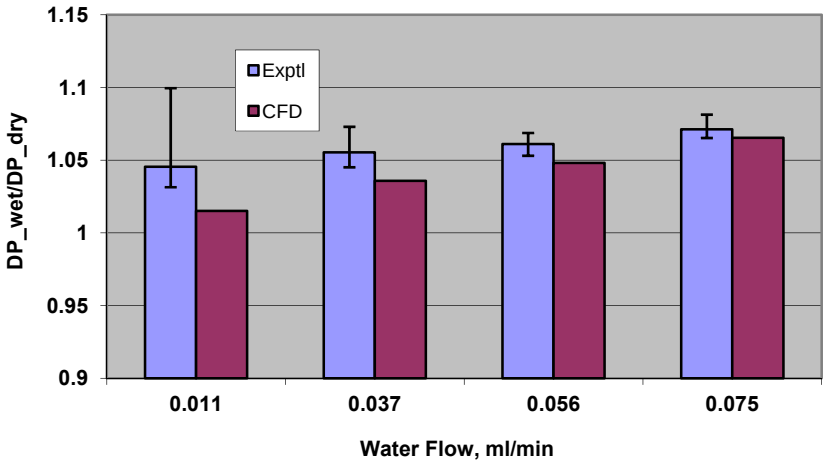

Figure 57. Experimental and Predicted Wet/Dry Pressure Drop Ratios at 407 sccm Air Flow for Varying Water Flow Rates

Application of the models to a second channel design, with wider but shallower grooves, resulted in similar observations as shown in Figure 58. The deviation between measured and predicted pressure drops is still greater for the lower total flow rates, and for this channel design the predictions are significantly worse as the total flow rate is reduced.

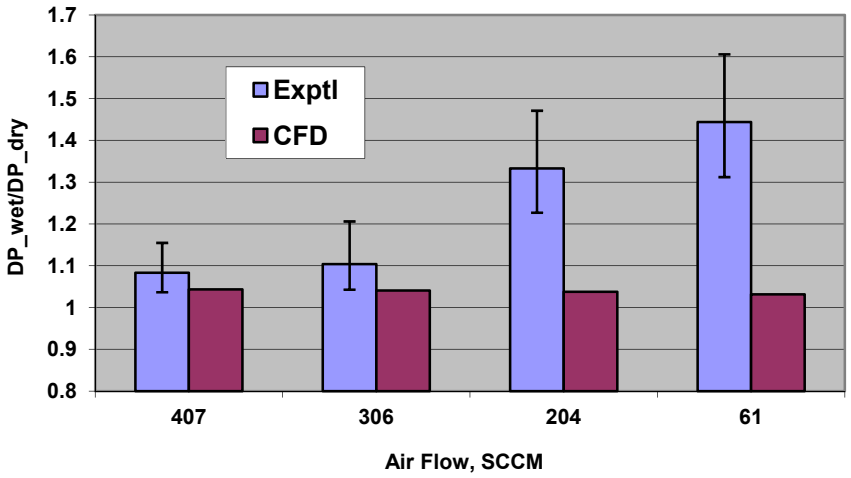

Figure 58. Comparison of Experimental and Simulated Pressure Drop Ratios for Two-Phase and Dry Air Flows with varying Total Flow, Equivalent Stoichiometry 1.8, Channel Design 2

Due to this inadequate model performance, ESI and CFDRC investigated a number of paths to improve the pressure drop results by focusing more on the model formulation. In particular, we evaluated the effects of using densities and kinematic viscosities as the weights for the mass conservation equations, and evaluated approaches to include surface tension effects arising from droplets and thicker films with dimensions similar to the channel cross-section.

U. Victoria Droplet Dynamics

In order to capture the channel scale surface tension effects, ESI implemented and validated a model for predicting the effect of surface tension in the channels. The formulation that was selected and implemented is the Continuum Surface Formulation (CSF) model proposed by Brackbill et al. [18]. In this model, the surface tension effect is modeled as a volumetric body force in the momentum conservation equation. The model implementation passed the basic tests, namely predicting the correct pressure drop across the surface of an equilibrated drop enclosed by the second fluid.

Transient simulations of the droplet emergence and detachment experiments performed at the University of Victoria were used to test the two-phase flow models in fuel cell relevant geometries. These simulations were more numerically stable than simulations of the Ballard experiments, likely due to the relatively small time steps required to resolve the droplet growth. However, the water-interface quickly becomes diffused in these simulations, Figure 59, and a water film is formed instead of the experimentally observed droplet growth. We attempted to improve this capability by improving the coupling of the surface tension forces with the pressure and velocity fields, and by implementing a liquid fraction solution scheme with less numerical diffusion.

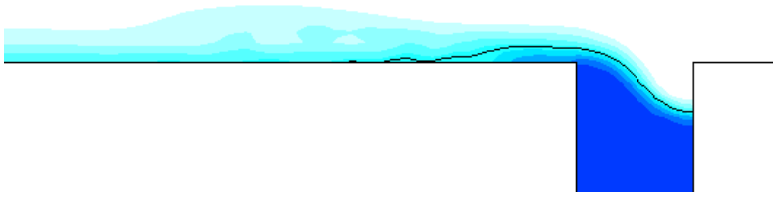

Figure 59. Simulation of Water Injection during U. Victoria Droplet Emergence Studies with Air Velocity 10 m/s, Water Injection Velocity 4 cm/s

Porous Media Forces

The Darcy drag implementation for two-phase flows in porous media was validated by simulating one-dimensional flows through a porous slab, and verifying that the predicted pressure drops matched the analytical solution. The capillary pressure implementation was validated by using a model with a liquid reservoir at the bottom and a fixed pressure 'outlet' to air at atmospheric pressure at the top. The GDL material has a low porosity, low permeability layer separating it from the outlet, to reduce the outflow of liquid water due to the capillary pressure forces. Sample results for volume-averaged liquid fraction in the GDL of approximately 0.5 are shown in Figure 60. Comparison of the model results with the analytical capillary pressure obtained from the Leverett function for the specified GDL porosity, permeability, and mean contact angle of 127° is shown in Figure 61. The results agree quite well, with the model giving slightly higher pressure differences at the greatest saturations due to some of the liquid water entering the low permeability, high capillary pressure force, separator layer. These results provided the confidence necessary to begin testing the models against experiments including water transport through GDLs and two-phase flows in channels.

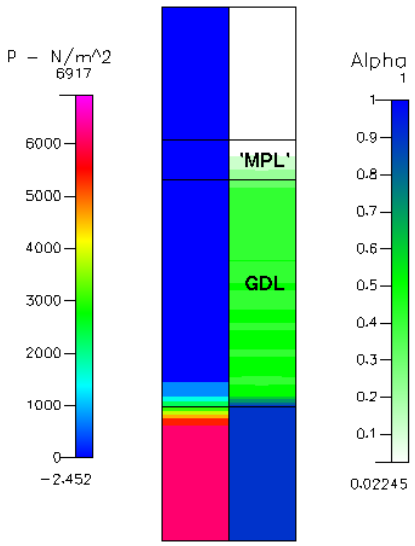

Figure 60. Sample Results of Capillary Pressure Model Validations for Average GDL Saturation 0.5. The Lowest Block is the Liquid Reservoir, Uppermost is Air, and the GDL is Capped by a Thin, Low-Permeability Layer.

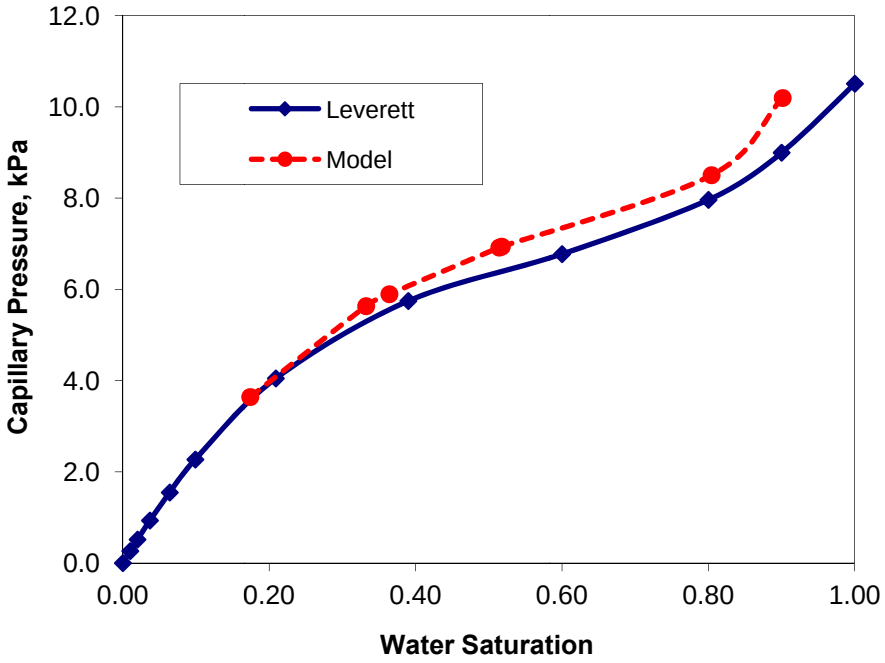

Figure 61. Comparison of Two-Fluid Model Results and Equivalent Leverett Function for GDL Capillary Pressure as a Function of Volume-Averaged GDL Water Saturation

Wet Pressure Drop in Serpentine Channels

The two-fluid model was then evaluated against the Techverse pressure-drop measurements for two-phase flow through serpentine flow channels in contact with GDL. The corresponding experimental data was reported in the June 2009 quarterly report. For the first tests, a short section of the channel that included a bend was simulated. In the simulations, there are three channels each having an air inlet and an outlet. The channels rest on a GDL layer 100 microns

thick. The GDL porosity is 0.8 and permeability 1E-11 m^2. The lower surface of the GDL is the water inlet boundary. The inlet air flow rate is at 1.5 liters/min, and the water flow rate through the lower surface of the GDL is varied.

The two data points simulated are for water flow rates of 0.1 and 0.5 cc/min. The predicted pressure drop increases from 159 Pa to 173 Pa as the water flow rate increases, qualitatively consistent with the Techverse measurements. In Figure 62, liquid volume fraction is plotted at a horizontal section in the channel. At the greater water flow rate there is more water in the channel, as expected. In both cases, the tumbling flow of the air in the turns allows liquid water to accumulate.

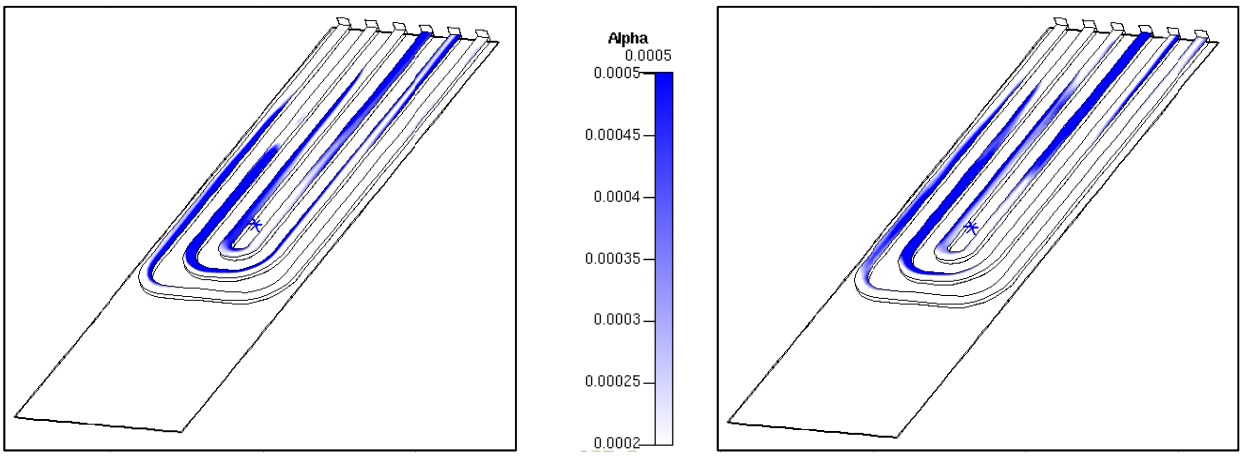

Figure 62. Liquid Water Distributions in the Air Channels for Techverse Experiments at 0.1 ccm/min Water Flow, Left, and 0.5 cc/min Water Flow, Right

Water Crossover in Non-Operational Cell

Ballard provided sample results from testing the effect of oxidant conditions on fuel pressure drop, and of fuel conditions on oxidant pressure. These studies were performed to understand the water transport interactions without electrochemical effects, and utilized well-characterized vapor humidifiers to control the amount of water entering the cells. The pressure drop signature at different liquid water flux, representing different operating cell conditions, is used to characterize the water management characteristics of the unit cell. Even in non-operational cell study, using liquid water injection, considerable interaction between anode and cathode due to liquid water was observed. In the experimental tests reported in January 2009, a 10% increase in the dry air pressure drop was observed as fuel was switched from dry to 100%RH without changing the cathode inlet conditions, suggesting significant water cross-over amongst other possibilities. A typical test result illustrating this is shown in Figure 63.

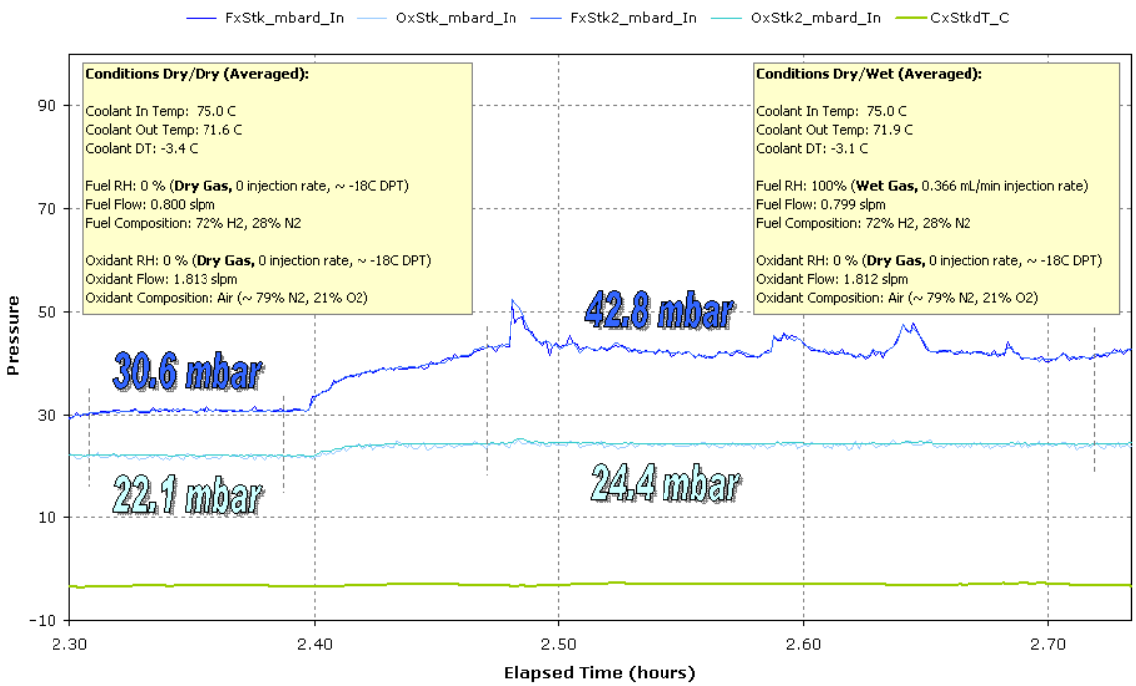

Figure 63. Anode/Cathode Cell Interaction - Non-Operational Water Transport Characterization

This experiment was simulated in order to evaluate the implementation of the Springer membrane transport model and related water transport algorithms such as effective diffusivity in porous media.

The predicted cathode channel pressure drops for the humidified anode case and the dry anode case show the 10% increase observed experimentally, Figure 64, qualitatively validating the model. These results indicated that the coupling to the membrane water transport model was adequate to allow initial testing of the developed models for an operational cell.

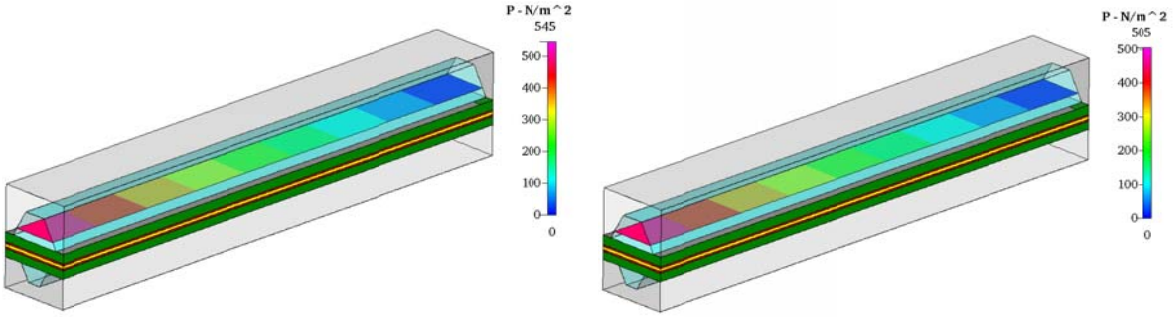

Figure 64. Predicted Cathode Channel Pressure Drops for 100%RH, left, and Dry, right, Anode Inlet Conditions

Operational Cell Model Testing Against Historical Data

At this stage, the integration of the key effects necessary for simulation of an operational cell at typical conditions of temperature, pressure, and inlet states had proceeded far enough to allow initial operational cell testing and validation to begin. The initial results reported here are for the

Ballard MK902 cell. This cell and operating conditions were selected for the detailed diagnostic data and past modeling results available for comparison [19,20]. The simulation utilized two-phase flow in the channels and porous media, electrochemistry, and heat transfer. The coupling between gas phase chemical species transport and liquid water formation was dominated by the treatment of the oxygen reduction reaction. For this reaction, the water product is formed as either vapor or liquid phase water based on the local thermodynamic state. Operating conditions were cathode stoichiometry 1.66, anode stoichiometry 1.5; relative humidities of the inlet streams cathode 84%, anode 41%; cathode oxidant inlet temperature 66 °C, fuel inlet temperature 74 °C; and pressure 3 atmospheres at both channel exits. The resulting liquid water fraction distribution at the level of the cathode GDL for an average current density of 0.85 A/cm^2, Figure 65, shows that liquid water is predominantly under the lands.

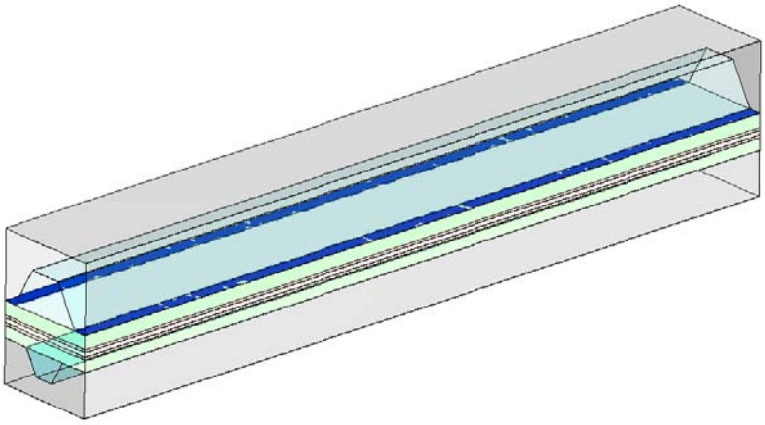

Figure 65. Distribution of Liquid Water Fraction at the Level of the Cathode GDL - Channel Interface for 0.85 A/cm^2 Operation

The predicted current density distribution, Figure 66, shows improved agreement with the experimentally measured trend. There are still stability issues, making it difficult to obtain converged solutions at the target 1 A/cm^2 current density. However, the two-fluid based model does demonstrate improved agreement with the trends along the channel for the current density distribution, particularly near the inlet. The single phase model did include a scalar function for liquid water transport that was coupled to the vapor phase water via evaporation and condensation. That scalar water fraction was convected by the gas phase velocities, diffused in porous media by an approximate treatment of the capillary pressure effects, and was assumed to occupy a negligible volume in the gas phase momentum and mass conservation equations.

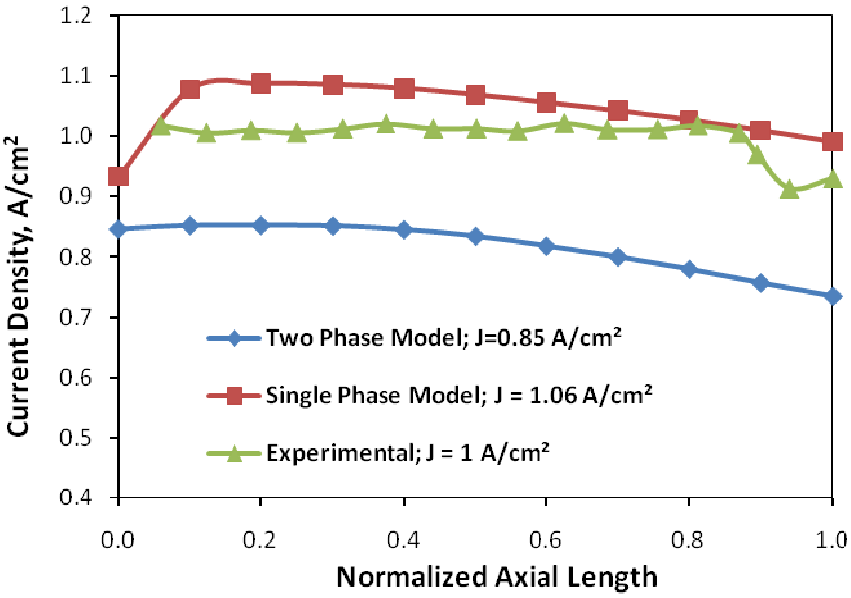

Figure 66. Predicted and Measured Current Density versus Distance along Cathode Channel for Ballard MK902 Cell

During this exercise, CFDRC identified improved treatment of water evaporation and condensation as one of the key needs for further improvement of the numerical convergence and model accuracy. Other issues include improved coupling of the liquid water transport with membrane hydration and verification of the treatment of energy losses, i.e. heat generation, from the electrochemical reactions.

Porous-Channel Interface Condition

At the interfaces between porous (GDLs) and non-porous (flow channels) regions, the finite volume discretization of the above momentum equation naturally results in matching of total momentum flux, and pressure continuity, across the interface. Therefore, there is typically no special treatment of those interfaces. However, the resulting velocity profiles from this simple implementation tend to show spurious over- and under-shoot at the material interfaces. These spurious velocities were observed early in the program for both single-phase and two-phase test cases. CFDRC and ESI initially focused on the pressure correction discretization to address this issue. The pressure correction equation is a discretized form of the continuity, or mass conservation, equation derived from averaging the momentum equation across each finite volume face to determine the relation between mass fluxes and pressure. Concerns about the effect of the porosity jump on the resulting equations always led us to believe that these spurious velocity oscillations were caused by the pressure correction implementation. Improvements to the pressure correction did allow us to remove some of that velocity overshoot and undershoot in simple test cases such as flow in and out of a porous 'plug', while correctly capturing the analytical pressure profile. However, the spurious velocities remained. An initial attempt at reformulating the momentum equation matching condition at the porous-open interface, removing the convection term and imposing stress matching, gave good results for test cases with flow normal to the interface but poor convergence for transverse flows.

Phase Change and Energy Equation Tests

During the initial tests simulating operational cells, we noted that direct formation of liquid water during the oxidation reduction reaction was used to produce liquid water due to the instability of the traditional, liquid-vapor equilibrium driven, phase change models. Additional testing for model systems with known solutions was used to identify the numerical treatment of the energy convection terms for each fluid phase as one source of the instability. The corrected implementation was then successfully validated for constant rate evaporation and condensation of water in a flowing system with adiabatic walls. For this model case, it is known that the total enthalpy of the fluids exiting the system must be equivalent to the total enthalpy entering. The corrected implementation of the heat transfer equation was tested for such a case with a superheated mixture of H_2O vapor, N_2 gas, and liquid water entering at a fixed rate. For constant rates of both evaporation and condensation, the corrected implementation resulted in enthalpy imbalances order 1E-8 Watts/sec between the inlet and outlet, relative to absolute enthalpies entering the system order 1000 Watts/sec.

To address concerns arising from unexpected trends in the predicted temperatures for operating cells, the energy equation formulation and the thermodynamic input data was reviewed. The thermodynamic input data was then adjusted to account for the electron thermochemical properties in the model. The thermodynamic data previously used was based on a literal interpretation of the common electrochemical energy scale derived by Lampinen [21], in which the reference enthalpy and entropy of protons in solution are identically zero. The revised data accounted for the fact that on this scale, the electron reference entropy is non-zero, so that heat generation effects due to electrochemical reaction were corrected. This helped phase change stability, since the cathode was no longer artificially cool.

CFDRC also evaluated physically based approaches for limiting the rate of phase change, either applying heat transfer limits or capping the effective superheat or subcooling allowed in the heat transfer analogue of the mass transfer correlation. All these modifications improved the numerical stability, allowing simulation of higher current density operation and conditions more conducive to liquid water formation, but convergence remained a concern.

Initial Operational Cell Testing Against Ballard In-Situ Diagnostics

The revised version of the integrated code (electrochemistry, heat transfer and phase change) incorporating the improvements in the two-phase flow, heat transfer, and phase change treatments described above was tested in simulations of a three dimensional model of an operational cell. The results reported here are for the Ballard MK902 cell, evaluated against the designed experiments performed by Ballard described in Section 4.2.3 above. This data was selected because of the detailed diagnostic data and past modeling results available for comparison. The simulations utilized two-phase flow in the channels and porous media, electrochemistry, heat transfer and phase change. The base operating conditions were cathode stoichiometry 1.8, anode stoichiometry 1.6; relative humidities of the inlet streams cathode 87%, anode 46%; cathode oxidant inlet temperature 65 °C, fuel inlet temperature 75 °C; and pressure 3 atmospheres in both channels. Initial model input properties were primarily based on historical analysis and fitting at Ballard and CFDRC. The GDL liquid water transport properties included a modified capillary pressure function, Figure 67, extracted from the measurements of Sole [22]. A residual saturation of 0.2 was used to obtain the normalized liquid water saturation.

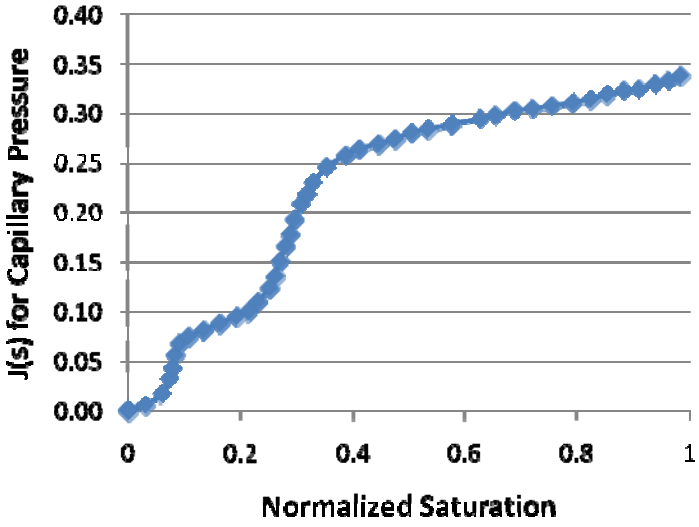

Figure 67. Capillary Pressure Dependence on Normalized Liquid Water Saturation

Comparison of the predicted and measured current density profiles for the base operating conditions and for 10°C cooler operation, expected to result in additional liquid water, is shown in Figure 68. The experimental data has a large constant current density region along the length of the cell, as opposed to the model results, which indicate decreasing current density in the direction of cathode gas flow. The MEA water content profiles, Figure 69, are more uniform with position in the cell, although the prediction is approximately ½ the measured water mass. This water content includes water in the membrane, catalyst layers, and GDLs. For the dimensions and properties of the membrane used in this experiment, λ=14 molecules/sulfonate group corresponds to approximately 2.3 mg/cm^2 and l=22 corresponds to 3.6 mg/cm^2; similarly saturation 0.2 in the GDL corresponds to approximately 3 mg/cm^2. Given the magnitude of the measured water content, we expect that the membrane is almost uniformly equilibrated to λ=14 and the GDL is highly saturated. The model results have a λ profile through the membrane thickness, with an average value approximately 7, and some variation in the saturation but a mean value closer to 0.1 due to evaporation and capillary pressure driving the water out of the GDL. The Springer model thermodynamics used in this case assumed λ=14 for unit activity of water. There are two key issues to note in these results:

- The activity of water cannot be greater than 1 in the model, since the two-phase transport models use the same water vapor pressure curve and include standard vapor-liquid equilibrium driving phase change. In the original Springer model application, water activity was allowed to reach as high as 3.0 as a numerical expediency to avoid dealing with liquid phase water at the membrane surface.
- Also, Ballard has reported that for all model-based analysis of the MEA water data, membrane water content is assumed to be under-predicted by a factor of 2x due to a systematic discrepancy between the Springer model results and measured water content.

Based on these results, we continued to investigate rate models for evaporation/condensation to improve numerical stability during solution of 'wet' models. Implemented the model of Wang and Nguyen [23], which gives lower rates and was more stable.

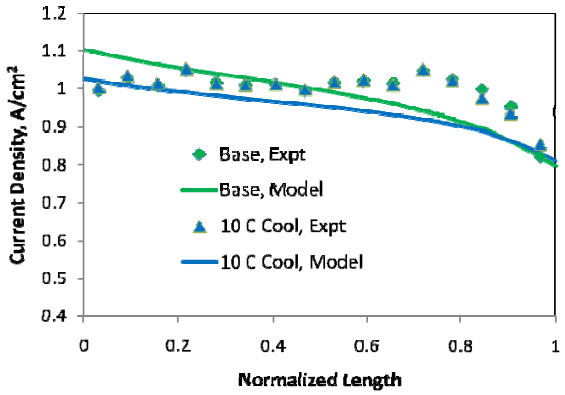

Figure 68. Comparison of Current Density Profiles for Base and 10° C Cooler Operating Conditions at 1 A/cm²

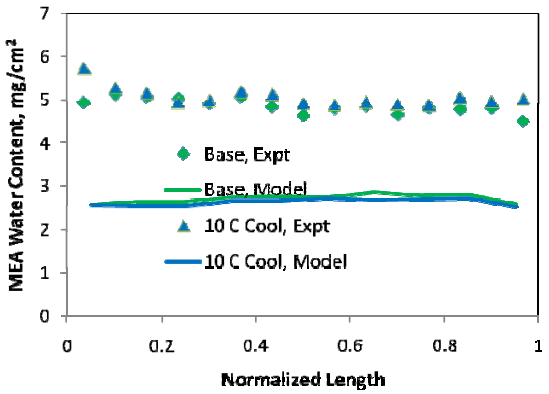

Figure 69. Comparison of Water Content Profiles for Base and 10° C Cooler Operating Conditions at 1 A/cm2

Sensitivity to input parameters related to transport in the GDLs was evaluated by changing the properties to be more consistent with those measured during this program. The GDL permeability was increased from 1 Darcy isotropic to 3 Darcy in the through-plane direction and 12 Darcy in the in-plane direction. The tortuosity was increased from 1 to 4, reducing effective diffusivities by a factor of 3, to better match the measured through-plane values. The model results for these parameters, shown in Figure 70 and Figure 71, exhibited worse agreement with the measured current distribution and similar water content to the previous model. The decrease in current density at the cathode exit for the high tortuosity model was a result of poor oxygen transport into the GDL, and convergence of the model was poorer with the modified properties.

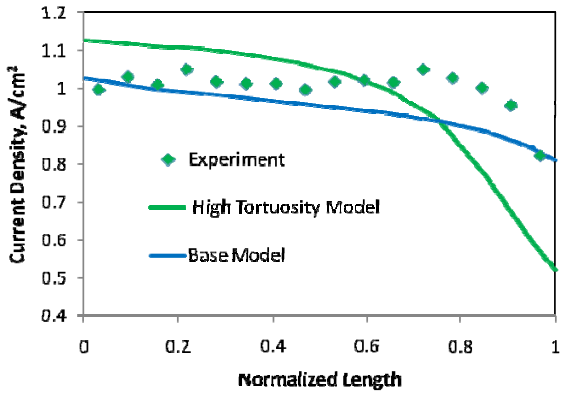

Figure 70. Comparison of Current Density Profiles for Base and High Tortuosity Models for Base Conditions at 1 A/cm²

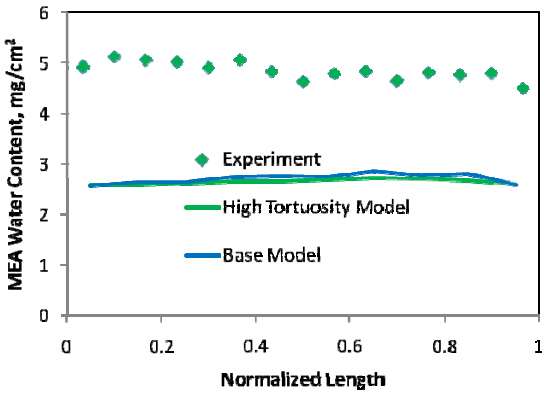

Figure 71. Comparison of Water Content Profiles for Base and and High Tortuosity Models for Base Conditions at 1 A/cm².

The results shown above are from models that exhibited the best convergence and stability observed to date with the developed two-phase transport models and the Springer model active in an operational cell.

Ongoing improvement efforts were deemed necessary to improve the agreement with the measured current density and water content distributions, and to improve numerical stability for adequate testing under a broader range of operating conditions.

Ballard Straight Channel Two-Phase Pressure Drop Gen. 2

Concurrent with the operational cell tests, the revised cell-scale modeling code was tested against the straight-channel two-phase pressure drop data obtained from the Generation 2 apparatus at Ballard.

This study was intended to evaluate the impact of improvements in model setup, grid discretization, and the fluid dynamics algorithms over the fourth year of the program. The model setup was improved by slightly refining the computational grid, improving the grid node distribution for more uniform computational cell aspect ratios and smoother transitions from fine to coarse regions. Model implementation and algorithmic improvements for the energy equation could also affect these results, since the Ideal Gas Law is used for gas phase density and the energy equation solution and convergence affect the gas phase density and fluid dynamics. The model was tested against measured pressure drops in the Ballard Generation 2 experimental fixture, which was more repeatable due to better sealing. The models were tested against data obtained by injecting the liquid water through a GDL, as opposed to the previous point injection, to better evaluate performance in fuel cell conditions. Capillary pressure effects were included, based on the pressure-saturation relation of Figure 67. The models predicted the trends in wet pressure drop with operating conditions, Figure 72, which we were able to capture with earlier models. These models also demonstrated the correct trend for the wet pressure drop response to design variations (lower aspect ratio), Figure 73, unlike the earlier models.

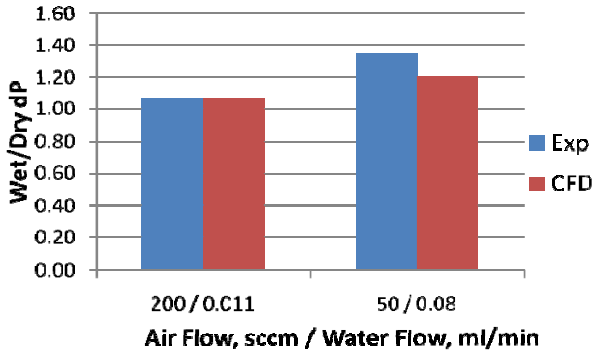

Figure 72. Comparison of Predicted and Measured Two-Phase Pressure Drops in Base Channel Design as a Function of Operating Conditions

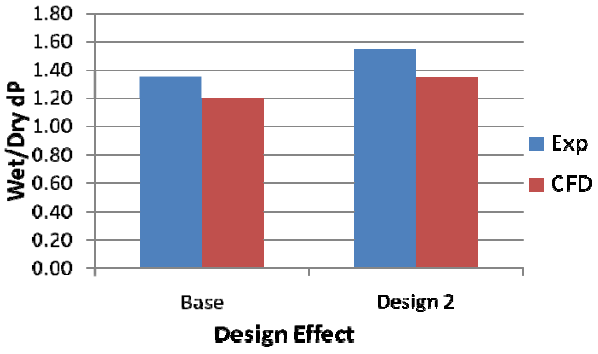

Figure 73. Comparison of Predicted and Measured Two-Phase Pressure Drops at Low Stoich (50 sccm Air/0.08 ml/min Water) Conditions as a Function of Channel Design

These tests provided confidence that the developed models for two-phase flow in both open channels and porous media can be used as an effective design tool. However, it was noted that there were still velocity oscillations at the GDL/channel interface in these models. The imposition of the flow through the GDL likely dampened the impact of these oscillations on the results, but it was considered important to resolve this issue and further improve the numerical stability of evaporation/condensation models before a final evaluation in operational cells.

Porous/Non-Porous Velocity Interface Condition

As noted above, spurious velocity oscillations at interfaces between porous and open regions, i.e. GDLs and channels, were an ongoing concern. Due to the nature of the formulation for the mass conservation equations, the algorithms used to solve for a mass-conserving pressure gradient were expected to be the source of this problem. The original developers of the porous media implementation at CFDRC and ESI contended that no special boundary condition is required at porous-open interfaces, since the porous medium momentum equations revert to the Navier-Stokes equations in the limit $\varepsilon \Rightarrow 1$, $\kappa \Rightarrow \infty$, where ε is the porosity and κ is the permeability. This is not the case, and the lack of a correct boundary treatment was the main cause of spurious oscillations in the interfacial velocity.

Following the work of Beavers and Joseph *(1)*, as described by Betchen et al. *(2)* and by Yu et al. *(3)*, the appropriate boundary conditions at an interface between finite volume cells with differing porosities specifies that a part of the normal stresses is absorbed by the porous solid, not the fluid in the porous media. The previous boundary condition was equivalent to this formulation for continuity of the pressure and the Darcy (superficial) velocity, but the stress matching condition included momentum convection and did not properly scale the shear stress at the interface. The corrected boundary condition was implemented and verified for both single-phase and two-phase flows. Single-phase flow benchmarks demonstrate that the Darcy, or superficial, velocity profiles are correct across the interface. The two-phase flow models give equivalent results if the properties of both fluids are identical, and follow the correct behavior for realistic air and water properties.

The case of channel flow impinging on, passing through, and exiting a porous plug was the first of the benchmark cases examined. The test problem configuration is shown in Figure 74 below.

Figure 74. Schematic of Porous Plug Test Case. Plug Length = 3x Channel Height.

The simulated conditions were a channel Reynolds number 1, porosity 0.7 in the porous plug, and Darcy number (κ/H^2) 10^{-3}. The benchmark results of Betchen and the corresponding CFDRC results are presented in Figure 75. The lower velocity at the inlet, x/H=0, is due to a constant velocity boundary condition instead of fully developed flow. The CFDRC solution quickly reaches a fully developed profile and shows excellent agreement with the benchmark results at the interfaces.

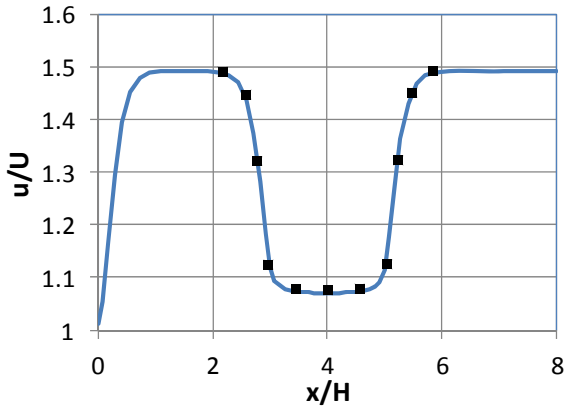

Figure 75. Comparison of Betchen (Symbols) and CFDRC (Curve) Dimensionless Centerline Velocity in Porous Plug Test Case (2)

The benchmark case that is more relevant to fuel cell operation is the Beavers-Joseph problem, with flow in a channel that is segregated into an open and porous region as in Figure 76. The CFDRC implementation of the interfacial boundary condition was also evaluated for this problem and compared to the benchmark results of Betchen. The simulated conditions were a channel Reynolds number 1, porosity 0.7 in the porous plug, and Darcy number (κ/H^2) 10^{-2}. As seen in Figure 77, the improved boundary condition treatment results in excellent agreement for the velocity profile as a function of vertical position in the channel and porous layer, without spurious velocity oscillations. The two-phase results, Figure 78, are again equivalent to the single-phase results after scaling the superficial velocity for the phase fractions.

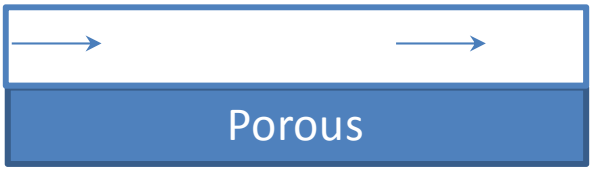

Figure 76. Beavers-Joseph Benchmark Case Schematic

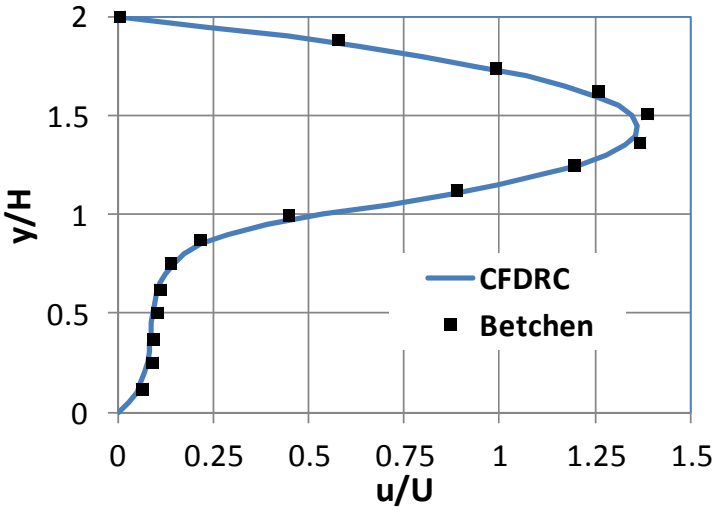

Figure 77. Comparison of Velocity Profile as a Function of Vertical Position for Beavers-Joseph Problem between Benchmark Simulations (Symbols) and CFDRC Results (Curve)

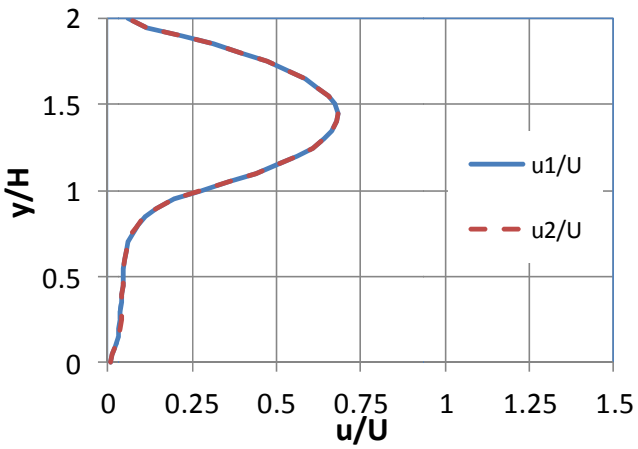

Figure 78. Velocity Profile as a Function of Vertical Position for Two-Phase Beavers-Joseph Problem, Equal Phase Fractions and Fluid Properties

Phase Change Numerical Treatment

Testing in models of short lengths of operational cells demonstrated that the modifications of the porous/open boundary conditions for the momentum equations did provide some improvement to convergence. However, the convergence of the water fraction and liquid phase velocities still tended to stall and the predicted liquid water distribution still exhibited what appears to be numerical noise. An example predicted liquid water distribution in the cathode GDL, Figure 79, demonstrates the nature of a typical result. The concern is the isolated high and low water fraction regions superimposed on the expected distribution; increasing liquid water fraction from the inlet to the outlet and from the regions under the channel center to those under the landings.

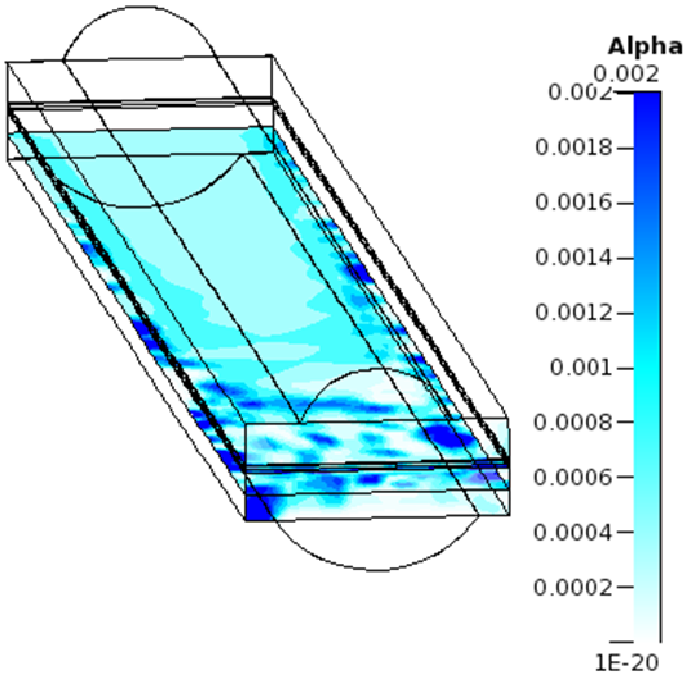

Figure 79. Example Liquid Water Distribution in Cathode GDL for 100% RH Air Inlet Conditions, 60 °C Operation at 0.6 A/cm^2

To address this remaining concern, CFDRC focused on the numerical treatment of the capillary pressure forces and the phase change mass source, the two physical effects identified as contributing to the poor convergence. The capillary pressure force computation was verified, and the treatment of residual saturation was modified to better capture experimental characterization studies. Previously, if a non-zero residual saturation was specified for a material, the capillary pressure force was set to zero whenever the liquid fraction was less than that threshold. The routine was modified to allow the sign of the capillary pressure to change instead, so that the capillary pressure can better drive fluid into a region with a liquid fraction below the residual saturation value. The phase change sources for the liquid volume fraction and the gas phase water vapor mass fraction were previously stored as the mass per unit time of water changing phase in each computational cell. For both models implemented, the rate is calculated from an expression of the form

[15]

where Y_w is the water vapor mass fraction and the *sat* superscript denotes the saturation or equilibrium value at the local temperature and pressure. The routine was modified to also store the partial derivative of this rate with respect to the liquid fraction α and the water mass fraction Y_w, allowing a numerically stable linearization of the source term regardless of whether evaporation or condensation is occurring.

The predicted liquid water distribution in the cathode GDL for an 85% relative humidity cathode feed, Figure 80, has a similar range as the earlier predictions but is qualitatively improved with much less numerical noise. The liquid water is preferentially formed under the landings, and in the downstream portion of the cathode, as expected due to the temperature and water vapor distributions.

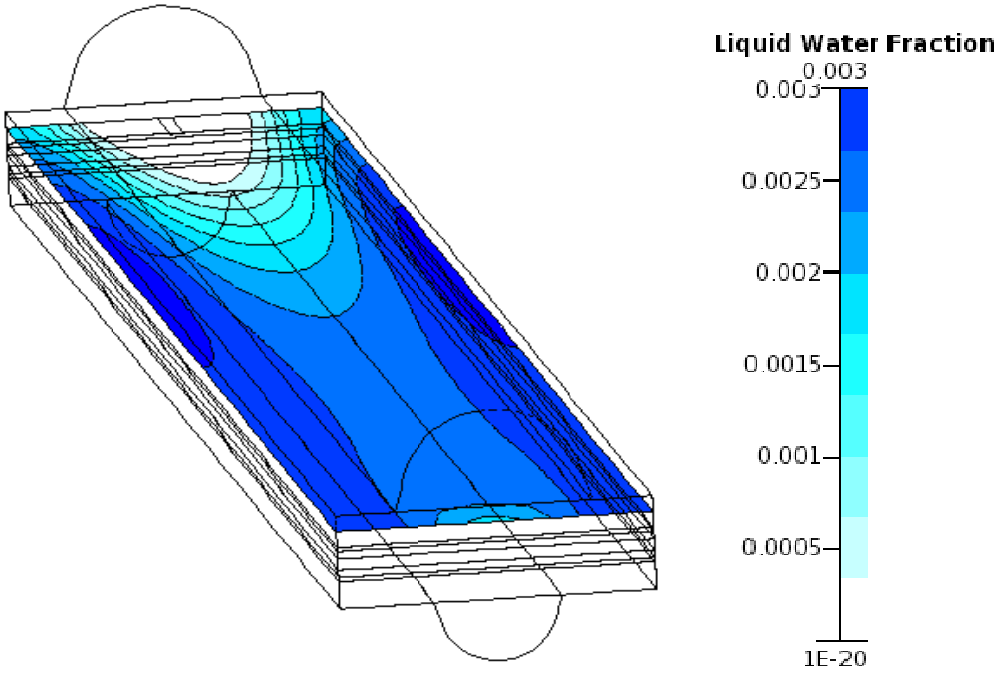

Figure 80. Representative Liquid Water Distribution in Cathode GDL Resulting from Improved Phase Change and Capillary Pressure Functions

Final Operational Cell Testing Against Ballard In-Situ Diagnostics

The final version of the integrated code (electrochemistry, heat transfer and phase change) incorporating the improvements in the two-phase flow and phase change treatments described above was tested in simulations of a three dimensional model of an operational cell. The results reported here are for the Ballard MK902 cell, comparing to the experimental data gathered by Ballard during this project. The base operating conditions were cathode stoichiometry 1.8, anode stoichiometry 1.6; relative humidities of the inlet streams cathode 87%, anode 46%; cathode oxidant inlet temperature 65 °C, fuel inlet temperature 75 °C; and pressure 3 atmospheres in both channels. Initial model input properties were based on the characterization performed during this work and the historical parameters provided by Ballard. The principal difference from the previous model evaluation simulations was the change in the GDL permeability to anisotropic values of 3 and 12 Darcy in the through- and in-plane directions, respectively.

Comparisons of the predicted and measured current density and MEA water profiles for the base operating conditions, reduced inlet humidity, low current, and for 10°C cooler operation are shown Figure 81 through Figure 88. The origin of the normalized length coordinate is at the cathode inlet and anode exit, with the cell operating in counter-flow. The current density and liquid water trends agree well along the length of the cell, from cathode inlet to cathode outlet/anode inlet, for the base operating conditions. The models were simulated at the measured cell potential, using cathode kinetics extracted by Ballard from a short cell with negligible reactant depletion, and the current was under-predicted by 20% for all 1 A/cm^2 cases. For the low current conditions, the experimental data indicates that the membrane is drying near the cathode inlet while the model agrees well over the remainder of the cell. It should be noted that the air enters at 100% relative humidity according to the provided experimental data, while the fuel inlet dew point is only 5°C below its inlet temperature and the cell is nearly isothermal, so that uniform membrane hydration or slight drying at the cathode exit, normalized length 1, should be expected.

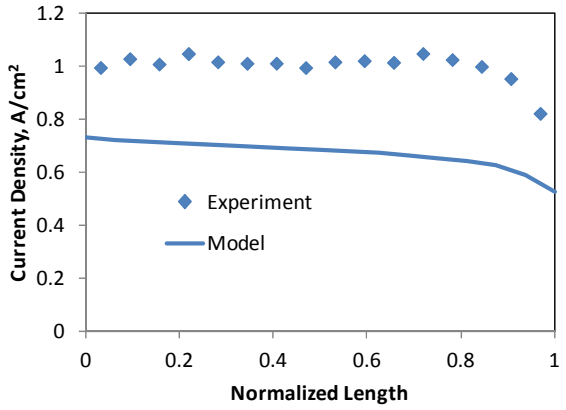

Figure 81. Comparison of Experimental and Predicted Current Density Profiles for Base Operating Conditions

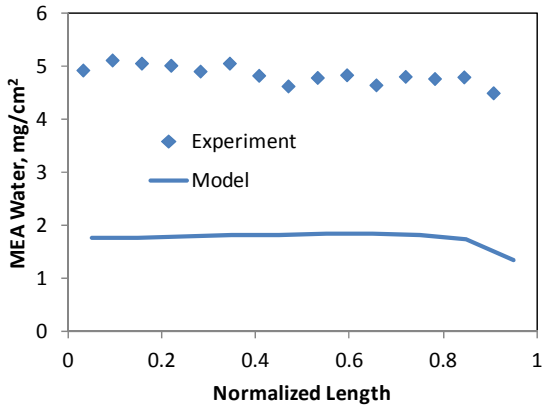

Figure 82. Comparison of Experimental and Predicted Water Content Profiles for Base Operating Conditions

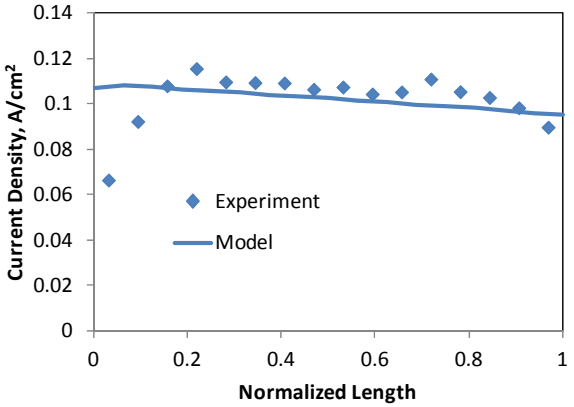

Figure 83. Comparison of Experimental and Predicted Current Density Profiles for Low Current, 0.1 A/cm^2, Operating Conditions

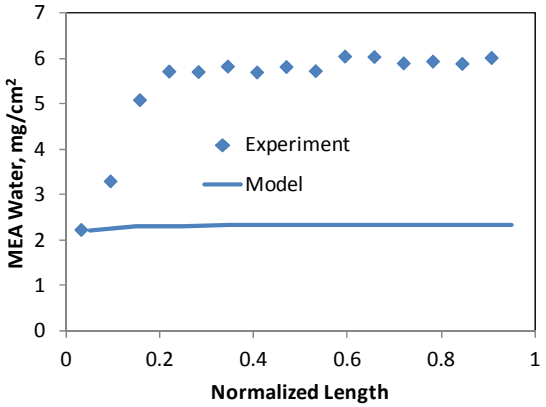

Figure 84. Comparison of Experimental and Predicted Water Content Profiles for Low Current, 0.1 A/cm^2, Operating Conditions

The low humidity trends are similar to above, with the model not reproducing the apparent slight drying of the membrane at the cathode inlet and capturing the reduced water content and current densities at the cathode exit. Under reduced temperature operation, the model does not capture the reduced current density at the cathode exit that is likely due to liquid water formation causing mass transfer resistance. The predicted liquid water distribution is very flat, as expected and qualitatively consistent with the measurements.

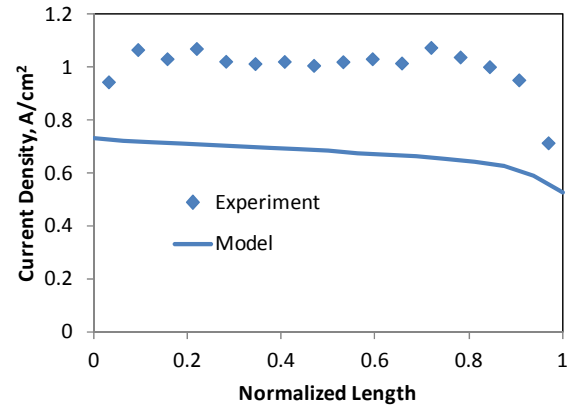

Figure 85. Comparison of Experimental and Predicted Current Density Profiles for Low Inlet Humidity, 25% Ox 16% Fuel, Conditions

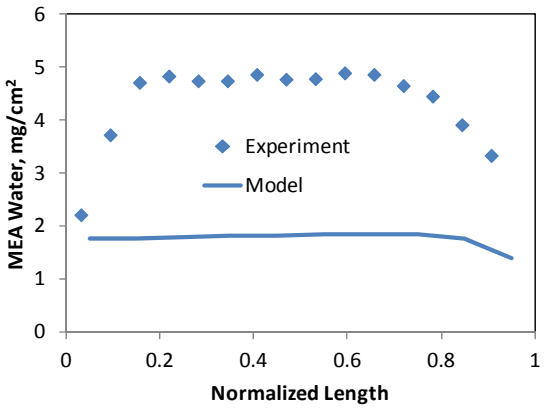

Figure 86. Comparison of Experimental and Predicted Water Content Profiles for Low Inlet Humidity, 25% Ox 16% Fuel, Conditions

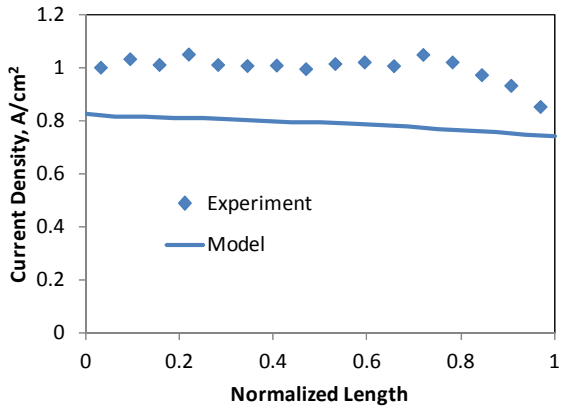

Figure 87. Comparison of Experimental and Predicted Current Density Profiles for Low Temperature, 10°C Cooler, Conditions

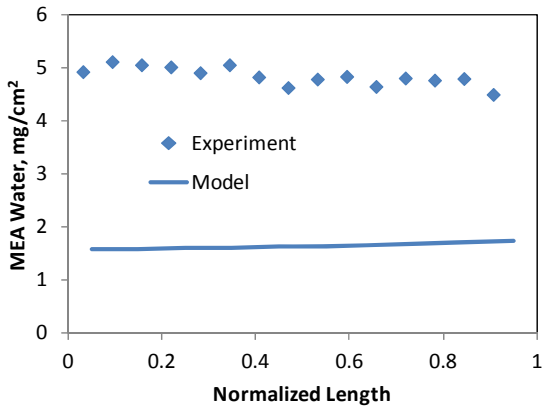

Figure 88. Comparison of Experimental and Predicted Water Content Profiles for Low Temperature, 10°C Cooler, Conditions

Quantitatively, the model is under-predicting the magnitude of the current density for all high current cases by 20%. This is due to diffusion limitations from the channel to the catalyst layer, which are arising because of the low effective diffusivities used in the GDL and not because of liquid water blocking oxygen diffusion. As in the previous study, the MEA water content is underpredicted by approximately a factor of 2.5 for all cases although the spatial trends are improved. This occurs because the GDL and catalyst layer water is underpredicted by a factor of 100, as the models are still unable to retain liquid water at the residual saturation value of 0.2. The water volume fraction in the GDL is order 10^{-2} for all cases shown, at least an order of magnitude too low to reproduce the measured MEA water contents if a water-equilibrated membrane corresponds to 3.6 mg/cm^2 measured water as expected.

This final testing and validation study confirms that there are still remaining issues for the fuel cell scale multiphysics models. The predicted liquid water saturation in the porous GDLs and catalyst layers is still much too low, likely because of the nature of the models used to capture non-zero residual saturation. This formulation of the Darcy's law drag term, with the relative permeability in the denominator, requires imposing an infinite force on the liquid water to keep it stationary due to the drag force term. The capillary pressure function is not adequate to keep the liquid water stationary, and with a non-zero relative permeability the liquid water eventually leaves the GDL. The alternate, capillary diffusion form of the combined water momentum and mass conservation terms multiplies the relative permeability and the capillary pressure force, so that the capillary diffusivity can be forced to zero and the water can remain stationary in the GDL if the volume fraction is below the residual saturation.

4.5 Model Application Studies

Application studies of the microscale LBM and cell-scale multiphysics models described above are discussed in the following sections.

4.5.1 Lattice Boltzmann Method

Water Distribution Simulation

One application of the multiphase LBM was simulation of the equilibrium water distribution inside a partially wetted GDL microstructure. Figure 89 shows the Toray-050 microstructure and the predicted water distribution. The GDL is 170μm thick, cross-sectional area is 200 μm ×200 μm, porosity 0.75, contact angle 144º. The grid resolution is 3.4μm. The inlet boundary is a no-slip wall. The space between the GDL and inlet is 70μm thick, initially filled with liquid corresponding to liquid saturation of $\alpha = 1$. The outlet is an open boundary at standard atmospheric pressure. The space between GDL and the outlet is 70μm thick, initially filled with gas corresponding to liquid saturation of $\alpha = 0$.

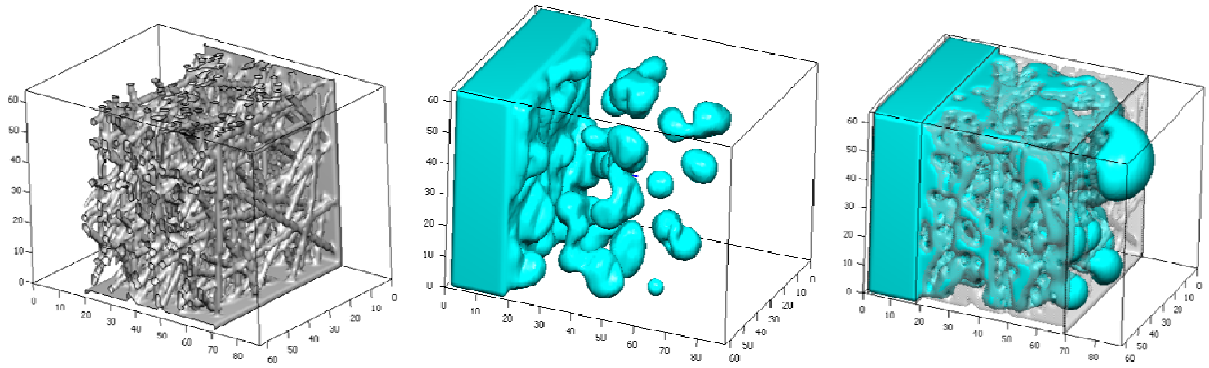

Figure 89. Toray-050 Microstructure and Predicted Water Distribution inside the Wet GDL for Liquid Fraction 0.3 and 0.7

Initially, the GDL is filled with a uniform saturation $0 < \alpha < 1$. As the time progresses phase separation sets in. In the figure liquid distribution is shown without showing the fibers for clarity. At low saturation ($\alpha = 0.3$) globules of droplets are formed that are distributed throughout the GDL. Most of the droplets are separated from each other. At higher liquid saturation ($\alpha = 0.4$), the droplets coalesce and form interconnected liquid streams. Part of the liquid also remains as isolated droplets. At still higher liquid saturation ($\alpha = 0.7$) liquid emerges through multiple openings at the GDL surface. Interconnected liquid paths are visible from inlet to these openings.

Capillary Pressure Simulation

To obtain a capillary pressure saturation curve, a hydrophobic medium of porosity 0.5 is positioned at the GDL outlet. The pores are 3.4μm in diameter and uniformly distributed. The layer prevents liquid to escape through it, but the gas can flow. The resulting equilibrium liquid distribution in the presence of the hydrophobic layer is shown in Figure 90 at $\alpha = 0.7$. Compared to Figure 89, there is no emerging droplet from the GDL surface. The pressure-saturation (P_c - α) plot is shown in Figure 91. The corresponding prediction using the Leveret function is plotted for comparison, based on the values for surface tension water $\sigma = 0.072$ N/m and Toray-050 permeability 4 Darcy, i.e. 4×10^{-12} m^2. Although the Leverett function is not calibrated for GDL materials, the comparison does indicate that the magnitude and trend with water fraction of the LBM prediction is reasonable.

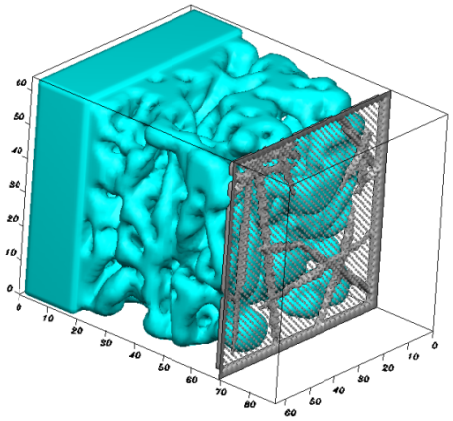

Figure 90. Water Distribution during Capillary Pressure Measurement Simulation, Water Volume Fraction α = 0.7, showing the Hydrophobic Plug at GDL Exit

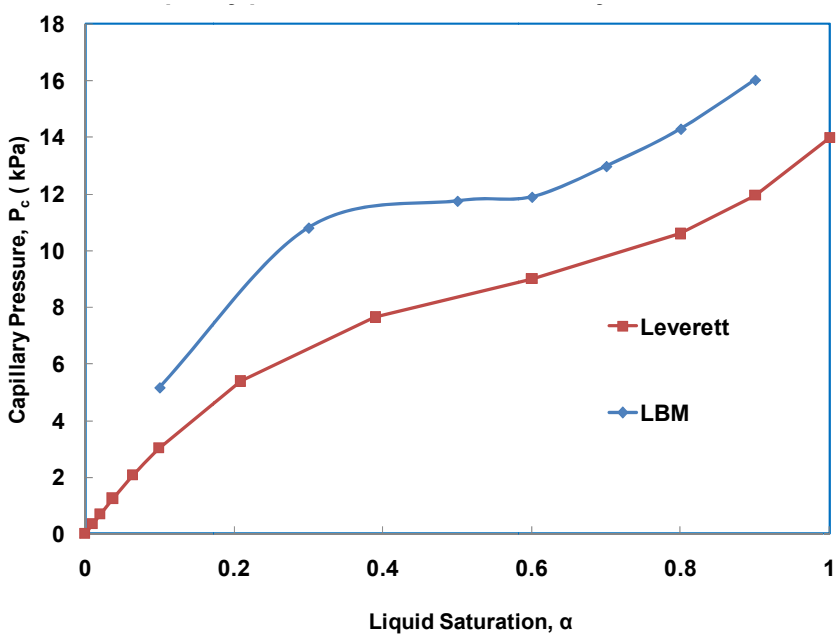

Figure 91. Comparison of Predicted Capillary Pressure Dependence on Water Saturation and the Leverett Function Correlation

These simulations provided valuable insight into physically reasonable capillary pressure distributions inside porous GDL materials, and were used to guide details of the capillary pressure implementation in the cell-scale two-phase model.

4.5.2 Cell Scale Multiphysics Model

Wet Flow Distribution

Unit cell two phase flow validation using a 21 channel oxidant cell design was attempted by Ballard early in the project. The objective of this work was to evaluate the predicted wet flow sharing and water management characteristics against previously obtained experimental data. However these modes did not converge well, likely due to inadequate grid resolution. CFDRC performed model studies using 4 channels for faster turnaround with adequate resolution. The

model domain is shown schematically in Figure 92. Convergence was not an issue for these simulations, after modification of the inlet boundary condition to introduce the two-phase flow as a mixture with the desired average liquid fraction. In these simulations, Figure 93, the wet flow sharing trends (without GDLs) showed reduced air flow in channels that are getting more liquid water in line with Ballard expectations for the behavior. These simulations provide a very first wet flow sharing analysis capability and are valuable in optimizing water management at the unit cell level.

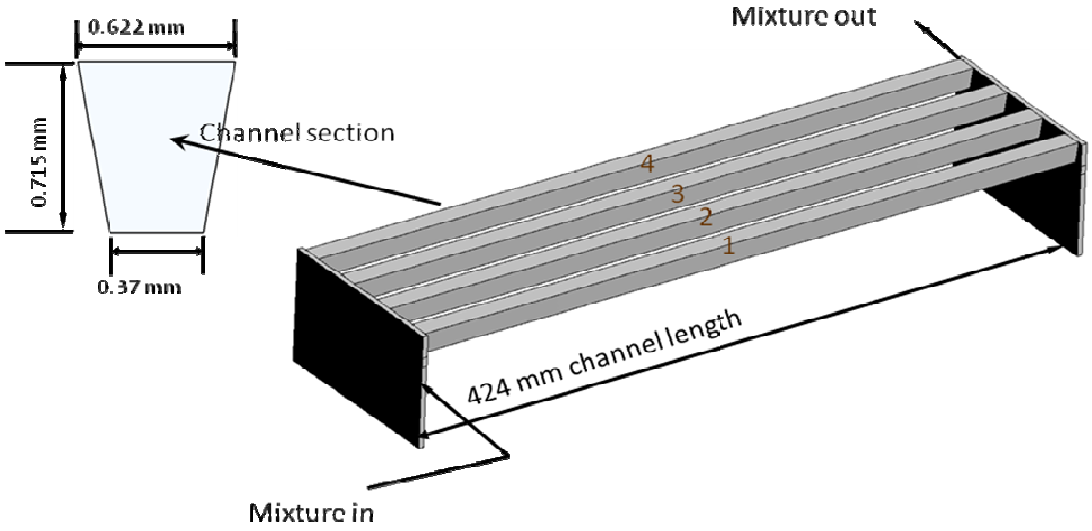

Figure 92. Schematic of Model Domain for Four-Channel Section of Ballard Oxidant Cell

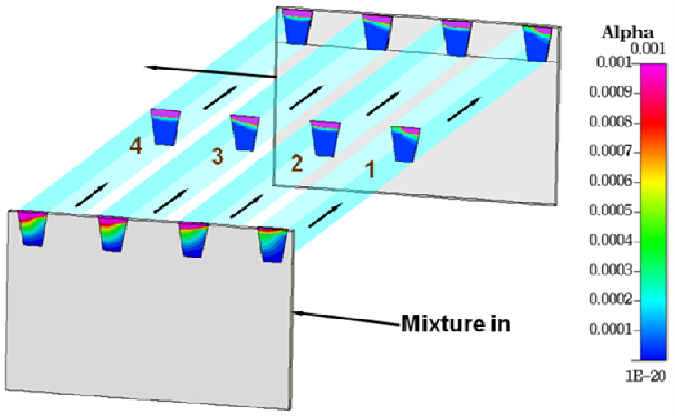

Channel	Air Mass Flow Rate, kg/sec	Water Mass Flow Rate, kg/sec
1	1.10E-05	1.04E-06
2	1.08E-05	1.89E-06
3	1.07E-05	2.53E-06
4	1.06E-05	3.05E-06

Figure 93. Two-Phase Flow Predictions of Water Fraction (Alpha) and Mass Flow Distributions in Reduced Model of Ballard Oxidant Cell

Ballard Flow Maldistribution

Ballard continued stack studies investigating flow mal-distribution among 28 channel stack sections. These simulations were judged by Ballard to be valuable for identifying the extent of stoichiometry reduction and flow mal-distribution in any single channel resulting from a given water volume within the channels. A 20x improvement in channel-to-channel air flow uniformity was predicted for a 'wet' case after doubling the air stoichiometry and total flow rate.

Ballard Kinetics Extraction

Concurrent with the operational cell diagnostic experiments, Ballard provided performance and water management characterization data for a next-generation cell. During this period, Ballard also conducted a series of experiments to characterize the Membrane Electrode Assembly (MEA) used in those cells. The experiments are performed in a small test cell designed to have minimal resistance losses outside the MEA, and operated under high stoichiometry conditions to reduce the effects of reactant depletion on the measured performance. The data is then fit using a Ballard 2-D through-plane + 1-D in channels model as described in [24]. This model assumes Tafel kinetics for the oxygen reduction reaction, and only treats the cathode side transport and electrical effects in detail. The anode side overpotential and ohmic losses are captured in an empirical MEA resistance parameter, which also includes ohmic losses in the membrane.

CFDRC and Ballard developed a systematic approach to enable application of the kinetics and cell resistance parameters derived from these experiments. In this approach, the oxidation kinetics are simulated with the parameters derived from the Ballard characterization and fitting. A detailed simulation of the test cell, including the full physics for both the cathode and anode sides, is used to calibrate a sub-model for the membrane electrical properties to enable prediction of the MEA performance in other cell designs. Calibration is necessary since the full cell model includes losses not present in the Ballard compact model, such as increased effective resistance of the GDLs and membrane due to current crowding in the through-plane direction. The calibration procedure has been automated.

Examples of the detailed model results after mapping the Ballard MEA characteristics are shown below for operation at 60 °C and 100% relative humidity. A section of the model geometry, Figure 94, depicts the MEA components included in the model.

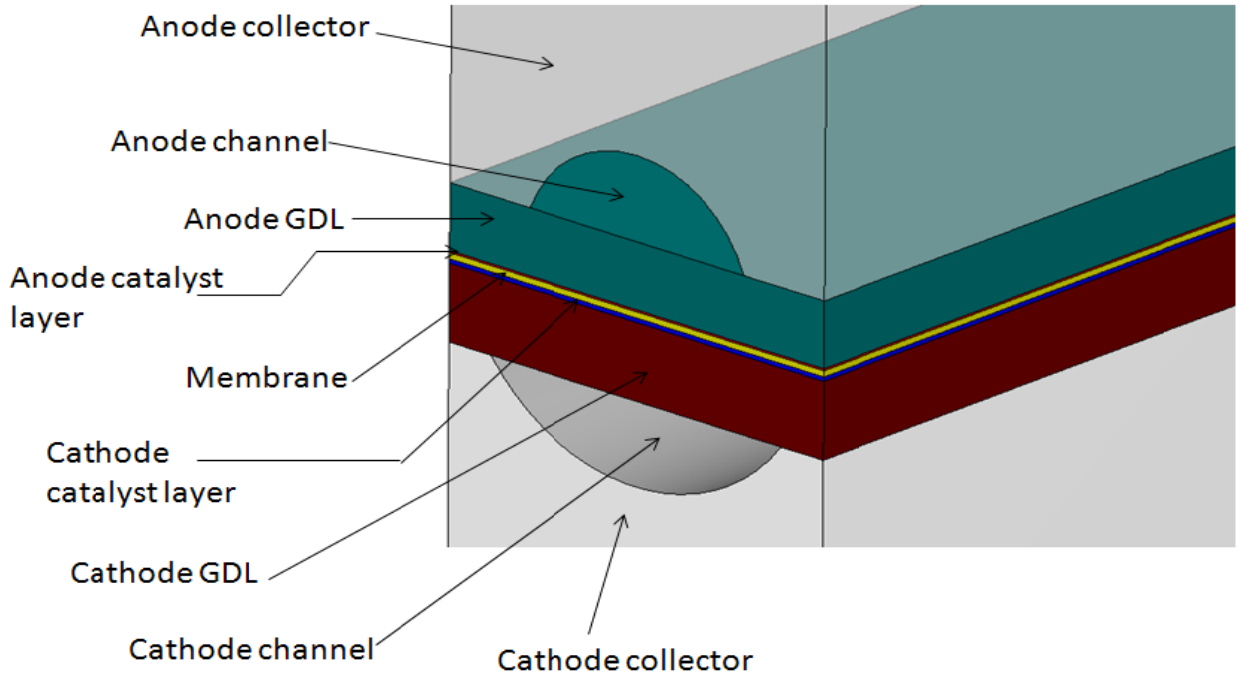

Figure 94. Schematic of the Test Cell Model, Depicting the Channel Orientation and MEA

After the calibration of the membrane resistivity model to match the characterization at a single point in the linear region of the polarization curve, the entire range of cell voltages was simulated to evaluate the detailed model. An initial evaluation of this calibration procedure was performed using single-phase (gas phase only) flow to analyze the characterization cell performance during 60 °C operation with a 100% relative humidity cathode feed. A second analysis, utilizing the developed two-phase flow models for liquid water transport, does reduce the cell performance and bring the predicted polarization curve closer to the experimental values, Figure 95. The extension of the linear region of the predicted polarization curve to cell voltage approximately 0.5 V can be ascribed to a number of factors, including calibrating model parameters to the fit of another model. However, the main concern we have is that the volume fraction of liquid water retained in the cathode GDL is not sufficient to cause mass transport limited performance at a current density of 0.6 A/cm^2.

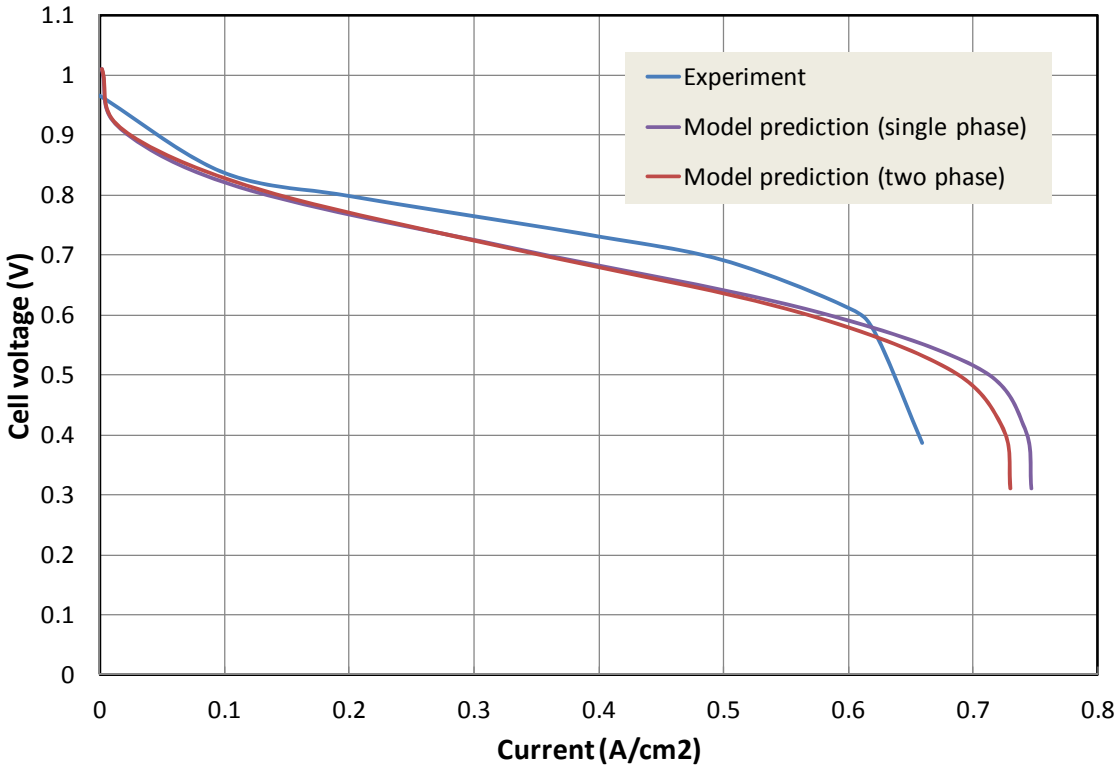

Figure 95. Comparison of Experimental Polarization Curve and Detailed Model Prediction at 60°C, 100% Relative Humidity Operation

4.6 Design and Operational Improvements

4.6.1 Oriented GDL Fibers

This potential improvement to materials design was devised and evaluated computationally using the single-phase LBM model. In the computations, the GDL is constructed by randomly oriented fibers lying in parallel planes. The through-plane direction is along the *x* axis, and *y, z* are the in-plane directions. We investigate the orientation effects by constraining the fibers along a preferred direction. Figure 96 shows fiber arrangements when their inclination to the *z* axis is

limited to φ values of 5, 15, 30, 45 and 90 degree. Within this limit the fibers are assumed to orient randomly. The porosity ε is set to 0.78, which is characteristic of an uncompressed Toray090. The grid resolution is at $64 \times 64 \times 64$. In Figure 97, the predicted through- (*th*) and in-plane (*in*) permeabilities are plotted. These results show that the through-plane permeability, κ_{th}, decreases with decreasing φ, however, the change is rather small. As example, κ_{th} at ϕ =5 and 90 are within 15%. The effect is more pronounced in the in-plane direction. Here, $\kappa_{in,z}$ increases by about 75% and $\kappa_{in,y}$ decreases by 47% as ϕ is lowered from 90 to 5. The results suggest that the in-plane permeability can be increased significantly along a preferred direction by orienting the fibers along it, without resulting in significant drop of through-plane permeability. This information can be used to enhance gas-diffusion in GDL. The GDL-material can be constructed in two layers. The gas-channel side consisting of fibers with preferred orientations assisting in-plane gas flow between neighboring gas-channels, whereas the catalyst side having fibers randomly oriented thereby allowing uniform distribution of incoming gas on the reaction sites. Experimental evaluation of similar work, with experimental data supporting the potential promise, was shown at the 217th ECS meeting by Jonquille and Pauchet, ECS meeting abstract MA2010-01 172.

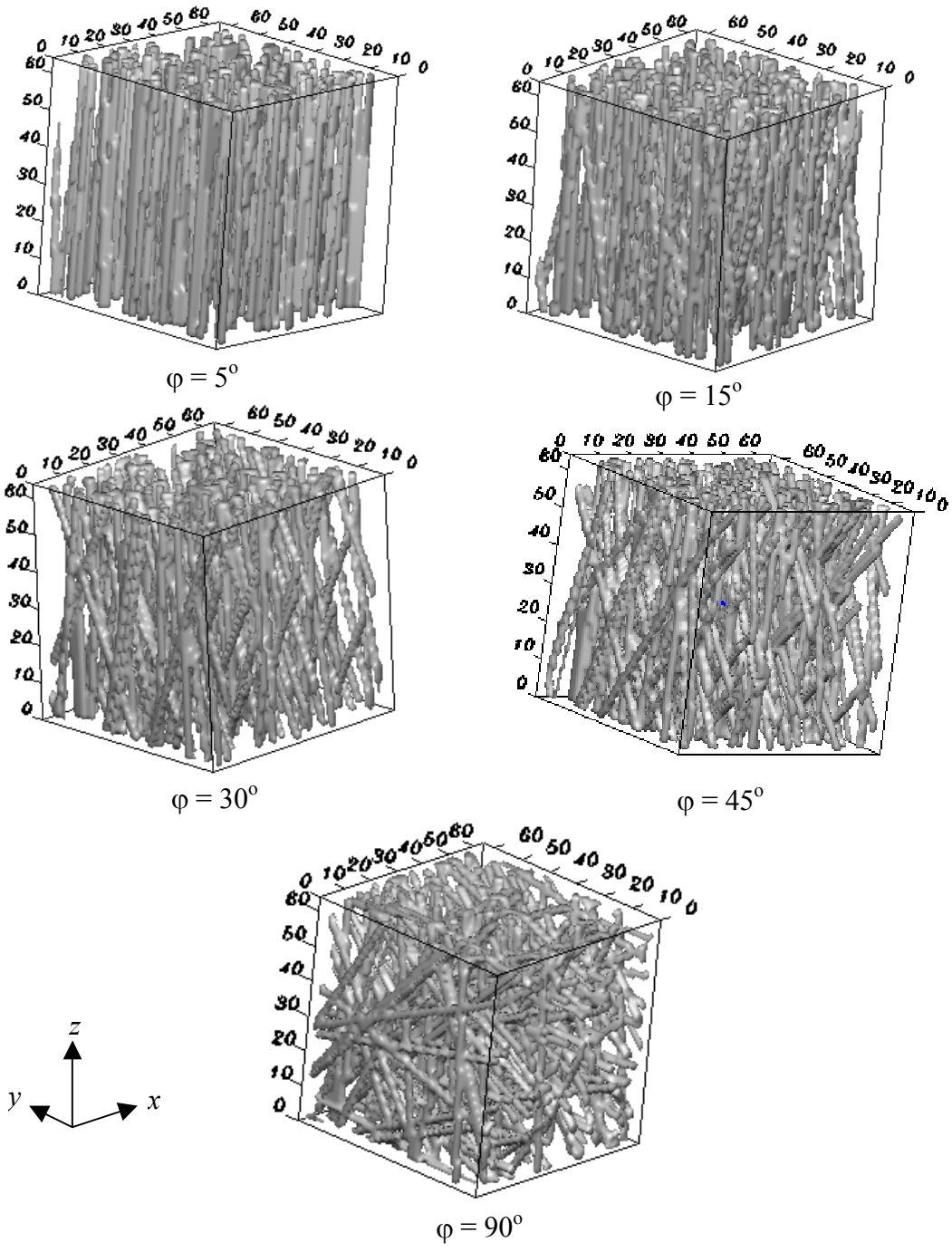

Figure 96. GDL with Preferred Direction in Fiber Orientation; ϕ is the Inclination Angle to the z-Axis

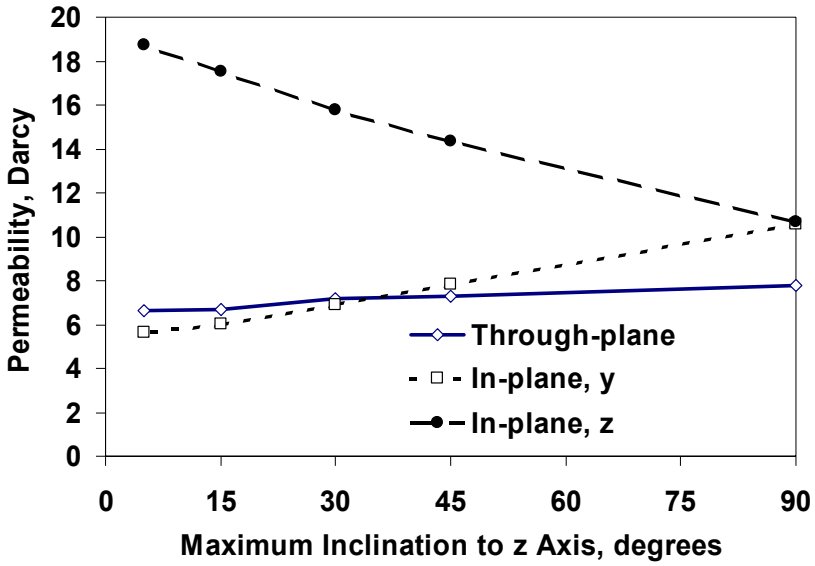

Figure 97. Through and In – Plane Permeability at Various Fiber-Orientations

4.6.2 BCS Fuel Cells Freeze-Thaw Performance Improvements

The improvement in cell performance, freeze-thaw cycling durability, and cold start-up time obtained by BCS Fuel Cells during the program is described above.

4.6.3 Techverse Developed Electrophoresis Method for GDL Teflon Treatment

As described above, initial SEM images of GDL surfaces during the accelerated aging tests performed by Techverse seemed to indicate that the Teflon coating on the GDL fibers was migrating in the direction of current flow. This observation led Techverse to evaluate using electrophoresis, as opposed to more traditional dip-coating, to impregnate PTFE into carbon paper GDL materials. The electrophoresis technique was demonstrated to produce more Teflon loading in the same processing time, and to more uniformly coat the carbon fibers within the media, as shown in the images of Figure 98 and Figure 99. Samples prepared with the electrophoresis technique also exhibited more resistance to Teflon migration and reduced loss of hydrophobicity on the surface during simulated aging experiments.

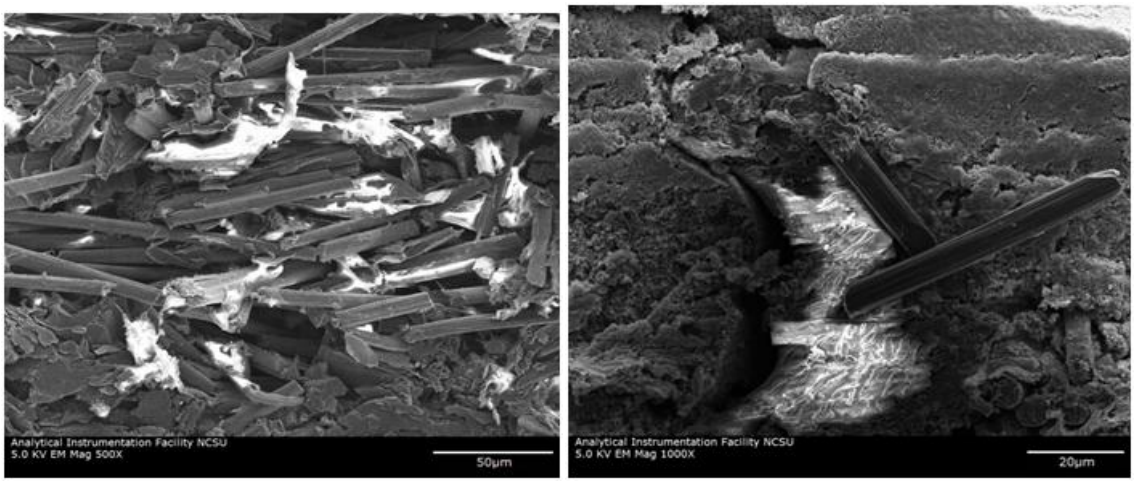

Figure 98. SEM Images of SGL Carbon 35EC GDL Media, 30% Tefon Content

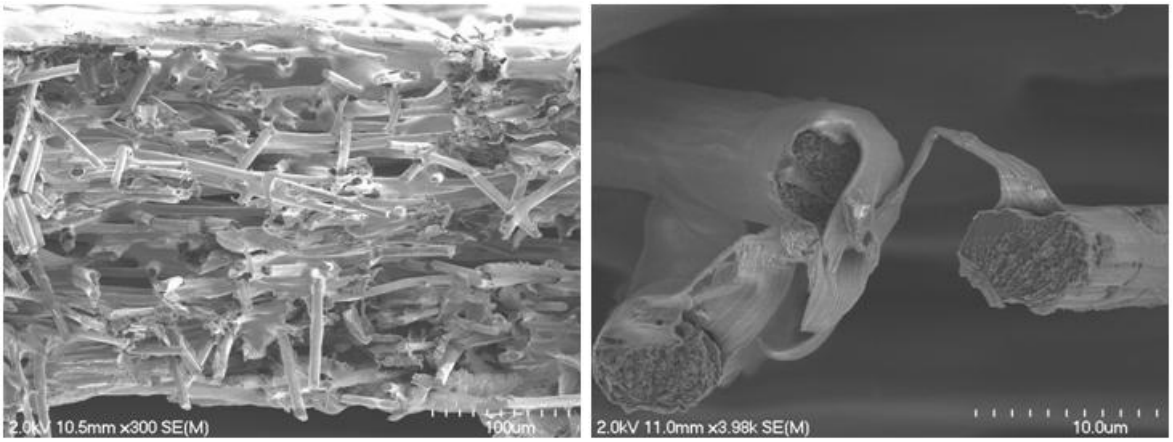

Figure 99. SEM Images of SGL Carbon 35AA GDL Media, initially 0 Teflon, after Electrophoresis Driven Teflonation to 30% Teflon Content

Capillary pressure characterization of the as-treated samples, Table , demonstrated consistently lower residual water saturation and breakthrough pressure of the electrophoresis coated samples. This is consistent with the electrophoresis technique producing more uniformly coated fibers, as seen in the SEM images.

Table 2. Comparison of Hydrophobicity Characteristics for Commercial and Electrophoresis Treated GDL Media

Sample	Residual Saturation	Breakthrough Pressure
n/a	%	Pa
35 EA - 30% Teflon	15.52	587
35 DA - 20% Teflon	25.54	1077
35 CA - 10% Teflon	7.6	1175
30% in-house AA sample	2.44	1959
7.5% in-house AA sample	2.32	1763
30% in-house A Toray	0.416	4800
15% in-house A Toray	0.6	3400
6% in-house A Toray	0.8	3100
30% in-house B Toray	0.769	3918
18% in-house B Toray	0.9	3300
4% in-house B Toray	1	3100
10% commercial Toray	3.3	780
20% commercial Toray	4	1000
30% commercial Toray	2.5	1100

Although Techverse was not able to generate a reproducible technique for treating microporous layers with the electrophoresis method before the project end, samples of the modified material were evaluated for fuel cell performance by BCS Fuel Cells. The initial tests demonstrated very poor performance under self-humidified operation, due to the absence of an MPL to maintain

hydration in the catalysts and membrane. An example polarization curve from these tests is shown in Figure 100, demonstrates that the electrophoresis treated materials at least deliver similar performance to the commercial materials in short-term operation. Despite the slightly higher initial activation loss for the Techverse material, the 30% Teflon sample provides a lower cell resistance at moderate currents. Development of an MPL fabrication procedure allowing operation at higher currents with significant water generation, and additional testing for longer-term performance, are needed to conclusively evaluate this approach to materials modification.

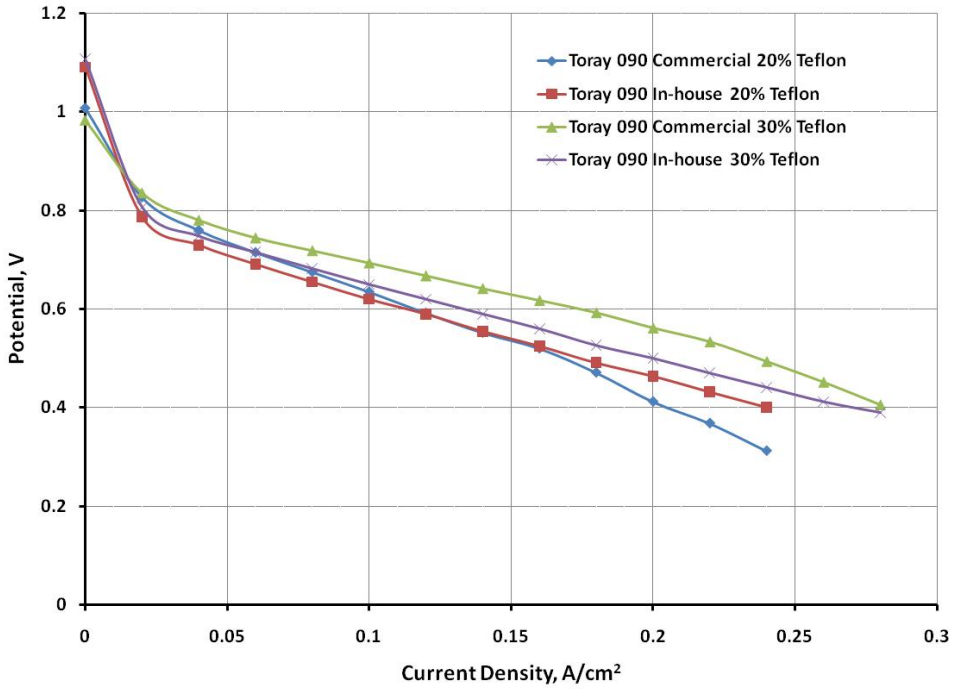

Figure 100. Cell Polarization Curves Comparing Techverse and Commercially Treated GDL Material Performance at 30°C, Self-humidified Operation

5. PRODUCTS DEVELOPED AND TECHNOLOGY TRANSFER

5.1 Publications and Presentations

The following publications, presentations, and conference proceedings articles resulted from this work:

1. Kunal Jain, James Vernon Cole, Sanjiv Kumar, Ashok Gidwani, and N. Vaidya, "A Multiphase, Two-Fluid Model for Water Transport in a PEM Fuel Cell", ECS Trans. 16, (2) 45 (2008). Presented at 214th Meeting of the Electrochemical Society.
2. Shiladitya Mukherjee, James Vernon Cole, Kunal Jain, and Ashok Gidwani, "Lattice-Boltzmann Simulations of Multiphase Flows in PEM Fuel Cell GDLs and Micro-channels," ECS Trans. 16, (2) 67 (2008). Presented at 214th Meeting of the Electrochemical Society.
3. Ashok Gidwani, Kunal Jain, and James Vernon Cole, "CFD Study of Carbon Corrosion in PEM Fuel Cells," ECS Trans. 16, (2) 1323 (2008). Presented at 214th Meeting of the Electrochemical Society.

4. "Formulation, Implementation and Validation of a Two-Fluid Model in a Fuel Cell CFD Code," Kunal Jain, James Vernon Cole, Sanjiv Kumar, N. Vaidya, Ashok Gidwani. Presented at 2008 Annual Meeting of the AIChE.
5. "Lattice-Boltzmann Simulations of Multiphase Flows in Gas-Diffusion-Layer (GDL) of a PEM Fuel Cell," Shiladitya Mukherjee, J. Vernon Cole, Kunal Jain, Ashok Gidwani. Presented at 2008 Annual Meeting of the AIChE.
6. "Water Transport Characteristics of Gas Diffusion Layer in a PEM Fuel Cell," Ashok S. Damle, J. Vernon Cole. Presented at 2008 Annual Meeting of the AIChE.
7. H. P. Dhar and S. K. Chaudhuri , "Detection and Verification of Electrode Flooding in Single Cell Studies," ECS Trans. 17, (1) 421 (2008). Presented at Fuel Cell Seminar, Phoenix, Arizona, November 27 - 30, 2008.
8. "Water Management in PEM Fuel Cell - A Lattice-Boltzmann Modeling Approach," S. Mukherjee, J. Vernon Cole, K. Jain, and A. Gidwani, Proceedings of FuelCell2009, ASME 2009 Seventh International Fuel Cell Science, Engineering and Technology Conference, FuelCell2009-85182 (2009). Presented at 2009 ASME 7th International Fuel Cell Science, Engineering & Technology Conference, June 8-10, 2009.
9. "Measurements of Fuel Cell Internal Resistances for the Detection of Electrode Flooding," H. P. Dhar and S. K. Chaudhuri, J. Solid State Electrochemistry 13, (7) 999 (2009).
10. S. Mukherjee, A. Gidwani, A. Roy, J. Vernon Cole, K. Jain, C. Bapat, and R. Thoms, "Multiphysics Simulation of Hydrogen PEM Fuel Cell," ECS Trans. 28 (27), pp. 93 – 102 (2010).

5.2 Technologies/Techniques

Techverse is continuing to develop the GDL treatment approach developed under this project.

5.3 Software Products

The LBM simulation capability was transferred to Ballard for additional use and application as desired. This capability was also used as the base modeling algorithm and software for US Navy SBIR N68335-10-C-0264.

The developed capabilities for the cell-scale models; namely two-phase flow in porous media, integration of two-phase flow with gas-phase chemical species transport and reaction, and integration with heat transfer and electrochemistry, were performed in collaboration with ESI Group. These capabilities have been integrated into the CFD-ACE+ commercial multiphysics simulation software.

In addition to assisting in the model implementation and testing, ESI completed the graphical user interface modifications for the code package. Options to activate the integrated two-phase flow, mass transfer, and heat transfer solver models developed during this program are provided when the user chooses to simulate a model with both electrochemistry and two-phase flow. Upon activation of these features in the GUI, relevant property input dialogues and choices for the detailed models are presented as shown in Figure 101 below.

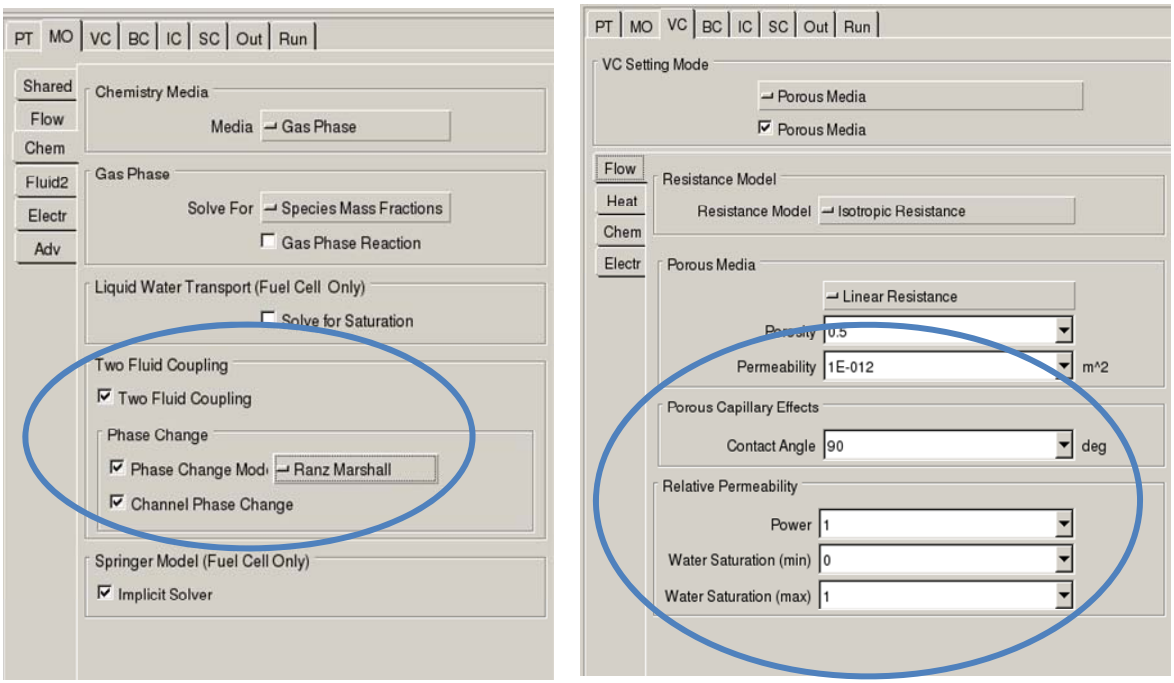

Figure 101. Graphical User Interface Dialogues added for: Specification of Coupling between a Chemical Species and Two-Phase Flow, Left; and Property Inputs for Two-Phase Flows in Porous Media, Right

6. COMPUTATIONAL MODEL DOCUMENTATION

6.1 LBM

The user guide prepared for the GDL microstructure generation and the LBM simulation code is attached as Appendix 1.

6.2 Cell-Scale Two-Phase Flow and Performance Model

This model was implemented within the commercial software CFD-ACE+, available from ESI Group. Theory manuals, User Guides, and tutorials for defining and simulating models with single-phase or two-phase fluid flow, heat transfer, chemical species transport and reaction, and electrical conduction are provided by ESI to licensed users of the base software. This documentation includes a dedicated section on application to fuel cell analysis. As seen in Figure 101 above, the primary inputs are activation of two-fluid coupling to the electrochemical analysis, selection of the phase change correlation, and specification of the model parameters for two-phase porous media flows.

7. SUMMARY

The overall objectives of this project were to achieve:

- Improved understanding of the effect of various cell component properties and structure on the gas and water transport in a PEM fuel cell, with particular emphasis on the gas diffusion media (GDM) and flow channels which have critical roles in transporting excess liquid water;

- Encapsulation of the developed advanced models in a commercial modeling and analysis tool, allowing transfer of technology to the industry for future applications to improve and optimize fuel cell design and operation; and
- Demonstrated improvements in water management resulting in improved efficiency during automotive drive cycles, freeze/thaw cycle tolerance, and faster cold startup.

CFDRC and our partners have contributed to each of these areas, and the developed technologies and modeling capabilities are continuing to be applied to improve fuel cell performance.

8. REFERENCES

1 Nguyen, T.V. *et al.* Measurements of Two-Phase Flow Properties of the Porous Media Used in PEM Fuel Cells. *ECS Transactions* **3**, 415-423 (2006).
2 Sole, J.D. & Ellis, M.W. Development of a Method for Determining the Two-Phase Relative Permeability Relationships in the Gas Diffusion Layers of PEM Fuel Cells. *ASME 2009 7th International Conference on Fuel Cell Science, Engineering and Technology* 729-739 (2009).doi:10.1115/FuelCell2009-85242
3 Litster, S., D. Sinton, and N. Djilali, "Ex Situ Visualization Of Liquid Water Transport In PEM Fuel Cell Gas Diffusion Layers," *Journal of Power Sources*, **154**(1), 95-105 (2006).
4 Bazylak, A., et al., "Effect of Compression On Liquid Water Transport and Microstructure Of PEMFC Gas Diffusion Layers," *Journal of Power Sources*, **163**(2), 784-792 (2007).
5 Bazylak, A., D. Sinton, and N. Djilali, "Dynamic Water Transport And Droplet Emergence In PEMFC Gas Diffusion Layers," *Journal of Power Sources*, **176** (1), 240-246 (2008).
6 Minor, G., "Experimental Study of Water Droplet Flows in a Model PEM Fuel Cell Gas Microchannel", M.A.Sc. Thesis, University of Victoria (2007).
7 P. Bhatnagar, E. Gross, and M. Krook, *Phys. Rev*., 94, 511 (1954).
8 D. D'Humie′res, I. Ginzburg, M. Krafczyk, P. Lallemand, and L. S. Luo, *Phil. Trans. Roy. Soc. Lon. A*, **360**, 437 (2002).
9 X., He, S., Chen, and R., Zhang, *J. Comp. Phys.*, **152**, 642 (1999).
10 S., Mukherjee and J., Abraham, *J. Coll. Inter. Sci.*, **312**, 341 (2007).
11 A. G. Yiotis, J. Psihogios, M. E. Kainourgiakis, A. Papaioannou, and A. K. Stubos, *Coll. Surf. A: Physiochem. Eng. Aspects*, **300**, 35 (2007).
12 V. P. Schulz, J. Becker, A. Wiegmann, P. P. Mukherjee, and C. Y. Wang, *J. Electrochem. Soc.*, **154**, B419 (2007).
13 M. Ishii, *Direction des Etudes et Recherches d'Electricit´e de France*, (1975).
14 Chapman, A. M. and Higdon, J. J. L. (1992). Oscillatory Stokes Flow in Periodic Porous Media. Physics of Fluids, 4(10):2099-2116.
15 H. Dohle, R. Jung, N. Kimiaie, J. Mergel, and M. Müller, *J. Power Sources*, **124,** 371 (2003).
16 S. Lister, D. Sinton, and N. Djilali, *Journal of Power Sources*, **154**, 95-105 (2006).
17 P. J. Oliveira, and R. I. Issa, *Int. J. Numer. Meth. Fluids*, **43**, 1177 (2003)
18 Brackbill J.U., Kothe D.B., Zemach C., "A Continuum Method for Modeling Surface Tension," *J. Comput. Phys.*, **100**, 335-354 (1992).
19 P.C. Sui, S. Kumar, N. Djilali, "Advanced Computational Tools For PEM Fuel Cell Design Part 1. Development and Base Case Simulations," *J. Power Sources*, **180**, pp. 410-422 (2008).

20 P.C. Sui, S. Kumar, N. Djilali, "Advanced Computational Tools For PEM Fuel Cell Design Part 2. Detailed Experimental Validation and Parametric Study,"*J. Power Sources*, **180**, pp. 423-432 (2008).
21 Lampinen, M.J., 1993. Analysis of Free Energy and Entropy Changes for Half-Cell Reactions. *Journal of The Electrochemical Society*, 140(12), p.3537.
22 Joshua D Sole and Michael W Ellis, in *ASME 2008 6th International Conference On Fuel Cell Science, Engineering and Technology* (ASME, Denver, CO, 2008), pp. 829-840.
23 Xuahai Wang and Trung Van Nguyen, "Modeling the Effects of Capillary Property of Porous Media on the Performance of the Cathode of a PEMFC," *J. Electrochem. Soc.*, **155** (11), B1085-B1092, 2008.
24 Andrew J. Desouza, Radu Bradean, Virginia Branzea, Stephen Hamada, Joerg Kleemann, Herwig Haas, Joy Roberts, and Emerson Gallagher, in *214th ECS Meeting, Volume 16, Issue 2, Proton Exchange Membrane Fuel Cells 8*, edited by Thomas F. Fuller, K. Shinohara, V. Ramani, P. Shirvanian, H. Uchida, S. Cleghorn, M. Inaba, S. Mitsushima, P. Strasser, H. Nakagawa, H. Gasteiger, T. Zawodzinski, and C. Lamy (ECS, Honolulu, HI, 2008), pp. 35-44.

APPENDIX 1

Users Guide for Lattice-Boltzmann Method (LBM) Software for GDL Microstructures

Developed Under DOE Award DE-FG36-07GO17010

Prepared by Shiladitya Mukherjee, CFDRC, Huntsville, AL – 2/10/2009

At the core of lattice-Boltzmann modeling approach is solution of a set of Boltzmann transport equations for a set of molecular distribution functions. The solution method mimics actual molecular transport through succession of streaming and collision. Because of the molecular or kinetic theory based nature of the solution algorithm, the continuum fluid properties such as, viscosity and surface tension are set indirectly by selecting appropriate LBM parameters related to collision time-scale, or strength of attraction between molecules etc. Similarly, imposition of continuum velocity or pressure condition at the boundary is performed through appropriate manipulation of the particle distribution functions. The Lattice-Boltzmann modeling approach and the GDL microstructure generation is discussed in additional detail in the conference proceedings article by Mukherjee [1].

The simulation set-up is done through the file *Input.in*, and these set-up conditions are output in the file *Input.out*. Following are description of input parameters. All parameters are non-dimensional.

Domain Size: *imax*, *jmax* and *kmax* are domain size in x, y and z direction, respectively.

1. In most simulations grid resolution used is δ_x = 3.4μm. In some of the cases, such as Teflonated GDLs, it is at higher resolution of 1.7μm to better capture PTFE distribution.
2. The cross-section area is typically 100μm×100μm or 200μm×200μm wide. Wider sample results in better statistical sampling in fiber distribution. GDL thickness is typically 170μm - 320μm thick, which is about 21 – 40 layers of fiber planes.

Problem Type: Switches are essentially either 0 or 1.

Parameter	**Description**	**Additional Notes**
iSinglePhase	• 0, multiphase flow • 1, single phase flow	A Multiphase solver can be set as single phase simulation by setting a) equal densities to both phase, b) zero surface tension and c) equating the upper and lower limit of the phase tracking variable φ, so that there is no variation in φ.
isMRT	• 0, BGK model	MRT is an improved modeling

	• 1, MRT model	approach over BGK (see ECS paper, Eq. 5)

Fluid Property:

Parameter	**Description**	**Additional Notes**
rho_h	normalized liquid density	In most LB models density ratios are typically limited to maximum of 10.
rho_l	normalized gas density	
relax_h	relaxation parameter, τ	• τ is related to *kinematic* viscosity, $v = (\tau - 0.5)(1/3)*\delta_t$. Here δ_t is characteristic time. • δ_t is computed from mean molecular streaming velocity as $c = \delta_x/\delta_t$. • In general, $\tau > 0.5$, otherwise viscosity would be negative. • It is recommended to set τ as 1. • v decreases as τ approaches 0.5, however, the numerical scheme becomes unstable.
surfT	surface tension parameter, κ	• κ is related to surface tension as $\sigma = \kappa I$, where $I=\int(\partial\varphi/\partial r)^2 dr$. The integration is along the normal to the diffused interface. • φ is the phase tracking variable somewhat similar to volume fraction in VOF. Its limiting values are LB model constants. In our model they are 0.2508 and 0.023 respectively for bulk liquid and gas, and I = 1.432E-2. • Recommended range for κ is below 0.1. Solution scheme will be prone to divergence at higher values. • For most of our computation we have used

		0.01.

Runtime, Output Frequency:

Parameter	**Description**	**Additional Notes**
itime_step_max	total simulation time steps, n_t	• GDL simulations are typically atleast 100,000 time steps. • total simulation runtime, $t = n_t \times \delta_t$
itime_view	Frequency of Plot-3D outputs	
itime_pr	Frequency of transient data output	• Transient data is usually some processed data, such as, difference between inlet and outlet pressure, liquid saturation inside GDL, permeability etc.

GDL Microstructure Generation:

1. GDL should usually have some free space at both inlet an outlet, typically 20 nodes or more thick.

Table 1. Parameters to set open space at GDL ends.	
iGDLSt	thickness of the open space at the inlet i.e. on Catalyst layer side
iGDLEnd	thickness of the open space at the outlet i.e. on Gas-channel side

2. GDL is constructed layer by layer. In each layer the fibers are oriented randomly (see Figure 4 of [1] and related discussion).

Table 2. Parameters to place carbon fibers.	
Parameter	**Description**
ifiberN	number of fibers in each plane
ifiberPl	number of planes
aziwidth	limiting value of azimuthal angle within a plane (see Figure 3)

thetaWidth	maximum inclination to the plane
fiberDia	fiber diameter
inPl	• 0, GDL *through-plane* direction along x-axis • 1, GDL *in-plane* direction along x-axis

Table 3. Parameters to add PTFE	
wallF	• sets contact angle within the GDL. • range is from 0 to 1. • linearly scales contact angle from 180 to 0. • for Toray 126º to 162º has been used.
iTeflon	• 0, No PTFE • 1, 2, 3, 4; incrementally higher value to add more wt% of PTFE
Note: Porosity is printed in *porosity.out* which has information on global porosity and layer by layer information.	

Domain Boundary Condition and Initial Condition:

Parameter	**Description**	**Additional Notes**
inletPrBC	• 1, pressure inlet boundary	• Inlet pressure is set by the input *PrIn* • Used for permeability measurements
inletWallBC	• 1, no-slip wall inlet	• Wall is of neutral wettability • Used for capillary imbibitions cases
iLiqThick	thickness of the liquid layer at the inlet	• The inlet corresponds to catalyst side. • The liquid layer may also extend inside the GDL.
alphaPore	initial uniform liquid saturation in the GDL	

ioutWallBC	• 0, outlet pressure boundary at reference pressure • 1, no-slip wall	• outlet pressure *1*(1/3)*gas-density*
PrIn	Sets the value of inlet pressure when *inletPrBC = 1*	• The value of inlet pressure is *P = PrIn*(1/3)*gas-density* • Pressure is transferred to non-dimensional unit by following relation, $p' = P*(\sigma'/\sigma)/\delta_x$,where primes are in dimensional unit.
iscreen	• 1, inserts a low porosity plug at the GDL outlet. liquid escape	• This is to prevent liquid escape during capillary imbibitions experiment

REFERENCES

1 S. Mukherjee, J. V. Cole, K. Jain, and A. Gidwani, "Lattice-Boltzmann Simulations of Multiphase Flows in PEM Fuel Cell GDLs and Micro-channels," *ECS Trans.* **16**, (2) pp. 67-77 (2008).